Physik-Department

Institut für Experimentalphysik E12

Interstellar radionuclides in Lunar samples

Dissertation

von

Leticia Fimiani

Technische Universität

München

Technische Universität München
Fakultät für Physik
Lehrstuhl für Experimentalphysik E12

Interstellar radionuclides in Lunar samples

Leticia Fimiani

Vollständiger Abdruck der von der Fakultät für Physik der Technischen Universität München zur Erlangung des akademischen Grades eines

Doktors der Naturwissenschaften

genehmigten Dissertation.

Vorsitzende(r): apl. Prof. Dr. Norbert Kaiser

Prüfer der Dissertation: 1. Univ. Prof. Dr. Walter Henning
2. Univ. Prof. Dr. rer. nat. Stefan Schönert

Die Dissertation wurde am 22. Mai 2014 bei der Technischen Universität München eingereicht und durch die Fakultät für Physik am 24. September 2014 angenommen.

To my father

Abstract:

The discovery of an ^{60}Fe/Fe spike in a ferromanganese crust from the Pacific Ocean implied the deposition of freshly synthesized material coming from a nearby supernova (SN) about 2 Myr ago. After this finding, there has been an ongoing effort to improve our knowledge by studying other reservoirs where the SN debris could be found.

Within the framework of this thesis a set of 24 lunar samples coming from the Apollo 12, 15 and 16 missions were analyzed with accelerator mass spectrometry (AMS). The isotopic ratios ^{53}Mn/Mn and ^{60}Fe/Fe were measured at the Maier-Leibnitz-Laboratorium in Garching, Germany, at the Gas-filled Analyzing Magnet System (GAMS) facility. This was the first time that a systematic measurement of these isotopic ratios in identical lunar samples was performed. The radioisotopes ^{53}Mn ($T_{1/2} = 3.7 \times 10^6$ yr) and ^{60}Fe ($T_{1/2} = 2.62 \times 10^6$ yr) are synthesized in massive stars and via spallation reactions of solar and galactic cosmic rays (SCR and GCR, respectively) on iron and nickel targets. To estimate the *in-situ* production of these radionuclides, a set of 7 samples coming from 4 different iron meteorites was analyzed at the same facility. Iron meteorites are composed mainly of nickel and iron and were usually exposed to GCR for a few 10^8 yr. Thus, they are rich in ^{53}Mn and ^{60}Fe. A strong, almost linear correlation between the activities of both radioisotopes was found.

The ^{60}Fe/Fe ratios (and respective high ^{60}Fe activities per kg nickel) in Moon samples taken from the top 10 cm of the lunar surface were considerably higher than in the meteoritic samples. It is thus inferred that SCR and GCR cannot be responsible for this high ^{60}Fe activity on the lunar surface, and that there has been a deposition of interstellar material, most likely from SN origin. A local interstellar fluence of ^{60}Fe between 4×10^7 at/cm^2 $< \Phi <$ 2×10^8 at/cm^2 was determined. No related signal of ^{53}Mn was found because of the high cosmogenic background due to a high concentration of iron in the lunar surface.

Keywords: ^{60}Fe, ^{53}Mn, Moon, accelerator mass spectrometry, supernova

Zusammenfassung:

Die Entdeckung einer ^{60}Fe/Fe Erhöhung in einer Ferromangan Kruste aus dem Pazifisch Ozean deutete auf die Deposition von kürzlich synthetisiertem Material einer nahen Supernova (SN) vor etwa 2 Myr hin. Nach diesem Fund gab es ein kontinuierliches Bestreben, unser Verständnis durch Untersuchungen anderer Reservoirs zu verbessern, in denen die SN Spuren ebenfalls vorhanden sein könnten.

Im Rahmen dieser Arbeit wurden 24 Mondproben von den Apollo Missionen 12, 15 und 16 mit Beschleunigermassenspektrometrie (AMS) untersucht. Die Isotopenverhältnisse ^{53}Mn/Mn und ^{60}Fe/Fe wurden am Maier-Leibnitz-Laboratorium in Garching, Deutschland, am Gasgefüllten-Analysier-Magnet-System (GAMS) bestimmt. Dies ist das erst Mal, dass eine systematische Studie beider Isotopenverhältnisse in identischen Mondproben durchgeführt wurde. Die Radioisotope ^{53}Mn ($T_{1/2} = 3.7 \times 10^6$ yr) und ^{60}Fe ($T_{1/2} = 2.62 \times 10^6$ yr) werden durch Nucleosynthese in schweren Sternen und durch Spallationsreaktionen durch solare und galaktische kosmische Strahlen (SCR und GCR) an Eisen und Nickel erzeugt. Um die *in-situ* Produktion dieser Radionuklide abzuschätzen wurden 7 Proben von 4 verschiedenen Eisenmeteoriten zusätzlich untersucht. Eisenmeteorite bestehen hauptsächlich aus Nickel und Eisen und waren GCR typischerweise für mehrere 10^8 yr ausgesetzt. Deshalb sind sie reich an ^{53}Mn und ^{60}Fe. Eine starke, fast lineare Korrelation zwischen den Aktivitäten beider Radioisotope wurde gefunden.

Die ^{60}Fe/Fe Verhältnisse (und ebenfalls hohen ^{60}Fe Aktivitäten pro kg Nickel) in Proben von den oberen 10 cm der Mondoberfläche waren deutlich höher als in den Meteoritenproben. Deshalb wird darauf geschlossen, dass SCR und GCR nicht für diese hohe ^{60}Fe Aktivität auf der Mondoberfläche verantwortlich sein können und dass es eine Deposition von interstellarem Material, wahrscheinlich erzeugt durch eine oder mehrere solarnahe SNe, gegeben hat. Eine lokale, interstellare Fluenz von ^{60}Fe im Bereich 4×10^7 at/cm^2 $< \Phi <$ 2×10^8 at/cm^2 wurde bestimmt. Kein entsprechendes Signal von ^{53}Mn wurde gefunden, da der kosmogene Untergrund wegen der hohen Eisenkonzentration auf der Mondoberfläche zu groß war.

Schlüsselwörter: ^{60}Fe, ^{53}Mn, Mond, Beschleunigermassenspektrometrie, Supernova

Contents

CHAPTER 1

Introduction

When a massive star ($M \gtrsim 8M_\odot$) exhausts its nuclear fuel, after having undergone several burning stages, it suffers a gravitational collapse and finally explodes. The result is a bright object called *supernova* (SN), which can even outshine its host galaxy for weeks. Its name comes from latin, (*nova*, new) since it was first believed that these events were the birth of stars in dark regions of the sky. The distinction between novae and supernovae came centuries after their first observation, the latter ones being several orders of magnitude brighter.

Different observations indicate that one or even more SN explosions occurred in the vicinity of our Solar System during the past several million years. It has been shown that the Local Bubble, a hot and sparse cavity in the interstellar medium (ISM) enclosing the Sun, was created by 14 to 20 SN explosions starting aproximatelly 13 Myr ago [Fuchs et al., 2006]. Observations of the composition of cosmic rays [Moskalenko et al., 2003] also give strong hints of SN events near the Solar System. There are also discussions of the consequences of such an event near our solar system, for example mass extinction [Ellis and Schramm, 1995; Benitez et al., 2002].

Understanding of the interactions of the supernovae and the ISM, and the interaction of the ISM and the interplanetary space is still incomplete. With the first man-made object that reached the ISM, namely the Voyager-1, a space probe launched by NASA in September 1977 that entered the interstellar space in August, 2012 [Voyager-1, 2013], new information is being gathered and analyzed in order to increase our knowledge on this matter. The material ejected by a supernova achieves very high velocities and heats up the ISM. The shock wave generated in the explosion sweeps up the matter in the ISM and enriches it with freshly synthesized material [Landgraf et al., 2000]. About two supernovae every century contribute to this end in the Milky Way [Janka, 2012].

If a SN occurs in the close vicinity of our solar system (around a few tens of parsecs), there is a chance that the debris of the explosion could enter the solar system, reach the Earth's orbit and could be detected in appropiate reservoirs on the Earth and on the

Moon. Possible candidates for the detection are isotopic anomalies of radioisotopes that are copiously produced during such an event, such as: ^{26}Al ($T_{1/2} = 7.1 \times 10^5$ yr), ^{10}Be ($T_{1/2} = 1.387 \times 10^6$ yr), ^{53}Mn ($T_{1/2} = 3.74 \times 10^6$ yr), ^{60}Fe ($T_{1/2} = 2.6 \times 10^6$ yr), ^{129}I ($T_{1/2} = 1.57 \times 10^7$ yr), ^{182}Hf ($T_{1/2} = 8.9 \times 10^6$ yr), ^{146}Sm ($T_{1/2} = 1.03 \times 10^8$) yr), ^{244}Pu ($T_{1/2} = 8 \times 10^7$ yr). Since the mass deposited should be very small, the selection of the appropiate reservoir is crucial. Furthermore, the development of adequate detection techniques is essential.

Hints of a close by supernova explosion were confirmed by the detection of SN material on Earth, as presented by Knie et al. [Knie et al., 2004, 1999a]. A time profile of the ^{60}Fe/Fe concentration in a Pacific Ocean ferromanganese crust was measured, displayed in Fig. 1.1, showing a significant increase between about 1.7 and 2.6 Myr ago, implying a near by (tens of pc) SN event. The growth rate of the crust was determined with the measurement of a ^{10}Be depth profile [Fitoussi et al., 2008].

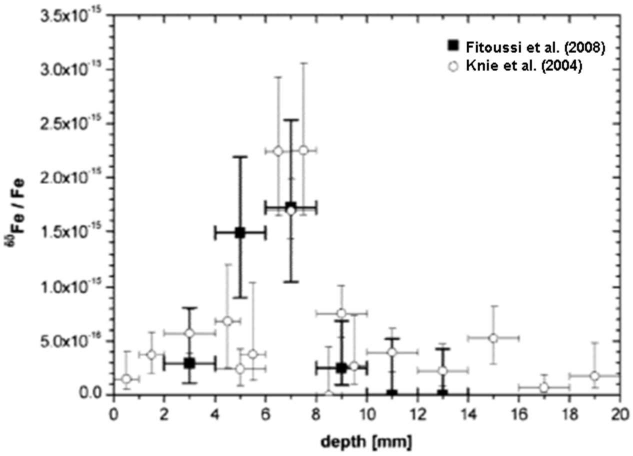

Figure 1.1. ^{60}Fe/Fe depth profile in a ferromanganese crust taken from the equatorial Pacific Ocean. Image taken from Fitoussi et al. [2008]. In their work, the depth profile measured by Knie et al. [2004] was remeasured using a different chemical preparation of the samples. Their results (black squares) agree with the ones published by Knie et al. (white squares).

The excess of ^{60}Fe to stable iron found in the ferromanganese crust is on the order of a few times 10^{-15}. This observation was only possible with the ultrasensitive accelerator mass spectrometry (AMS) technique, which has a sensitivity for the detection of concentrations of ^{60}Fe/Fe $\approx 10^{-16}$ or even lower. AMS is a method for determining isotopic ratios using an accelerator, making use of higher energies (MeV range) than regular mass spectrometers, allowing the complete suppression of molecular background in a stripping process and the use of nuclear physics methods for isobar separation and particle identification.

The determination of the local interstellar fluence of ^{60}Fe, *i.e.* the number of atoms originally present in the ISM passing through an area of 1 cm^2, using the measurement in the ferromanganese crust was achieved using a series of assumptions. The growth rate of the crust was determined by measurement of the cosmogenic radionuclide ^{10}Be profile [Segl et al., 1984; Fitoussi et al., 2008], assuming constant ^{10}Be flux in the past. The local interstellar fluence of ^{60}Fe atoms, was estimated to be $\Phi \approx 2 \times 10^9$ atoms cm^{-2} [Knie et al., 2004]. This was done by comparing earlier measurements of the cosmogenic flux of ^{53}Mn in ice [Bibron et al., 1974] and sediment samples [Imamura et al., 1979], ^{55}Mn in ocean water, and the ratio of ^{53}Mn/Mn measured in the same crust. These different results were used to determine an uptake factor of ^{60}Fe of the crust, *i.e.* the percentage of extraterrestrial iron that was actually incorporated in the crust. This uptake factor was used to estimate the local interstellar fluence, according to the measured ^{60}Fe/Fe depth profile. The resulting value has to be revised, since Auer et al. measured a value for the ^{53}Mn flux in ice that is almost 160 times smaller than the one determined in Bibron et al. [1974]. This would lead to a local interstellar fluence of about two orders of magnitude lower than the one reported by Knie et al..

A similar search for a SN signature in marine sediment [Fitoussi et al., 2008] was unsuccessful to confirm the findings in the ferromanganese crust. Possible causes for this results may lie in the much smaller fluence, in the chemical preparation of the samples, leading to a dilution of the expected signal, or an unsuited sampling site. There are ongoing efforts in order to find a signature in sediment cores from a different location [Feige et al., 2012] and by a selective iron extraction [Ludwig et al., 2013].

If the observed ^{60}Fe signal is indeed from a supernova event, then it is reasonable to assume that SN debris has also been deposited on the Moon and that an excess of ^{60}Fe should also be found there. The lunar surface can be considered as a SN debris collector having several advantages in comparison with terrestrial reservoirs. On Earth, sedimentation and mixing due to wind and/or water transport can dilute the ^{60}Fe signal. Wind and water do not exist on the Moon, therefore long-lived radionuclides from a SN event should be still present on the lunar surface today. Unlike terrestrial samples, it is not possible to measure a time profile of the concentration of any isotope on the lunar surface. However, an accurate estimation of the local interstellar ^{60}Fe fluence should be possible. Since the isotopic abundance in SN ejecta represents a superposition of the products from different nucleosynthesis scenarios preceding the ejection event, observation of several of these isotopes also would yield important astrophysical constraints on nucleosynthesis. For example, a finding of r-process isotopes, such as ^{182}Hf and ^{244}Pu coinciding with a ^{60}Fe signature would conclusively link SN to the r-process.

The lunar surface is constantly being stirred and mixed due to stochastic impacts of micrometeorites (*gardening*). This process affects the lunar surface on different scales. A rule of thumb is to assume that the first 2 cm of the lunar soil (*regolith*) are mixed on a Myr timescale. This was calculated by comparing theoretical predictions of the in-situ production rates of different radioisotopes (mainly ^{26}Al and ^{53}Mn) as a function of depth, with actual measurements of the activity of the same radioisotopes in depth profiles in lunar cores (brought back to Earth by the astronauts of the Apollo missions) [see, for example, Nishiizumi et al., 1979]. Deviations of the expected profile where interpreted as mixing of the soil. The analyses coming from different cores (*i.e.* different locations on the Moon) showed varying results. This gardening effect of the regolith can then dilute the sought SN signal, whereas the total number of ^{60}Fe atoms should be preserved.

For this work we chose samples originating from three different Apollo missions. We received material from 3 different cores and a set of pristine samples collected from the vicinity and underneath a small boulder. Core samples are very valuable, mainly because they are the only information about the lunar stratigraphy available to this date. They shed light on the mixing mechanisms, down-slope movement of regolith from near craters and are available with good depth resolution.

An important factor that cannot be neglected is the *in-situ* production of radionuclides. ^{53}Mn is synthesized in spallation reactions in iron and nickel targets. ^{60}Fe is also produced in this way, mainly in nickel-rich materials. Fortunately, the concentrations of Ni by lunar material is in general low (in the order of a few hundred ppm). Thus, the expected production of ^{60}Fe due to spallation reactions with galactic and/or solar cosmic rays is also low. To address this issue experimentally, we measured the concentrations of ^{53}Mn/Mn and ^{60}Fe/Fe in a set of iron meteorites. Iron meteorites are composed mainly of iron and nickel and were irradiated for several million years, thus they have very high concentrations of both radioisotopes. They should be an accurate reference to account for the cosmogenic production of ^{53}Mn and ^{60}Fe.

This thesis is organized as follows. Chapter 2 is dedicated to the production mechanisms of the radioisotopes relevant in this work, ^{53}Mn and ^{60}Fe. It is followed by a chapter describing in detail the principles of AMS, outlining also the relevant parameters used in the measurements of the samples. The fourth chapter gives an overview on the previous studies of the samples studied here, in order to have an understanding of the history of each sample. The results obtained in this work are shown in chapter 5, followed by a thorough discussion. The last chapter summarizes the most important results and conclusions.

Chapter 2

Synthesis of ^{53}Mn and ^{60}Fe

Contents

The process of creation of new nuclei from preexisting ones is called *nucleosynthesis*. This can be roughly split up into these basic scenarios:

1. The lightest nuclei ($A \lesssim 4$) were mostly synthesized minutes after the Big Bang.
2. Elements up to the iron group can be synthesized in different stages of hydrostatic burning in stars.
3. Most heavier elements are formed in neutron capture processes.

A brief explanation of the last two scenarios will be given in this chapter, with more detail on the isotopes measured in this work, followed by a discussion of cosmogenic creation of these isotopes.

2.1 Stellar Nucleosynthesis

The attempt to explain the transformation of abundances after the Big Bang (mostly H and He) to the rich variety of isotopes we can observe today is the main task of nuclear astrophysics. Gamov [1946] was the first to estimate how fast the density of the universe had to change in order to have the first atoms being created. Later, Alpher et al. [1948], stated that hydrogen, helium and a few other heavier elements were created during the Big Bang. This work argued, incorrectly, that all heavier elements were then produce via successive neutron capture reactions. It was in 1957, with the famous appearance of the B^2FH paper [Burbidge et al., 1957] that the synthesis of chemical elements different than H and He was suggested, via thermonuclear reactions in the interior of the stars. It gave rise to the theory of stellar nucleosynthesis.

The fact that stars like our Sun do not collapse under their own gravitation implies the existence of a source of pressure in the stellar interior, which can counteract gravity. The pressure for this comes (in most stars) from hydrostatic fusion reactions, continuously transforming one element into another.

The general picture of subsequent burning stages can be understood as follows. In a stellar core fusion reactions between nuclei having the lowest Coulomb barrier will usually dominate the reaction flow, providing a source of energy. These thermonuclear reactions change the composition of the stellar plasma, until the fuel for the burning stage is consumed entirely, leading to a gravitional contraction of the stellar core. In many cases, the previous burning stage can now continue in a shell around the core. The temperature in the core will rise to a point were the nuclei with the next lowest Coulomb barrier are ignited. The next burning stage will provide the nuclear energy which stabilizes the star's core against further contraction. Depending on the mass and initial composition of a star, it may undergo several burning stages. These are briefly described in the next sections.

2.1.1 Hydrogen burning

The first fusion stage in all stars is hydrogen burning. Depending on the temperature and initial composition, the two main reaction networks which can contribute to hydrogen burning are the proton-proton (p-p) chain and the carbon-nitrogen-oxygen (CNO) cycle.

While the p-p chain is most efficient for low-mass stars, like our Sun, the CNO cycle (which uses C, N and O as catalysts) dominates for heavier stars ($M \gtrsim 2M_\odot$). However, the sum reaction of both hydrogen burning mechanisms is the same:

$$4\mathrm{p} \rightarrow {}^4\mathrm{He} + 2\mathrm{e}^+ + 2\nu + \mathrm{Q}$$

were Q is the released energy, varying from 19.2 to 26.2 MeV per reaction [Rolfs and Rodney, 1988]. Stars undergoing core H burning are referred to as main sequence stars, and make up for most of the stars in our night sky. The reason for this is that both p-p chains and CNO cycles involve weak interactions, leading to very large time scales (in the order of Myr or Gyr) allowing stars to slowly burn H for the majority of their lives.

2.1.2 Helium burning

When the hydrogen is consumed in the core, the star will slowly contract increasing both the temperature and density, until helium is ignited. The hydrogen in a shell around the core will heat up and continues to burn. Inside the core, two helium atoms fuse into the unstable ^{8}Be until an equilibrium concentration of ^{8}Be/^{4}He $\sim 10^{-9}$ is reached. This amount of beryllium is sufficient to capture an additional ^{4}He nucleus, producing ^{12}C. This chain of reactions is also known as the triple-α process.

Subsequently ^{12}C can capture an alpha particle to form ^{16}O. In principle, this capture process can continue to create ^{20}Ne, ^{24}Mg, ^{28}Si, and so on. However, since the ^{16}O(α,γ)^{20}Ne is a very slow process, the typical ashes of helium burning are ^{12}C and ^{16}O.

2.1.3 Advanced burning stages

For stars M $\gtrsim$ 8M$_{\odot}$ a new burning stage begins once the helium in the core of the star is consumed. The core contracts until the density and temperature are sufficiently high to ignite the ashes of the previous burning phase.

The fusion reaction with the lowest Coulomb barrier involves two nuclei of ^{12}C. The resulting highly excited (^{24}Mg*) system releases energy by the emission of lighter particles (protons, neutrons or alpha particles). These are rapidly consumed in secondary reactions involving the ashes of the helium burning or even the products of the primary reactions. This series of reaction is referred to as carbon burning.

After carbon is almost consumed, the core is composed mostly of ^{16}O, ^{20}Ne, ^{23}Na and ^{24}Mg. When the core contracts, it is sensible to assume that the next fuel, ^{16}O, will ignite in fusion reactions. But at this point, the temperature in the core is so high (in the order of GK) that some nuclei will be involved in photodisintegration reactions. Since the separation energy of an α particle is relatively low, the reaction ^{20}Ne(γ,α)^{16}O takes place. The released α particle reacts with the ashes from the precious burning stage in a successive chain of reactions known as neon burning.

The core, now formed mainly by ^{16}O, ^{24}Mg and ^{28}Si, starts contracting once again until the temperature is high enough for the fusion of two oxygen atoms. Analog to what happens during the carbon burning, the resulting ^{32}Si is highly excited. The excess energy is removed by the emission of lighter particles that are consumed by secondary reactions. This phase of the star is called oxygen burning. After the oxygen in the core is consumed, mostly ^{28}Si and ^{32}S remain. Fusion reactions involving these nuclei are unlikely to occur, since the Coulomb barriers are too high, even at the high temperatures achieved to this stage. At this point, a photondisintegration rearrangement takes place, similar to the neon burning, but to a much larger scale. The lighter particles now available, together with nuclei of intermediate masses, form the most tightly bound nuclei (the so called iron peak), in what is referred to as silicon burning.

At this point, the massive star has an onion-like structure, with different shells or layers containing the ashes or fuel from the different burning stages it went through. Temperatures, densities, predominant constituents and burning stages are summarized in Table 2.1 [Rolfs and Rodney, 1988]. The core is principally composed of nickel and iron. Since the density and temperature rise toward the interior of the star, the boundary between each layer is also a burning region. As the density gradient between layers is high, there is no convective mixing across them.

Shell burning	Predominant constituents	Temperature K	Density g/cm^3	Time scale
p → ^{4}He	H, He, C, N, O	2×10^7	10^2	5 Myr
^{4}He → ^{12}C, ^{16}O	He	2×10^8	10^4	0.5 Myr
^{12}C → ^{20}Ne	^{12}C, ^{16}O	5×10^8	10^5	0.6 kyr
^{20}Ne → ^{16}O	^{16}O, ^{20}Ne, ^{23}Na, ^{24}Mg	1×10^9	10^6	1 yr
^{16}O → ^{28}Si	^{16}O, ^{24}Mg, ^{23}Na	2×10^9	10^6	0.5 yr
^{28}Si → ^{56}Ni	^{28}Si	4×10^9	10^7	1 day

Table 2.1. Properties of the different shells composing a massive star. The information is extremely simplified and is only presented to give an estimate or an order of magnitude of the conditions present in each shell [Rolfs and Rodney, 1988].

2.1.4 Nucleosynthesis beyond iron

Beyond the iron peak, more energy is consumed by the photodisintegrations in the silicon burning stage of the star than what is gained by adding nucleons or α particles to nuclei, since the binding energy is maximum at this mass region. Hence, charged particle induced nucleosynthesis is stopped at this point. Heavier nuclei are formed mainly by successive neutron captures. Since there is no Coulomb barrier for neutrons, the cross sections of neutron induced reactions can be very large. After adding several neutrons, at some point, a β-unstable nucleus will eventually be formed. As originally suggested by B^2FH [Burbidge et al., 1957], neutron capture nucleosynthesis can be split up into two different processes: the slow s-process and the fast r-process.

The rapid neutron capture process is believed to occur under extreme conditions with high temperatures (in the order of GK) and neutron density (up to 10^{22} cm^{-3}) [Rolfs and Rodney, 1988]. Under these conditions, the time scale for neutron captures is extremely short (ms) and an equilibrium along isotopic chains is quickly established. Only when the path of nucleosynthesis reaches a closed neutron shell, or the neutron drip line, β-decays can affect the reaction flow. Thus, the r-process proceeds far away from the valley of stability, involving the most neutron-rich nuclei. When the neutron flux seizes typically after few seconds, the neutron-rich products are allowed to β-decay back towards the valley of stability, yielding a great variety of isotopes, up to the heaviest ones observed.

The s-process can be viewed as a nucleosynthesis scenario with moderate conditions (medium neutron densitities, $10^6 - 10^{11}$ cm^{-3}) with neutron capture timescales τ_{n} on the order of years to thousands of years [Rolfs and Rodney, 1988]. This allows the competing β-decay rates ($\tau_\beta << \tau_{\mathrm{n}}$) to keep the nucleosynthesis path very close to the valley of stability. The s-process abundances in our solar system can be best reproduced using a set of at least two different s-process components with different neutron exposures, hinting to the observed s-process abundances being a superposition of nucleosynthesis from more than one s-process site. Firstly, the so-called weak s-process, producing mostly nuclei with A $\lesssim$ 80, can occur during the He and C core and shell burning phases of massive stars, making use of the neutron source ^{22}Ne(α,n)^{25}Mg reaction. Secondly, the main component of the s-process, producing the majority of observed abundances (A $\leq$ 209) which can occur during the asymptotic giant branch (AGB) phase of stars with intermediate masses ($1\mathrm{M}_\odot \lesssim \mathrm{M} \lesssim 8\mathrm{M}_\odot$). In this phase of stellar evolution, H and He fuel in the core are exhausted, but stellar mass is insufficient to ignite carbon burning in the core, which consists mostly of ^{12}C and ^{16}O. In alternating shell burning phases in the H and He shells, an s-process can occur with the ^{22}Ne(α,n)^{25}Mg and ^{13}C(α,n)^{16}O neutron sources, the latter one taking place in a ^{13}C ̈bubbleformed after mixing of proton rich material into the He-shell following thermal pulses caused by the He ignition.

2.1.5 Supernovae

In the innermost shell around the core of a massive star there is still silicon burning to iron, adding more iron to the core, which is stabilized by electron degeneracy pressure. At some point, the core cannot longer support itself against gravity and starts to collapse.

This process is accelerated, while photons disintegrate some of the iron-peak nuclei and electrons are being captured by protons within nuclei forming a proto-neutron star, releasing neutrinos. These can escape from the star, since they interact only weakly with the matter, but may still play an important role in heating the ejecta later [Janka, 2012]. As the core loses energy with these two mechanisms, it contracts and heats up. This happens in only fractions of a second, a very short time compared to the life of the star itself.

When the density in the core reaches nuclear densities ($\rho \gtrsim 3 \times 10^{14}$ g/cm^3), the collapse is abruptly stopped, and as the core rebounds, an expansive shock wave is produced, leading to explosive nucleosynthesis during the passage through the outer layers. Some nuclei undergo photodisintegration or fission, increasing the number of nuclei, thus augmenting the pressure. In this way, the outer layers of the star are ejected in what is called a supernova explosion [Janka, 2012].

2.2 Production of ^{60}Fe in stars

The half life of ^{60}Fe is $T_{1/2} = (2.62 \pm 0.04)$ Myr [Rugel et al., 2009]. Following Limongi and Chieffi [2006], it is mainly produced during the s-process in massive stars, via two successive n-captures on ^{58}Fe (see Fig. 2.1). The cross section for these neutron capture process has a weak dependence of the temperature, but the half life of ^{59}Fe is strongly decreasing with increasing temperature due to (γ,n) reactions. It has a terrestrial half life of $T_{1/2} = 44$ days, 6 days by $T = 1 \times 10^9$ K and only one hour at $T = 4 \times 10^9$ K. The neutron capture reaction must compete with the β-decay to produce a considerable amount of ^{60}Fe. For an efficient production of ^{60}Fe a minimum of 3×10^{10} n/cm^3 is needed at temperatures below $T = 5 \times 10^8$ K, as, at a temperature of the order of 2×10^9 K, both ^{59}Fe and ^{60}Fe are destroyed via the (n,γ) and (p,γ) reactions. Therefore ^{60}Fe is mainly synthesized during the He, C and Ne burning phases.

The main neutron donor in the He burning is the ^{22}Ne(α,n)^{25}Mg reaction. In central He burning, temperatures are still to low for an efficient neutron production. During the shell burning, temperatures may rise up to the required value of $T = 4 \times 10^8$ K to reach the needed neutron densities. Similarly, during the central C burning stage, the neutron densities are in the order of a few times 10^7 g/cm^3. Throughout the shell burning, higher temperatures than 10^9 K allow for a sufficient generation of neutrons. Meanwhile, in the Ne shell burning there is a large abundance of neutrons due to the ^{23}Na(α,n)^{26}Al reaction, but due to the absence of a stable convective shell that lasts until

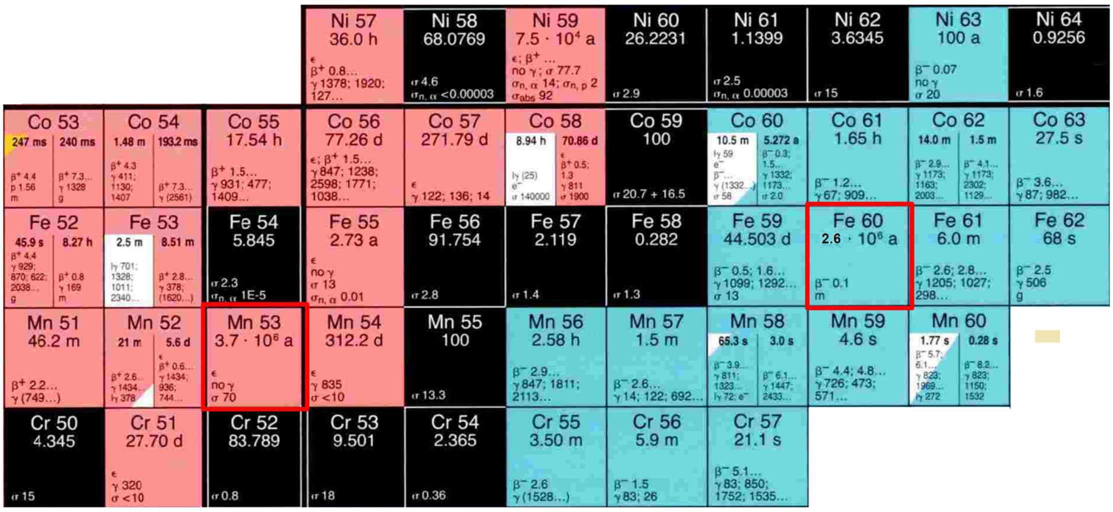

Figure 2.1. Detailed view of the nuclide chart around the isotopes discussed in this section, ^{53}Mn and ^{60}Fe, marked in red boxes. The half life for ^{60}Fe was corrected according to Rugel et al. [2009].

the supernova explosion, no significant amount of ^{60}Fe is produced. Finally, when the shock wave crosses the mantle as it travels outward, the temperature reaches a maximum in the order of $T = 2 \times 10^9$ K and ^{60}Fe is explosively synthesized. This last contribution represents only a fraction of the total ^{60}Fe yield.

The ^{60}Fe yield depends strongly on the initial mass of the star. There are several publications that calculate the yields for different types of stars in different mass ranges. Five were chosen to illustrate what is expected in a mass range from 2 - 120 $M_\odot$ [Limongi and Chieffi, 2006; Karakas and Lattanzio, 2007; Woosley and Weaver, 1995; Rauscher et al., 2002; Woosley and Heger, 2007] (see Fig. 2.2). The different results for similar mass arise from several factors, like the initial composition of the star, the chosen explosive mechanism that triggers the supernova, the description of the convective zones and the boundaries between them.

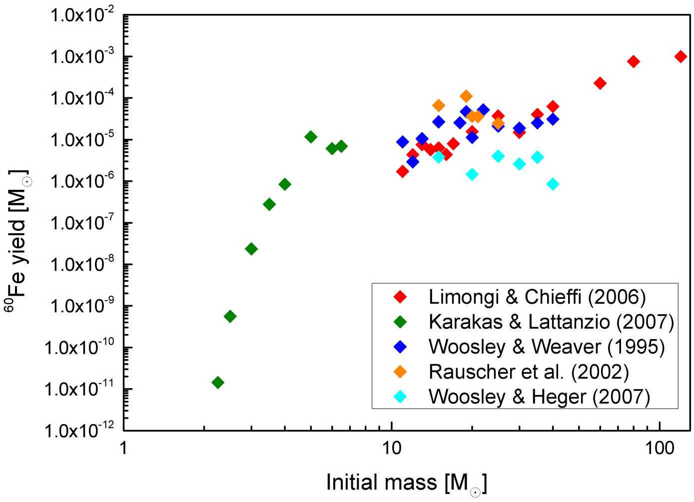

Figure 2.2. Compilation of yields of ^{60}Fe as a function of the initial mass of the star. Data taken from Limongi and Chieffi [2006]; Karakas and Lattanzio [2007]; Woosley and Weaver [1995]; Rauscher et al. [2002]; Woosley and Heger [2007]. The values by Karakas et al. correspond to calculations for AGB stars.

2.3 Production of ^{53}Mn in stars

^{53}Mn has a half life of (3.7 ± 0.4) Myr [Honda and Imamura, 1971]. During the explosive silicon burning stage of the star, ^{53}Fe is created and quickly decays to ^{53}Mn (see Fig. 2.1).

Fig. 2.3 shows the calculated yields for ^{53}Mn ejecta from three of the before cited publications [Woosley and Weaver, 1995; Woosley and Heger, 2007; Rauscher et al., 2002]. These yields are roughly up to an order of magnitude larger or similar to the ^{60}Fe yields. As for ^{60}Fe, the yields of ^{53}Mn also show a dependence on the initial mass of the star.

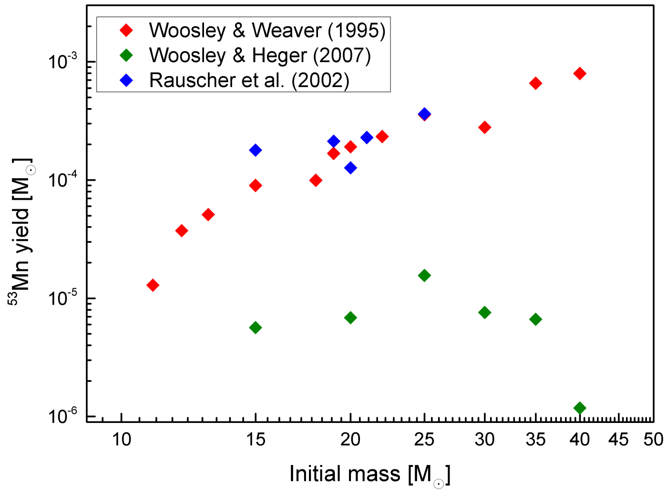

Figure 2.3. Compilation of yields of ^{53}Mn as a function of the initial mass of the star. Data taken from Woosley and Weaver [1995]; Woosley and Heger [2007]; Rauscher et al. [2002].

2.4 Cosmogenic radionuclide production

Besides being copiously synthesized in stars, both ^{53}Mn and ^{60}Fe are also produced in cosmic ray spallation reactions. Cosmic rays produce a large variety of radionuclides in meteoroids, in the Earth's or lunar surfaces and in interplanetary dust particles. This section will describe the production of ^{53}Mn and ^{60}Fe via spallation processes.

2.4.1 Cosmic ray spallation

There are two types of cosmic rays: galactic cosmic rays (GCR) and solar cosmic rays (SCR). The first type originates from outside the solar system and the second are emitted by the Sun continuously during solar flares. They are composed mainly of protons, $\sim 10\%$ alpha particles and a small $< 1\%$ of heavier nuclei ($Z > 3 \sim 90$) [Reedy et al., 1983]. GCR have high energies (hundreds to thousends MeV per nucleon), thus are capable of penetrating upto around 1 m in to matter, like rocks or meteorites. On the other hand, SCR have energies lower than 100 MeV per nucleon. They are stopped within a range of 2 cm in matter. They produce a great variety of radionuclides and noble gases, which can later on be measured in order to reconstruct the exposure history of the irradiated material.

Spallation processes are knock out reactions induced by energetic particles. The isotopes formed by these mechanisms are called cosmogenic nuclides. As they pass through matter, SCR or GCR also generate secondary particles (for example: neutron, photons, muons, ...). The number of secondary particles depends strongly on the energy and the atomic number of the incident primary cosmic particle. Because of their lower energy, SCR induced reactions produce nuclides with similar masses as the target nuclei. GCR produce a large quantity of secondary particles. Those can produce new nuclei that are further away in mass from the original target material in secondary reactions.

For a freshly exposed surface, the activities of the cosmogenic radionuclei is zero. After several half lives of exposure, the activity reaches an equilibrium or saturation. Concentrations of cosmogenic noble gas nuclides can give information about the integrated radiative history of the surface.

Theoretical model calculations for production rates of several radionuclides in meteoroids are available [see for example: Leya and Masarik, 2009; Ammon et al., 2009; Wieler et al., 2013, and references therein]. The most important factors are exposure time, size and composition of the meteorites. These calculations are often used to determine the preatmospheric size and to reconstruct the exposure history of the object [see for example Llorca et al., 2013]. For iron meteorites, the exposure time can be longer than a million years, since they are composed mainly by iron thus are very resistant to erosion and fragmentation during impacts [Choppin et al., 2002].

2.4.2 Cosmogenic ^{60}Fe production

^{60}Fe is mainly produced in nickel targets. The cross section for the ^{nat}Ni(p,x)^{60}Fe reaction was measured for proton energies between 33.5 MeV and 2.6 GeV by Merchel et al. [2000].

Leya and Masarik [2009] calculated the production rate in stony meteoroids. For objects with a radius smaller than 60 cm, the production rate increases towards the center of the meteoroid, but for larger radius, the production reaches a maximum of 0.7 dpm/kg Ni (disintegrations per minute per kilogram nickel) near the surface and then decreases. Ammon et al. [2009] did similar calculations for iron meteorites. For bodies with radius smaller than 40 cm, the production rate increases towards the center of the meteoroid. For larger ones, the production rate reaches a maximum towards the surface and then decreases. Their predictions, however, seem to underestimate the measured values.

2.4.3 Cosmogenic ^{53}Mn production

The principal targets for ^{53}Mn production are iron and nickel. The cross section for the reactions $^{\mathrm{nat}}$Fe(p,x)^{53}Mn and $^{\mathrm{nat}}$Ni(p,x)^{53}Mn for protons with energy between 17 MeV and 2.6 GeV have been measured and are in the range of tens to 200 mb [Merchel et al., 2000].

Production rates for ^{53}Mn depend strongly on the energy, hence on the range of the cosmic rays. On the lunar surface, the rate due to GCR is maximum in a depth of approximately 20 cm [Reedy and Arnold, 1972; Leya et al., 2001]. Since the SCR have lower energies, they dominate the production in the upper centimeter. Summing up both contributions, the production rate has a maximum at the lunar surface, then decreases steeply in the next centimeters, then reaching a plateau between 10 and 50 cm.

In meteorites, the dominant contribution to the total production rate of ^{53}Mn are also due to the secondary neutrons created by the primary GCR. For a detailed description in this matter, the reader is referred to Leya and Masarik [2009] and Ammon et al. [2009].

Chapter 3

Experimental setup and measurements

Contents

After the description of the production of the isotopes studied in this work, this chapter will describe the technique used to detect them, namely accelerator mass spectrometry (AMS). Since the measurements that are the foundation of this work were performed at the GAMS (Gas-filled Analyzing Magnet System) facility in the Maier-Leibnitz Laboratory (MLL) in Garching, Germany, this system and its features will be described in detail in the second section of this chapter, after a brief general introduction of the technique itself. The last section will be dedicated to the description of the measurements.

3.1 Accelerator Mass Spectrometry

The origin of this technique can be traced back to 1939, when Alvarez and Cornog successfully showed using a cyclotron that ^{3}He is stable [Alvarez and Cornog, 1939a] and tritium (^{3}H), its isobar, is radioactive [Alvarez and Cornog, 1939b]. Almost four decades later the counting of single ^{14}C atoms instead of decays has been shown to improve the dating accuracy [Muller, 1977]. The extension to other isotopes and new applications soon followed, and the term *accelerator mass spectrometry* (AMS) began being used to refer to this technique.

In principle, a conventional mass spectrometer can distinguish between different isotopes of the same element. To do so, first the atoms with the mass M are ionized, accelerated with an electrostatic potential V and analyzed by a magnetic field B. The radius of their trajectory ρ is determined by the *magnetic rigidity*:

$$B\rho = \frac{p}{q} = \frac{\sqrt{2ME + E^2/c^2}}{q} \tag{3.1}$$

with the kinetic energy E, momentum p, charge q and c the speed of light in vacuum. Nevertheless, this method is limited by the presence of interfering isobars, being atoms or molecules with the same mass.

AMS is an ultra-sensitive method for determining isotopic ratios using an accelerator. With it, higher energies than in regular mass spectrometers are achieved, allowing the complete suppression of molecular background by stripping off several electrons and the use of nuclear physics techniques for isobar separation and ion identification. Although the first measurements were performed with a cyclotron, linear electrostatic accelerators (mostly tandems) are preferred.

To this date there are over 70 AMS facilities worldwide [Fink, 2010] that are capable of measuring concentrations of approximately 40 different radioisotopes with half lives up to 10^9 years. Fig. 3.1 shows a plot of the radioisotopes measured via AMS up to this date, organized according to their half lives and masses.

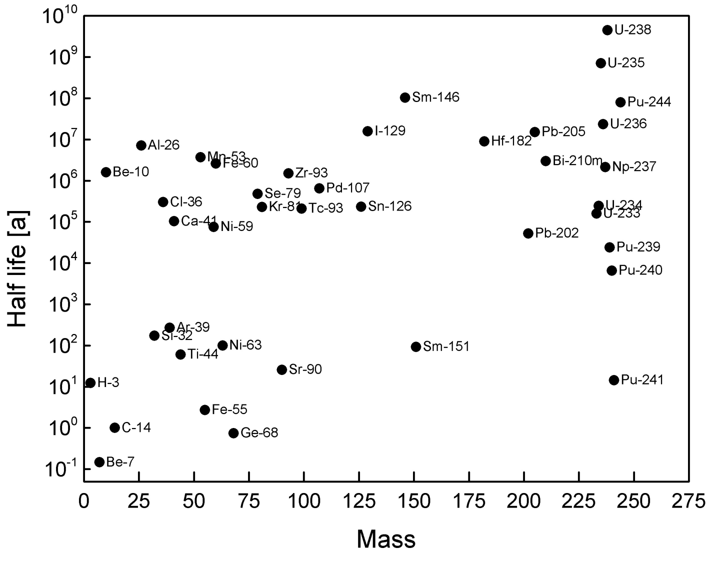

Figure 3.1. Radioisotopes measured via AMS, updated from Fink [2010].

3.2 AMS facility GAMS in Garching

The ^{60}Fe and the ^{53}Mn data discussed in this thesis were obtained at the Maier-Leibnitz Accelerator Laboratory (MLL) in Garching, Germany, and the ^{26}Al and ^{10}Be data at PRIMELab in Purdue University in West Lafayette, Indiana, United States. While heavy nuclei like ^{60}Fe and ^{53}Mn are only measurable with large facilities like the tandem in Garching (in order to achieve the necessary isobaric suppression), lighter radionuclides are routinely measured with smaller machines. This section will be dedicated to a detailed description of the GAMS setup at MLL, schematically shown in Fig. 3.2. In short, singly charged negative ions leaving the ion source are deflected by a 90° injection magnet that performs a first mass separation. After a 18° electrostatic deflection that performs an energy selection, the ions enter the low energy side of the accelerator. In the center, by passing through a thin carbon foil (~ 4 g/cm^2), a stripping process occurs removing a number of electrons. The ions are now positively charged and are further accelerated. In the stripping process all molecular background is removed, because highly charged molecules are unstable and undergo a so-called Coulomb explosion. The beam is once again deflected by a 90° analyzing magnet and directed to the experimental beamline. There are two beamlines exclusively dedicated to AMS at the MLL. Only the one used for this work will be described here, also explaining its operating principle.

3.2.1 Ion source and injector magnet

There are different processes that can be used for the production of negative ions that are necessary for injection into a tandem accelerator, but sputtering is chosen in most of the cases for AMS, because it can be very versatile in terms of the ion species that can be generated. A Middleton type ion source [Middleton, 1983], is chosen in most AMS laboratories. In this case, cesium vapour coming from a heated reservoir is directed to a volume containing an ionizer surface (usually tantalum) and the target (see Figs. 3.3 and 3.4). When a cesium atom, which has a low ionization energy (3.89 eV), comes in contact with a hot surface ($\sim 1000°$C) of a material with high work function, it is positively ionized and accelerated towards the sputter target, by means of a *sputtering* voltage of -6 kV. Because the ionizer and the sputter target share the same volume, but the target has a considerably lower temperature as the ionizer, a Cs layer is condensed on the target surface. It has been shown [Krohn, 1962] that this reduces the work function and increases the negative ion yields. The ionizer consists of two half-spherical tantalum structures, which is indirectly heated. This allows for a precisely focused Cs$^+$ beam

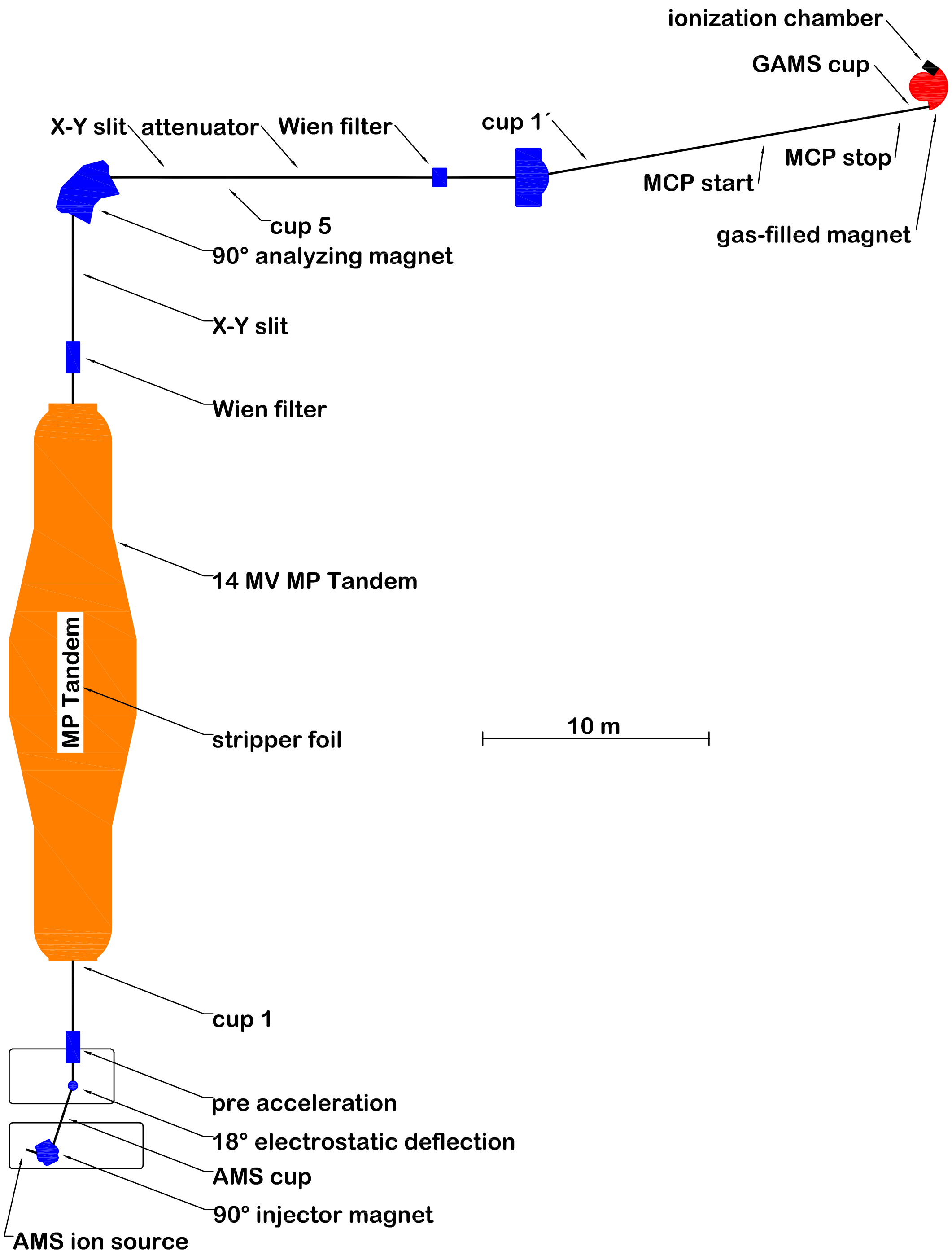

Figure 3.2. Schematic view of the GAMS facility of the Maier-Leibnitz-Laboratory.

sputtering of the target [Korschinek et al., 1986].

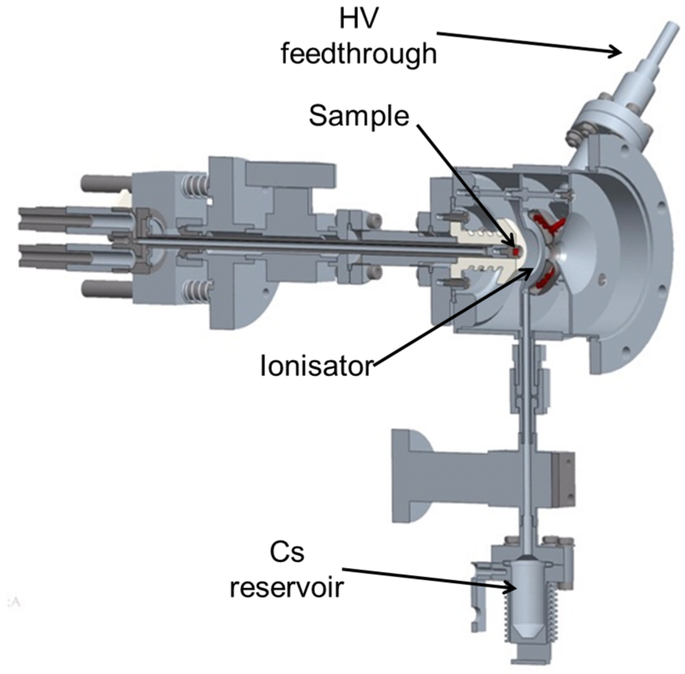

Figure 3.3. Schematic drawing of the ion source. (Courtesy of P. Hartung.)

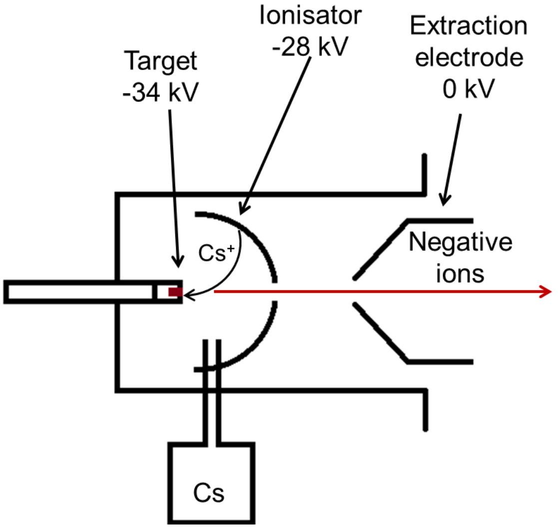

Figure 3.4. Heated cesium vapor enters the ion source, is positively ionized, and accelerated to the sample with a sputtering voltage of 6 kV. The negative ions originating from this process are accelerated first due to the sputtering voltage and after due to the extraction voltage (28 kV).

The target holder consists of a high purity silver cone (Alfa Aesar, 99.99% EG-Nr.:231-131-3), with a hole drilled in the center (diameter 1.5 mm, depth ∼ 2 mm). The sample material, after being mixed with silver powder to improve the thermal and electrical conductivity, is hammered into the hole. The singly charged negative ions are then accelerated by the sputtering voltage and further accelerated from the source with an *extraction* voltage of 28 kV.

The first step of isobar suppression can happen in the ion source. On account of iron having a smaller electron affinity than nickel (0.16 eV and 1.156 eV, respectively), but the oxides having similar values (1.49 eV for FeO^- [Drechsler et al., 1997] and 1.45 eV for NiO^- [Ramond et al., 2002]), for ^{60}Fe measurements the molecular anions are extracted. Since manganese has a negative electron affinity, it cannot form negative ions at all. For this reason, for ^{53}Mn measurements all samples are prepared as oxides and MnO^- is extracted from the ion source.

At the AMS facility at MLL there is a dedicated injection system used for AMS only. Ion sources, like the one shown in Fig. 3.3, are changed and thoroughly cleaned between beam times to avoid *cross-talk* contamination.

Right after the extraction from the ion source, a first mass separation of the ions is performed with a 90° injector magnet. The mass resolution of this device is around $\Delta M/M \sim 1/300$ and the maximal field achievable is 1.2 T. The injector magnet field is set to maximize the current measured in a Faraday cup located before the 18° electrostatic deflector (AMS cup in Fig. 3.2).

3.2.2 Tandem accelerator

The majority of the AMS measurements has been realized using a tandem accelerator mainly because of:

- Availability: old machines, built originally for nuclear physics experiments, became available for refurbishing and adapting for AMS experiments. Nowadays, small machines (*i.e.* low terminal voltages) can be purchased.
- Versatility: tandem accelerators can accelerate a great variety of beams with little changes in the settings.
- Background reduction: due to the stripping process occurring in the middle of the accelerator, all molecular background is destroyed by cause of Coulomb explosions.

The tandem accelerator of the Maier-Leibnitz Laboratory, a joint research installation of the Ludwig-Maximilian Universität (LMU) and the Technische Universität München (TUM), was put into operation in 1970 [Jahresbericht, 1970].

After gaining 150 keV in the preacceleration section (see Fig. 3.2), the singly charged negative ions enter the 14 MV tandem accelerator. The ions are then accelerated towards the positive terminal. There they are stripped of a number of electrons as they pass through a 4 μm/cm^2 thick carbon foil, thus become positive and are accelerated away from the terminal. It is in this stage where the molecular background is completely suppressed. This interaction also causes a charge state distribution that is calculated following Shima et al. [1992]. The energy of the ions is now

$$E = \left((V_P + V_T) \frac{m_+}{m_-} + qV_T \right) e \tag{3.2}$$

where V_P and V_T are the preacceleration and terminal potential, respectively, m_- is the mass of the injected ion, m_+ the mass of the positive ion (which can differ from the latter if one injects molecular ions), q its charge state after the stripping of electrons and e is the elemental charge.

3.2.3 Beamline description

After exiting the tandem, the magnetic rigidity (see Eq. 3.1) is defined by the analyzing magnet (see Fig. 3.2), whose maximal field is 1.45 T and a maximum mass resolution of ΔM/M $\sim$ 1/3000. However, ions of different mass and charge state can have the same magnetic rigidity, thus can generate background and/or high count rates that interfere and overload the detector at the end of the beamline. To avoid this one can use a Wien filter (velocity filter), which consist of an electric and a magnetic field ($\mathcal{E}$ and $\mathcal{B}$, respectively) with direction perpendicular to each other and to the direction of the beam. Only ions with velocity

$$v = \frac{\mathcal{E}}{\mathcal{B}} \tag{3.3}$$

pass through. As the magnetic rigidity of the ions is defined, this device works also as a mass filter. The GAMS setup has two Wien filters located one before the analyzing magnet and one after (approximate location indicated in Fig. 3.2). Their mass resolutions are ΔM/M $\sim$ 1/80 and ΔM/M $\sim$ 1/40, respectively. Usually, the magnetic field is fixed throughout the experiment and only the electric field is changed. To find the optimal settings, the current of a stable reference isotope is optimized in a Faraday cup located after the Wien Filter (cup 5 in Fig. 3.2). A *switching magnet* is used to select the experimental beamline.

3.2.4 Gas-filled magnet and split anode ionization chamber

Further isobar separation can be accomplished with a gas-filled magnet [see for example Knie et al., 1997]. The magnet chamber is filled with N_2. During the interaction of the ions with the atoms of this gas a charge state distribution develops. The ions reach a mean charge state $\langle q \rangle$ that depends on their atomic number and velocity*. Thus, isobars, having the same mass but different atomic numbers, develop a different mean charge state. This is schematically shown in Fig. 3.5.

A photograph of the magnet of the GAMS facility is shown in Fig. 3.6. The 135° magnet, with a mean deflection radius of 85 cm and a gap between the poles of 7 cm, has a maximum field of 1.25 T. This is enough to bend ions with $A \leq 130$. The path length of the ions in the gas is 2.20 m and its ~ 90% covered by magnetic field. The spatial separation of two ions with different magnetic rigidity is $\Delta x = 1.55$ cm/%(Bρ). A detailed description of the features of it can be found in Knie [1997] and Knie et al. [1997].

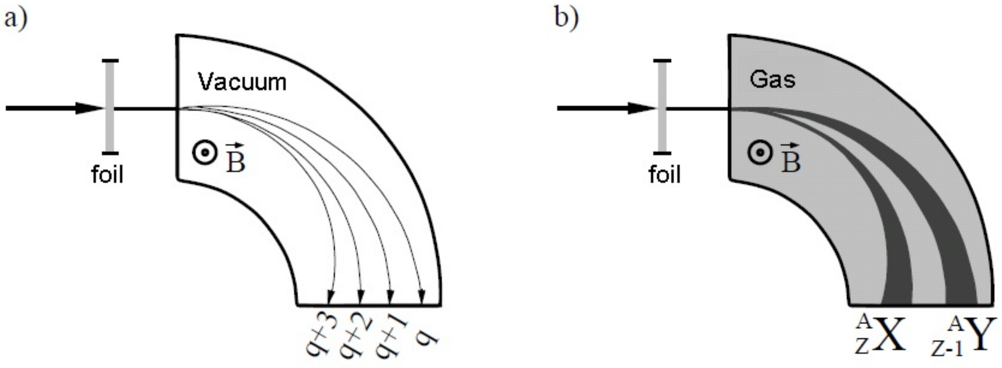

Figure 3.5. Principle of function of the gas filled magnet. If the magnet chamber is under vacuum (a), the ions are deflected only according their charge state. Under a weak gas atmosphere (b), isobar separation is accomplished.

At the exit of the magnet chamber there is an ionization chamber (see Fig. 3.7). Its anode is split into 5 sections perpendicular to the direction of the beam. The first two sections are also divided diagonally, which allows to measure the x position of an ion

---

*Due to a partial cancellation of the velocity there is only a weak velocity dependence of the magnetic rigidity.

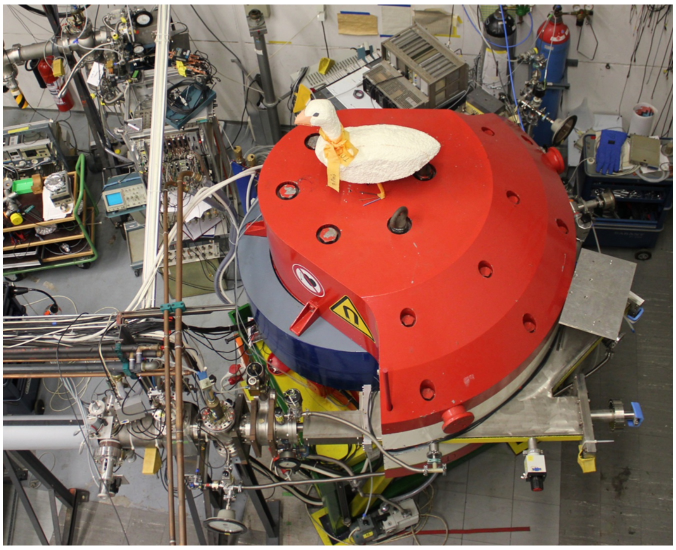

Figure 3.6. Photograph of the gas filled magnet.

at the entrance of the detector, by obtaining a signal from the left and the right part independently. From the drift times in the first and the third segment it is possible to calculate the angle in the y-direction and using the four diagonal sectors it is possible to obtain information about the x-direction. The ionization chamber is filled with isobutane (C_4H_{10}). The Frisch grid is capacitively connected to the cathode, collecting a signal proportional to the total energy loss in the chamber. The cathode and the Frisch grid are supplied with -700 V and -280 V, respectively, and the anode is connected to ground.

The differential energy loss is described by the Bethe-Bloch formula[*]

$$\left(\frac{dE}{dx}\right)_{e^-} = -4\pi \frac{Z_p^2 e^4}{m_e v_p^2} n \ln\left(\frac{2m_e v_p^2}{I}\right) \tag{3.4}$$

where Z_p is the atomic number of the ion going through the material, v_p its velocity, n is the electronic density of the stopping material and I the effective ionization potential (of the order of $\sim$13 eV). Neglecting the variations in the logarithmic term, this can be approximated by the expression

$$-\frac{dE}{dx} \propto \frac{m_p}{E} Z_p^2 \tag{3.5}$$

To determine the optimal gas pressure inside the magnet, one has to take the energy loss in the ionization chamber into account too. Since the isobar separation in the ionization chamber is better at higher energies, the pressure in the magnet chamber

---

[*] non relativistic form

cannot be too high, as the ions would loose to much energy before entering the detector. Typical values for the experiments done for this work were ∼45 mbar isobutane in the ionization chamber and ∼5 mbar nitrogen in the magnet. The volumes between the gas-filled magnet and the beamline are separated by a 0.9 μm mylar foil. The entrance window of the ionization chamber is a 2 μm aluminized mylar foil.

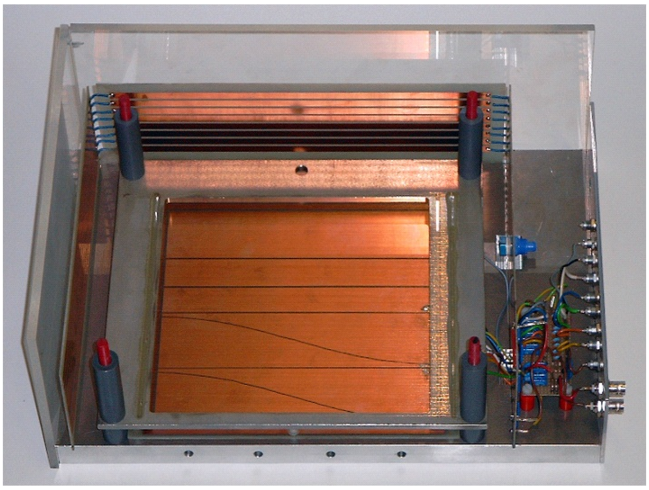

Figure 3.7. Photograph of the ionization chamber.

3.3 Measurements

This section will describe the typical measuring procedure. The quantity of interest is the concentration of the radioisotope relative to a stable isotope of the same element. In general, this is obtained by counting the events from the radioisotope and by measuring a macroscopic current of its stable counterpart. The measurement of the ratio of ^{53}Mn/Mn or ^{60}Fe/Fe is in principle very similar. At first, the system is tuned with a stable beam (^{55}Mn or ^{54}Fe). The tuning is performed by sequentially maximizing the current on different Faraday cups along the beamline. After this is finished, the electrostatic elements (tandem voltage and Wien filters) are changed for the radioisotope of interest, and a standard sample (of known concentration) is measured. This is followed by a blank sample (a sample with no radioisotopes) for background measurement and afterwards the real samples. In this way, the isotopic ratio is determined relative to the standard sample. Although this has the big advantage of being independent from any transmission factors, the resulting concentration can only be obtained to the degree of precision that the concentration in the standard sample material is known.

3.3.1 Beam tuning

The first step is the tuning of the system with a stable beam. To do so, a blank sample is used. The blank samples consist of MnO_2 or Fe_2O_3 mixed with silver powder, pressed into a high-purity silver sample holder. It has been shown, that similar Ag powders rated the same purity level have different contents of chromium [Meier, 2006] and ^{53}Cr has to be avoided as it is the isobaric background. This is the reason why a particular powder is used for preparing the MnO_2 samples (Aldrich Chem. Co. Nr:7440.22,4).

Firstly, the field of the injector magnet is set to maximize the current in the AMS Faraday cup (see Fig. 3.2). In both cases single oxides are extracted from the ion source. Typical currents in the AMS cup are in the order of 0.6 μA of ^{55}MnO^{-} and 2 μA of ^{56}FeO^{-}. The next step is to tune the beam in the Faraday Cup 1, located before the entrance to the tandem accelerator. The energy of the ions is fixed by the field of the analyzing magnet, the tandem voltage is then adjusted to optimize the current in the Faraday cup 5. Once the beam is tuned through the entire beamline, the Wien filters are switched on. The magnetic fields are fixed and the electric fields are optimized measuring the current in cup 5 and the last cup of the line, located before the entrance of the gas-filled magnet (GAMS cup in Fig. 3.2). At this point, the magnetic rigidity on the high energy side of the accelerator is not changed anymore. In this way, any hysteresis effects can be avoided.

After this procedure is done, the terminal voltage is set to the radionuclide. Since in the so called low energy part of the accelerator, *i.e.* from the ion source up to the terminal, the beam is solely focused with electrostatic elements, except for the injector magnet, this tuning is valid for ions having the same E, thus have no dependence on the mass. The field of the injection magnet is changed according to

$$B_{\mathrm{rad}} = B_{\mathrm{st}} \sqrt{\frac{m_{-}^{\mathrm{rad}}}{m_{-}^{\mathrm{st}}}} \tag{3.6}$$

with B_{rad} and B_{st} the fields for the radioactive and the stable isotopes, respectively, and m_{-}^{rad} and m_{-}^{st} the masses of the injected molecular ions.

On the high energy side of the tandem, the magnetic rigidity of the ions is fixed, and the terminal voltage and the electric fields of the Wien filters have to be changed. The equation for the velocity filters is

$$\mathcal{E}^{\mathrm{rad}} = \mathcal{E}^{\mathrm{st}} \frac{m_{+}^{\mathrm{st}}}{m_{+}^{\mathrm{rad}}} \frac{q^{\mathrm{rad}}}{q^{\mathrm{st}}} \tag{3.7}$$

where m_{+}^{st} and m_{+}^{rad} are the masses of the different ions, q^{st} and q^{rad} their charge states and $\mathcal{E}^{\mathrm{st}}$ and $\mathcal{E}^{\mathrm{rad}}$ are the values for the voltage of the power supplies of the electric fields for the stable and the radioactive ions, respectively.

3.3.2 Sample Measurements

After the tuning process for both the stable and the radioactive isotope is finished, one can start with a routine AMS measurement. The first thing to do is to measure a sample with a known concentration of the radioisotope, a standard, in order to be able to correctly identify the isobars in the spectra and set the appropriate values for the magnetic field and pressures in the gas-filled magnet and in the detector. In addition, the magnetic field of the GAMS is adjusted to accept the radioisotope and to prevent part of the isobar from entering the detector, in order to reduce the dead-time, by keeping the countrate low ($\lesssim$ 1 kHz). After that, a blank sample (with no radioisotope) is measured long enough to get a good sensitivity level. Afterwards, an unknown sample can be measured. The desired concentration of the radioisotope can be calculated using the formula:

$$C = \frac{N \times e \times q}{T \times I_{st} \times t} \tag{3.8}$$

with N the number of counts of the radioisotope, e is the elemental electric charge, q is the charge state, T is the transmission from the GAMS cup (see Fig. 3.2) to the detector, I_{st} the current of the reference stable isotope and t the measuring time, corrected with the dead time of the measurement. The transmission T is determined with the measurement of the standard sample:

$$T = \frac{N \times e \times q}{I_{st} \times t \times C_{STD}} \tag{3.9}$$

with C_{STD} the concentration of the standard sample.

3.3.2.1 ^{53}Mn measurements

The interfering isobar of ^{53}Mn is ^{53}Cr, the second most abundant isotope of chromium (9.5%) (see Fig. 2.1). The spectra shown in Fig. 3.8 are typical measurements. The ^{53}Mn related events can be easily identified in Fig. 3.8(a), although the presence of ^{53}Cr is considerably strong. To determine how ^{53}Cr background which mimics ^{53}Mn in the detector, a MnO_2 sample spiked with $\sim$ 1000 ppm of chromium was measured during the experiments. With these spectra it is possible to estimate the chromium suppression (by means of the data analysis software, see Appendix A). For the measurements of this work, this was a factor of ∼ 10^4.

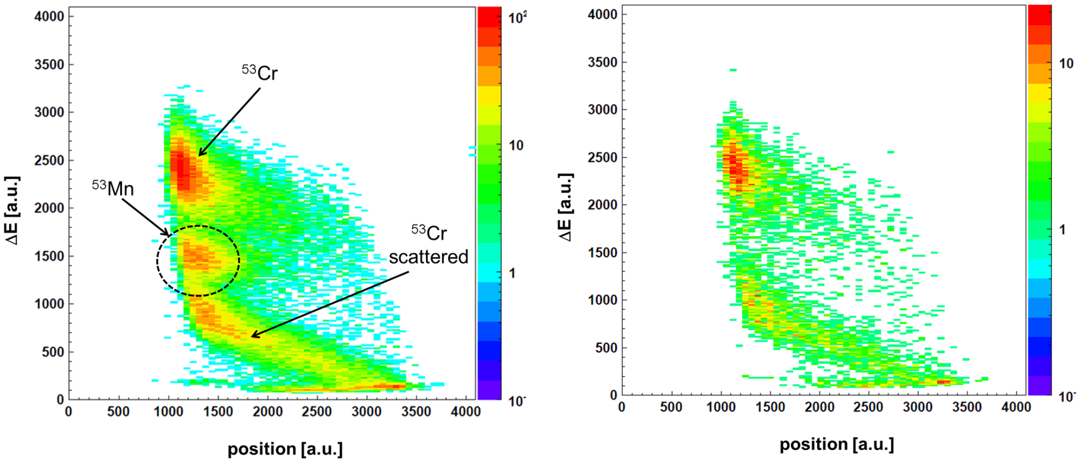

(a) (b)

Figure 3.8. Two dimensional spectra ΔE - position of (a) a ^{53}Mn standard sample, and (b) a blank sample. The background is dominated by ^{53}Cr. Some of it is scattered in the slits before the entrance in the detector.

The standard sample used is named Grant GLS[*] [Poutivtsev, 2007; Poutivtsev et al., 2010]. This sample originates from the Grant iron meteorite and its ^{53}Mn concentration was determined from its activity by the measurement of K_α and K_β lines from ^{53}Cr. This concentration is $^{53}\mathrm{Mn}/\mathrm{Mn} = (2.83 \pm 0.14) \times 10^{-10}$. The uncertainty of this value comes mainly from the uncertainty of the half-life of ^{53}Mn, where $T_{1/2} = (3.7 \pm 0.4) \times 10^6$ yr has been used.

The ionization chamber was filled with 45 mbar of isobutane and the GAMS with 5.0 to 5.5 mbar of nitrogen. The value of the magnetic field in the GAMS was varied between 794 and 806 mT in different runs. The manganese ions lose, under these conditions, aproximatelly 30% of their initial energy of 144 MeV in the gas-filled magnet and enter with ∼ 100 MeV in the detector.

A typical scenario for the isobaric separation in the GAMS can be seen in Fig. 3.9. The top part of the figure shows a graph of the mean magnetic rigidity of the isobaric pair ^{53}Mn - ^{53}Cr, calculated with the semi-empirical formula of Sayer [1977]. The relative difference between the two is displayed in the bottom half of the same figure. It is then clear that high energies are here necessary in order to get a good separation of both

---

[*] General Laboratory Standard

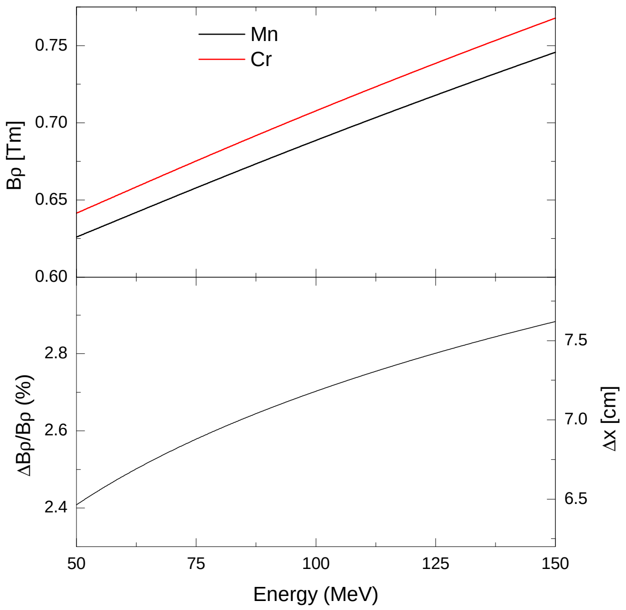

Figure 3.9. Magnetic rigidity of ^{53}Mn and ^{53}Cr as a function of the energy (top part) and their relative difference (bottom part), calculated with the mean charge state of the ions, according to the formula of Sayer [1977].

isobars*. For this reason, the experiments were performed with a rather high terminal voltage available under stable conditions of the tandem. For both stable and radioactive isotopes, the charge state $q = 11$ was chosen. The energy of the ^{53}Mn was 144 MeV ($V_T = 12.300$ MV) and for ^{55}Mn 139 MeV ($V_T = 11.847$ MV) and the stripping yields for the charge state 11^+ are 14 % and 12 % respectively. Typical transmission between cup 1 and GAMS cup was about 30 %. The transmission through the GAMS, as calculated from Eq. 3.9, was between 30 % and 45 %, depending on the conditions applied for the settings of the software cuts. The sensitivity achieved was 1×10^{-13}. Higher sensitivities (in the order of $\times10^{-15}$) are possible [Poutivtsev et al., 2010], but were not necessary in the experiments performed during this thesis, since the concentration of the samples to be measured were, on average, 2 orders of magnitude higher.

---

* The separation also depends on the width of the distributions.

3.3.2.2 ^{60}Fe measurements

^{60}Ni is the interfering isobar of ^{60}Fe. With 26.6 % natural abundance it is the second most abundant isotope of nickel. The difference of 2 in the nuclear charge of this isobaric pair makes the measurement simpler than the measurement of ^{53}Mn. Fig. 3.10 show examples of the spectra taken. The events related to ^{60}Fe in Fig. 3.10(a) can be nicely separated from the background.

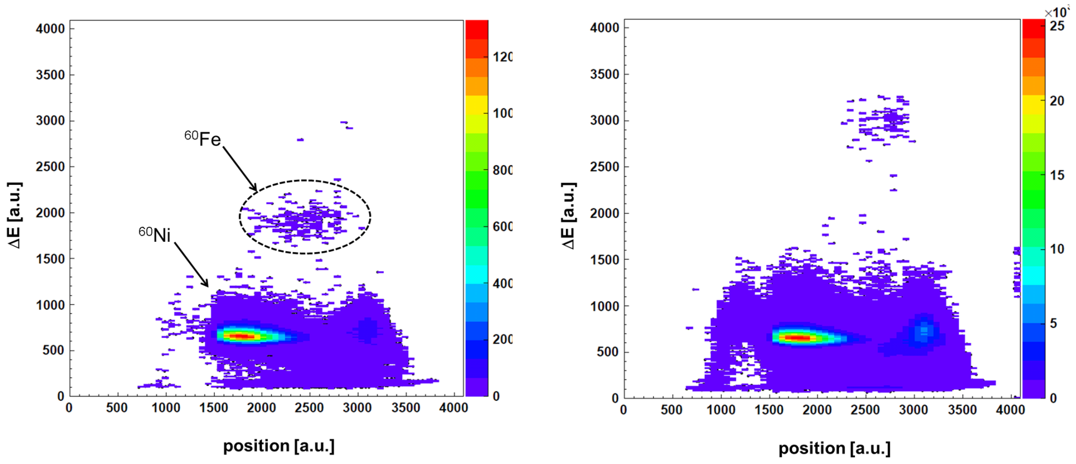

(a)

(b)

Figure 3.10. Two dimensional spectra of (a) a ^{60}Fe standard sample and (b) a blank sample. The background is dominated by ^{60}Ni.

As standard material, diluted Fe_2O_3 extracted from a beam dump from the 590 MeV proton accelerator of the Paul Scherrer Institute in Switzerland [Schumann et al., 2009], was used. The concentration of ^{60}Fe was directly determined in the same way as described in Rugel et al. [2009] and it was then diluted to obtain two different reference materials. The one used for this work has a concentration of $^{60}\mathrm{Fe}/\mathrm{Fe} = (1.25 \pm 0.06) \times 10^{-12}$.

The graph in Fig. 3.11 shows the magnetic rigidity of the isobaric pair ^{60}Fe -^{60}Ni in the top part and its difference in the bottom half, calculated once again with the semiempirical formula of Sayer [1977]. As the difference between them (bottom half of the graph in this figure) is higher than for ^{53}Mn - ^{53}Cr, the measurement is easier. Nevertheless, high energies are desired in order to get a better isobaric separation.

For these measurements, the terminal voltage was 12.5 MV. The charge state chosen for the radioisotope was $q = 11$, with a yield of 21 % and an energy of 150 MeV. As reference isotope, ^{54}Fe is chosen with a charge state of $q = 10$ and energy of 138 MeV. Although this isotope is the second most abundant of iron, with only 5.8 %, its choice

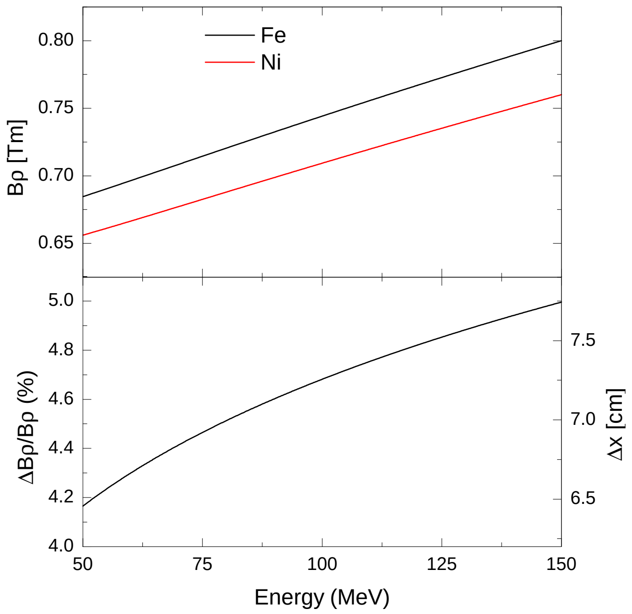

Figure 3.11. Magnetic rigidity of ^{60}Fe and ^{60}Ni as a function of the energy (top part) and their relative difference (bottom part). The difference of 2 in the atomic number results in a better relative separation between this isobaric pair than for ^{53}Mn - ^{53}Cr.

is justified because the m/q ratio is close to 60/11 (as in the measurement with the radioisotope), what requires only a small change the settings in the tandem and Wien filters in order to measure the current between runs. The stripping yields are 21% and 19% for the unstable and stable isotope, respectively. The transmission through the accelerator was on the order of 40 - 60 %. For the measurements of this isotope, the ionization chamber was operated with 42 to 45 mbar of isobutane and the GAMS with 5.2 mbar of nitrogen. The magnetic field was 880 mT. Under this conditions the ions lose about 30% of their energy passing through the GAMS.

CHAPTER 4

Sample description

Contents

This chapter will be dedicated to a detailed description of the samples, both the meteorites used as reference for the expected galactic cosmic ray production of ^{53}Mn and ^{60}Fe and the lunar samples. The lack of atmosphere makes the Moon to a unique reservoir for the search of supernova debris. Additionally, because sedimentation rates are negligible, most of this material is expected to be found in the top centimeters of the lunar surface. As the concentration of Ni on the Moon is in general very low, a high in-situ production of ^{60}Fe via spallogenic reactions is not expected.

On the other hand, ^{53}Mn is produced in lunar material, mostly via spallation on iron targets. This isotope, along with the also in-situ produced ^{26}Al, can be used to study the exposure history of Moon samples, as well as the *gardening* of the lunar surface. Gardening is referred to as the process of mixing of the regolith due to stochastic impacts of micrometeorites.

4.1 Lunar samples: Apollo missions and sample collection

Apart from the Earth, the Moon is the only body in the planetary system that has been methodically sampled. A total of 6 manned missions of the Apollo Program landed on the Moon (see approximate landing sites in Fig. 4.1 and 4.2) and collected a total of 381.7 kg of sample material.

However, only a fraction of this is available for studies and unfortunately, not all samples are well suited for this work. There exist several different types of samples [Heiken et al., 1991]:

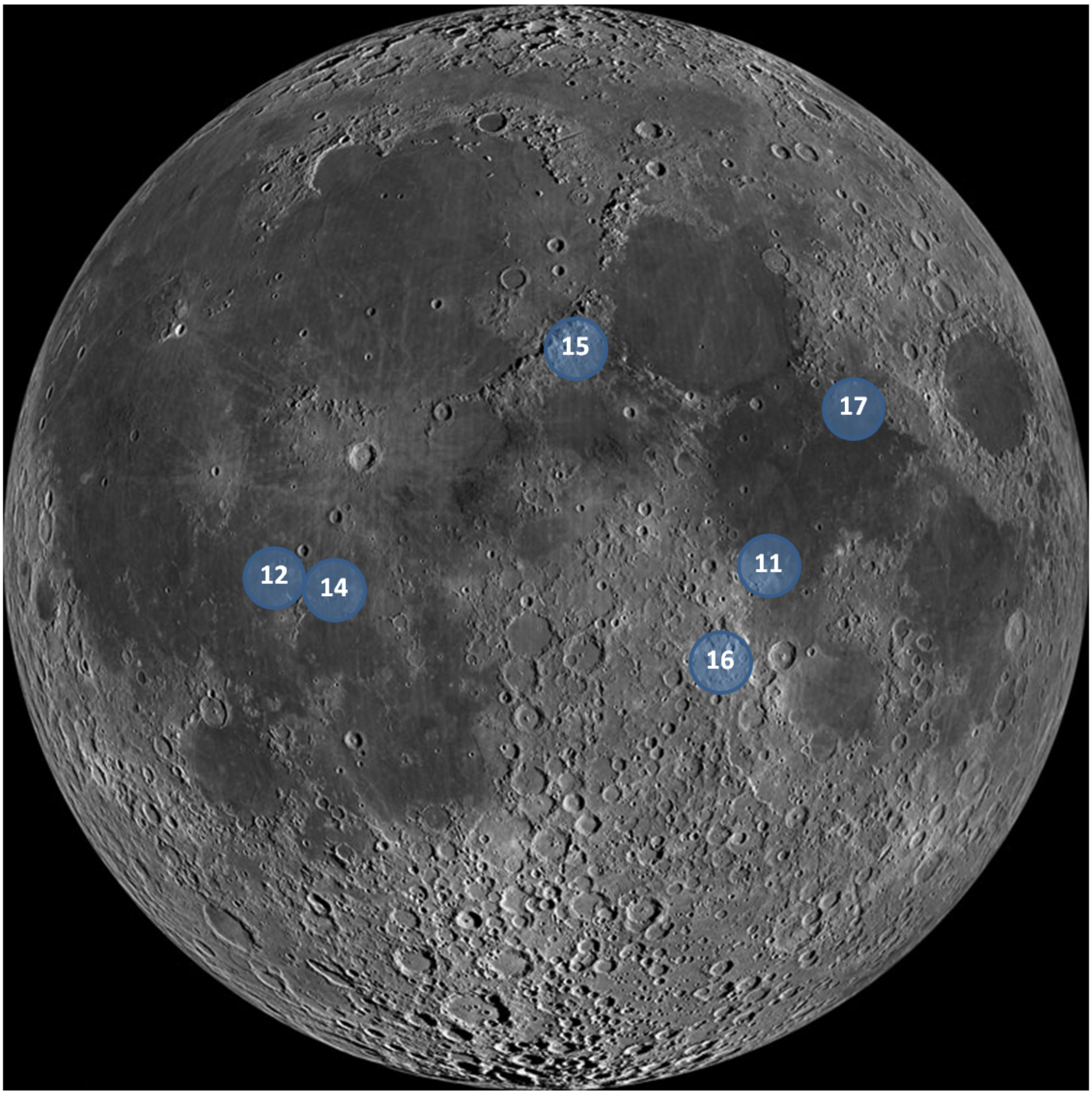

Figure 4.1. Image of the Moon including the approximate landing sites of the Apollo missions. Modified from LROC [2011].

- Contingency samples: These samples where quickly collected, without documenting their position or taking care on selecting them. The sole purpose of this type of sampling was to ensure the return of some lunar material if the exploration of the lunar surface would have had to be aborted. This procedure was performed during the first four Apollo missions.

- Bulk samples: This type of sample was only collected during the Apollo 11 mission and consist of around 38 kg of regolith scooped from different locations near the lunar module, combined as a single sample.

- Rake samples: Using a rake as collecting tool, astronauts from the Apollo 15 and later missions collected rocks bigger than 1 cm across, representing the population of a few square meters of the lunar surface.

- Cores: There exist a total of 21 cores collected from the lunar surface, representing only 5.2% of the total mass sampled. They are extremely valuable, since only they carry information about the stratigraphy of the lunar surface. In order to obtain core samples, astronauts hammered or pushed drive tubes into the lunar surface. In the later missions they used a battery-powered drill to collect deeper samples.

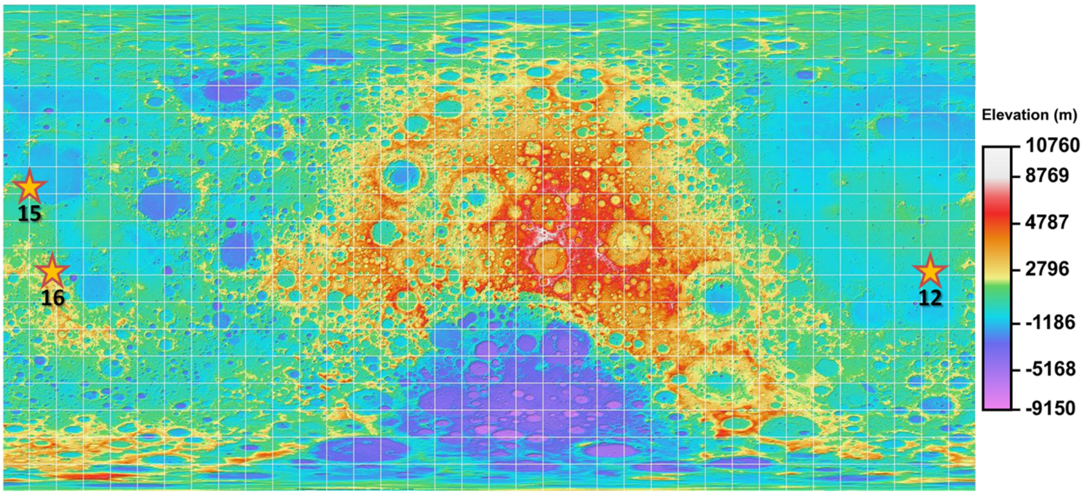

Figure 4.2. A topographic map of the Moon, obtained by the the Lunar Reconnaissance Orbiter Camera from the Arizona State University [LROC, 2011]. The stars indicate the approximate landing sites of Apollo 12, 15 and 16 missions.

Samples from the Apollo missions are numbered as follows. Each sample is identified with a three-part number. The first part is a 5 digit generic number, whose first two digits indicate during which Apollo mission the sample was collected (for the last two missions only the first digit was used). Then follows a specific number, providing a unique identification for each subdivision of a sample. For some cases, for example for the core samples, an extra parent number is needed to unambiguously identify the sample. Specific and parent numbers have between 2 and 4 digits. The complete identification number for each sample is the succession of the generic, parent, and specific numbers separated with a comma.

In this section a detailed history of each sample chosen for this work will be described, including previous measurements done on each sample.

4.1.1 Apollo 12 samples

The Apollo 12 mission was the sixth manned flight of the NASA Apollo program and the second to land on the Moon, on November 19th, 1969. In two extra vehicular activities a total of 34.35 kg of material was returned to Earth. The Apollo 12 lunar module landed on the northwest rim of the 200 m Surveyour Crater. The coordinates of the landing site were 3.2° S latitude, 23.4° W longitude, on an area of the Oceans of Storm (later christened *Mare Cognitum*). Fig. 4.3 shows a map of the landing site. For our study we chose the core 12025/8. The core was obtained by hammering a drive tube into the lunar surface (see Fig. 4.4(b)), collecting 41 cm of material. The diameter is 2 cm and its bulk density is 1.92 g/cm^3 [Heiken et al., 1991]. The core was taken from the north rim of a 10 m crater, approximately 25 m south from the Halo crater. The red arrow in Fig. 4.3 indicates the approximate sampling location.

This core shows smooth ^{26}Al ($T_{1/2} = 7.1 \times 10^5$ yr) and ^{53}Mn ($T_{1/2} = 3.7 \times 10^6$ yr) depth profiles. Both isotopes are produced via spallation of SCR and GCR in the lunar surface, thus smooth profiles indicate, with different times scales, that this core was not substantially disturbed. However, Rancitelli et al. [1971] suggest that the ^{26}Al depth profile they measured (see Fig. 4.5) was consistent with a complete mixing of the soil in the Lunar surface to a depth of 2 or 3 cm (approximately 4 to 6 g/cm^2) every 10^5 years. The uniform stratigraphy of the soil of this section supports mixing to this depth, and rules out the possibility that the flat ^{26}Al gradient has resulted from recent deposition of material. At depths greater than 10 cm (19.2 g/cm^2) the concentration of ^{26}Al decrease to a relatively constant value. The value of ^{26}Al is consistent with a calculated value, assuming 2π exposure [Fuse and Anders, 1969]. Nishiizumi et al. [1979] measured a ^{53}Mn depth profile (see Fig. 4.6). Their profile showed a smooth, rapid increase with decreasing

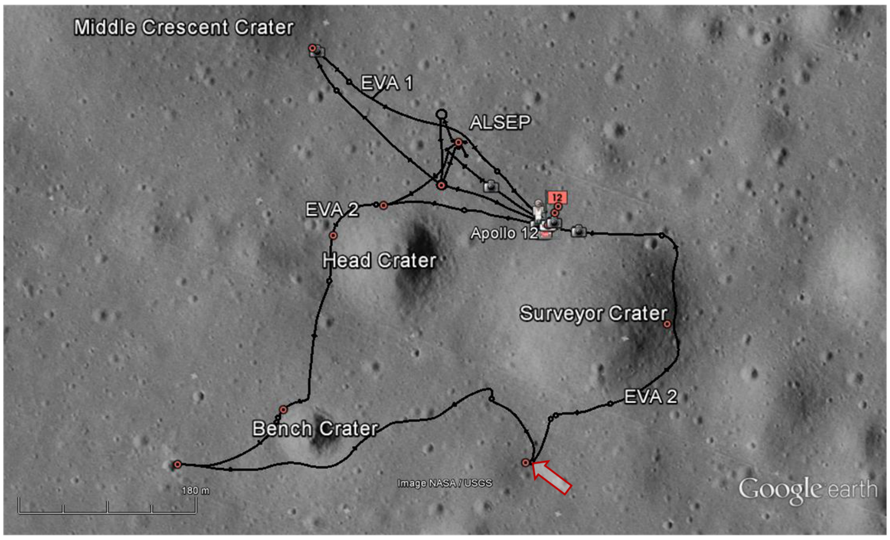

Figure 4.3. Map of the landing site of Apollo 12 including the extravehicular activities (EVAs). The red arrow indicates the approximate sampling location of the core 12025. Image taken from Google Earth V:7.1.1.1888.

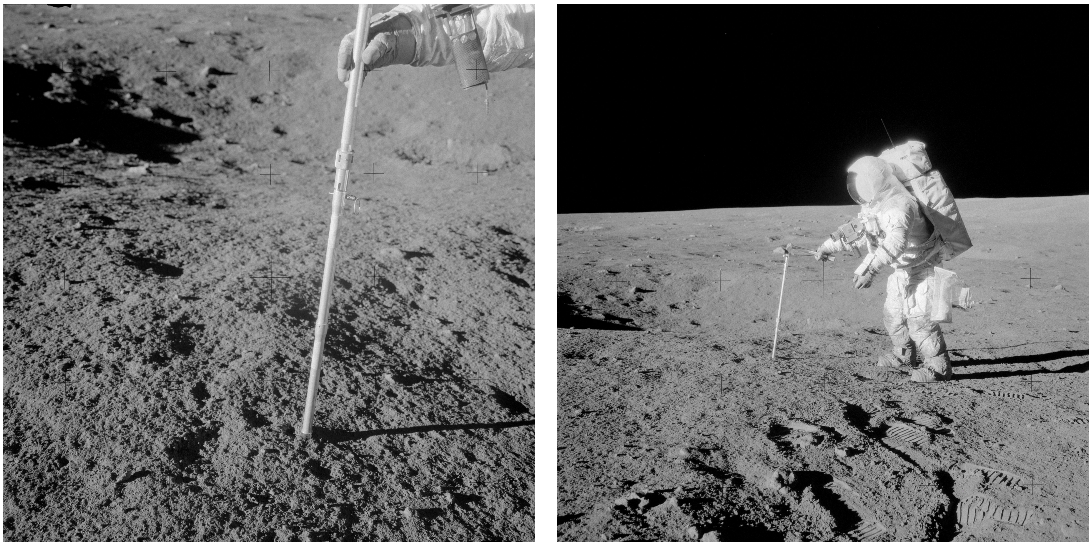

(a) (b)

Figure 4.4. Detail images of astronaut Alan Bean placing (a) and hammering (b) the double core tube 12025/8 into the lunar surface (AS12-49-7285 and AS12-49-7286).

depth from 16 to 1 g/cm^2, and then a slight decrease at the surface. They assume that this implies the addition of $\sim$ 2 g/cm^2 of material to an otherwise undisturbed core, in contradiction with the conclusion of Rancitelli et al. [1971]. Another explanation for this data is a more complex gardening history to 10 g/cm^2 [Nishiizumi et al., 1979].

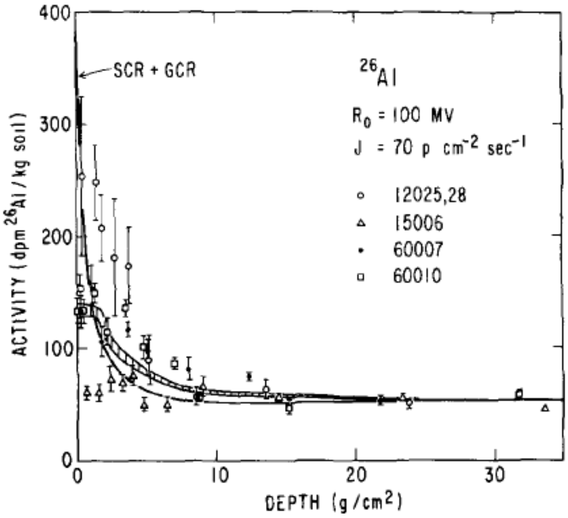

Figure 4.5. ^{26}Al activities measured. The data for 12025/8 are from Rancitelli et al. [1971], for 60010 from Fruchter et al. [1977, 1976], and for 15006 and 60007 from Fruchter et al. [1976]. The solid curve is the Reedy-Arnold calculation of an undisturbed ^{26}Al profile for the chemical composition of the Apollo 15 drill stem. The area with the vertical cross-hatching is a Moon-wide average gardened profile calculated with the model of Arnold [1975] for ^{26}Al and the same chemistry. The values are plotted at the mid-points of the depth intervals of the samples.

The integrated depth profiles of ^{26}Al and ^{53}Mn up to a depth of 10 g/cm^2 are 1.2 ± 0.1 and 1.6 ± 0.3 times greater than the ones predicted by Reedy and Arnold [1972], respectively [Nishiizumi et al., 1979]. Although the uncertainties overlap, the excess seems larger for ^{26}Al than for ^{53}Mn. One possible interpretation to this may lie in the different half lives of both isotopes and the indication that a layer was exposed long enough to become saturated in ^{26}Al but not in ^{53}Mn.

For this work a detailed ^{53}Mn profile of this core up to a depth of 74.3 g/cm^2 was measured, obtaining a good agreement with Nishiizumi et al. [1979] results, shown in Fig. 4.6. Our results are shown in Fig. 5.1(a) in chapter 5. The results of Cook et al. [2009] for the ^{26}Al depth profile also match smoothly with the previous published results by Rancitelli et al. [1971]. Fig. 4.15 in section 4.3 show new measurements done in this work, compared with the mentioned references.

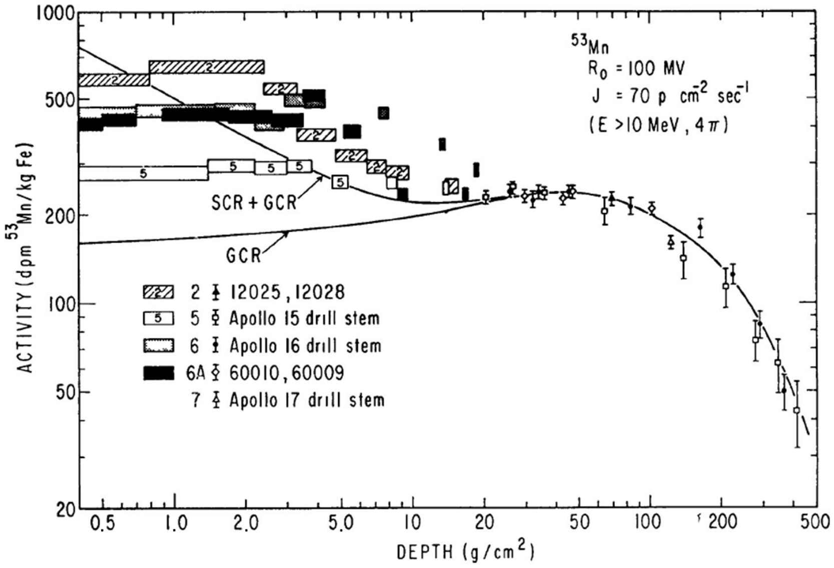

Figure 4.6. ^{53}Mn data measured in different lunar cores. The theoretical curves were calculated using the Reedy-Arnold model. The GCR curve was normalized to the data points in the 20 to 100 g/cm^2 region. As presented by Nishiizumi et al. [1979].

4.1.2 Apollo 15 samples

This was the ninth manned mission to the Moon of the Apollo program. It landed on the Moon on July 30th, 1971 and returned 77 kg of lunar material. The coordinates of the landing site are 26,1° N, 3,6° E. The mission was the first one not to land in a lunar mare, but near the Hadley Rille. It was also the first mission to use the Lunar Roving Vehicle, allowing the crew to travel much farther from the Lunar Module. In Fig. 4.7 there is a map showing the trajectories performed during the mission, spanning distances in the order of 3 km traveling to the different stations.

The samples chosen for our study are from the double drive tube 15008/7. Its total length is 56.6 cm and its diameter 4.13 cm. This tube was taken close to the rim and within the ejecta blanket of a $\sim$ 10 m diameter crater [NASA, 1972], as it can be seen in Fig. 4.8(a). Its bulk density is 1.65 g/cm^3 [Heiken et al., 1991]. The approximate location of the sampling of this core is shown with a red arrow in Fig. 4.7. The history of this core seems to be a little more complicated than the others, a summary follows.

Fruchter et al. [1982] measured a ^{26}Al depth profile in this core, obtaining a reasonably good agreement with the calculated profile [Reedy and Arnold, 1972], but showing a possible depletion of activity in the upper 9 g/cm^2. Nishiizumi et al. [1990] measured

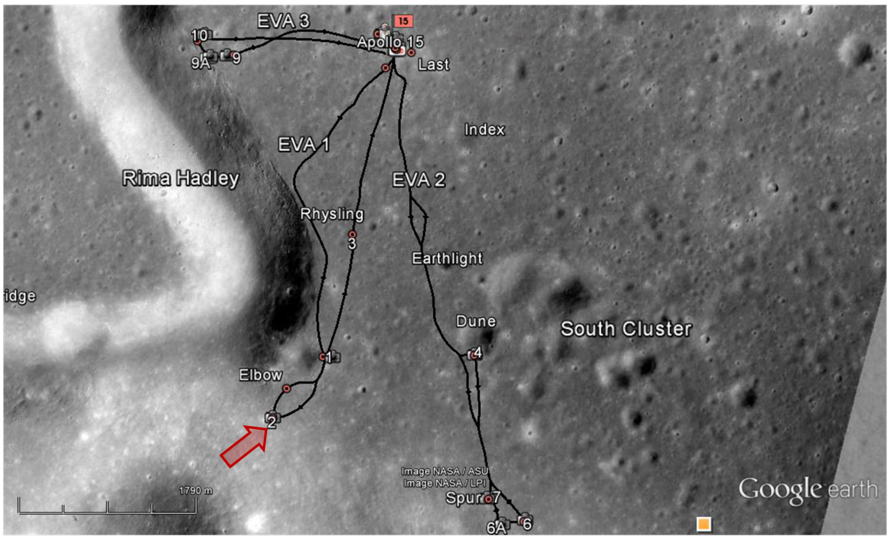

Figure 4.7. Map of the landing site of Apollo 15 including the extravehicular activities (EVAs). The red arrow indicates the approximate sampling location of the core 15008. Image taken from Google Earth V:7.1.1.1888.

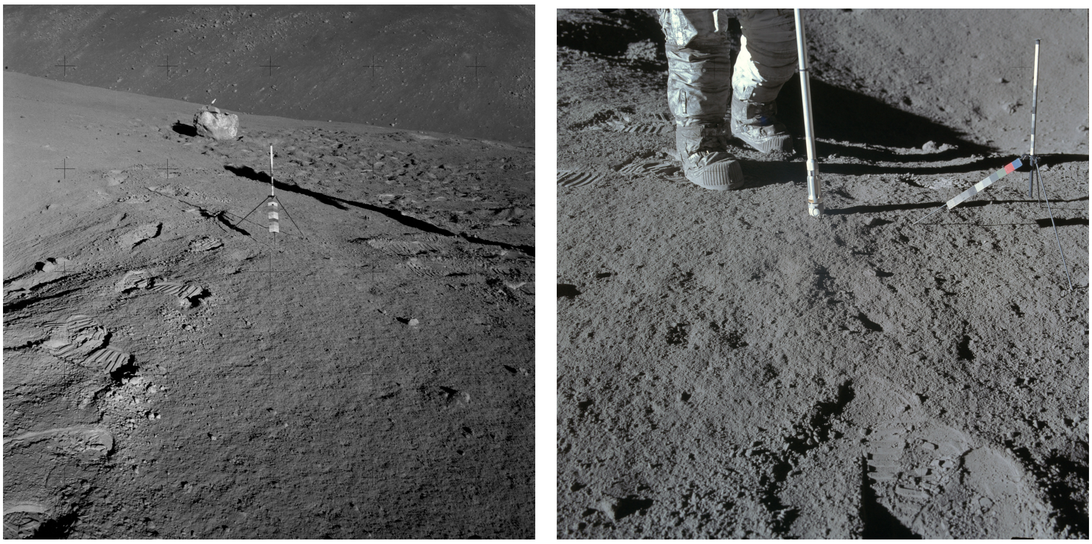

(a) (b)

Figure 4.8. Collection of the core 15008: (a) The core was taken near a small crater (diameter between 5 and 10 m); (b) detail images of astronaut James Irwin, with the core completely driven into the rim of the crater The gnomon, visible in both pictures, was placed near sampling positions as a reference (AS15-85-11443 and AS15-86-11578).

a ^{53}Mn depth profile, but in this case, the depth profiles seems clearly undersaturated, increasingly towards the surface [see both profiles in Nishiizumi et al., 1990, Fig.1]. They model this results with the idea that more than 5 g/cm^2 of the surface was removed perhaps 5×10^6 years ago, and that infilling of material at about the GCR-saturated activity level continued until $\sim$ 1.5-2×10^6 years ago, with little alteration since.

Nagle [1980] carefully studied the petrography (detailed description of rocks) of several cores, one of them being 15008. He found that the upper 17.5 cm of this core were light-colored, coarse grained soil, with chaotic structure (fabric) and abundant bedrock-derived rock fragments. Then follows a zone of dark, fine-grained soil, with horizontal fabric and abundant regolith-derived rock fragments. His hypothesis is that light soils are rim crest deposits and the dark soils are older regolith. The contrast in texture, fabric and structure, and composition between the light and dark soils in this core are best explained if the coarse-grained, poorly sorted, chaotic, marbled, bedrock-rich light-colored soils are rim crest ejecta; and the finer, better-sorted, glass- and soil breccia-rich dark soils, with *in-situ* glass that must have formed at the lunar surface, are pre-existing regolith. A cartoon depicting the possible scenario of this core is shown in Fig. 4.9.

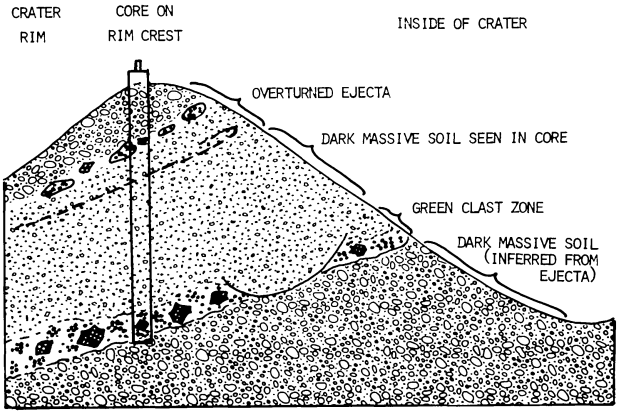

Figure 4.9. Cartoon depicting soil-cross-section that was sampled by 15008/7. Below this core is a sequence of crater bottom structures, seen now only in highest ejecta. The continuous green clast ejecta zone is reworked, penetrated by craters in some areas, is overlain by a thick crater bottom sequence, all of which is overturned in the upper ejecta. As shown in Nagle [1980].

4.1.3 Apollo 16 samples

The Apollo 16 mission was the first to land on the Lunar Highlands (9.0° S, 15.5° E), on April 21th, 1972. The missions before this one landed in the Lunar *maria*. It was believed that the Highland region was of volcanic origin. This was later proved as incorrect, as scientists began to study the samples returned to Earth. The astronauts returned a total of 95.8 kg of lunar samples in this mission.

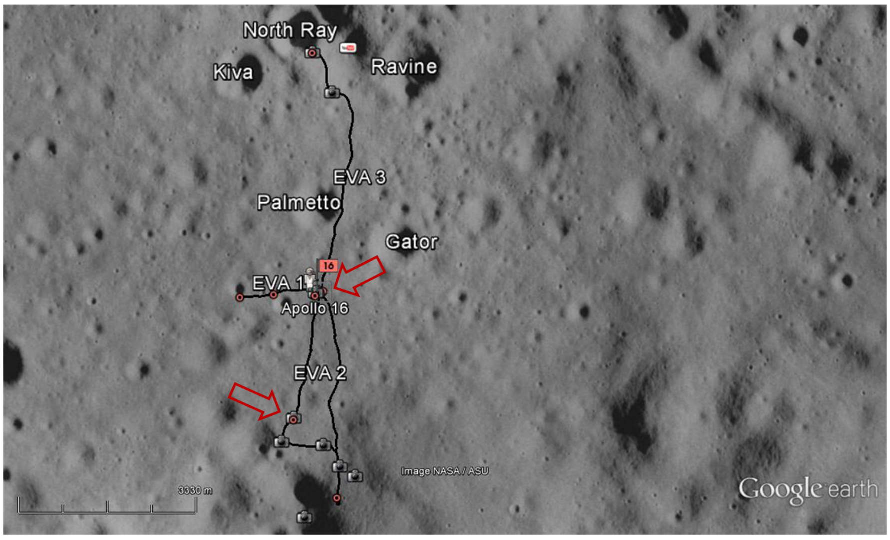

Figure 4.10. Map of the landing site of Apollo 16 including the extravehicular activities (EVAs). The red arrows indicate the approximate sampling location of the different sample sets. Image taken from Google Earth V:7.1.1.1888.

For this work, two sets of samples were chosen. The approximate sampling location can be seen in Fig. 4.10. We received five samples from the 60007 and 60006 portions of the deep drill string 60007-60001, which has a total depth of about 225 cm. The soil in the area where this drill core was obtained was loose, possibly because of numerous small crates in the vicinity, making the drilling of the core an easy task. To remove it, a treadle was used (similar to a car jack). Unfortunately, there are no detailed pictures of the process, only video footage, which can be seen on the web page of the Apollo Lunar Surface Journal [ALSJ, 2013]. The bulk density of this core is 1.50 g/cm^3 [Heiken et al., 1991]. The measured samples range from depths of 3 to 32 cm.

Additionally, we received a skim (69921), scoop (69941) and *under-boulder* (69961) samples. The first two samples were collected from the shade cast by a small boulder (~0.5 m). After carefully skimming the lunar surface with a scoop, penetrating approximately 5 mm, a regular scoop sample was taken from underneath, with an estimated penetration depth of 3 cm (Fig. 4.11(a)). After this, the boulder was turned over and the last sample was taken, as shown in Fig. 4.11(b). The goal was to sample pristine soil, not contaminated by the astronauts' steps or by the exhaust of the lunar module or the lunar roving vehicle, used to arrive to the station 9 where these samples were gathered. Information about the bulk density of these samples is missing, thus a representative value of 1.5 g/cm^3 was assumed.

(a) (b)

Figure 4.11. (a) Sampling of the skim and scoop samples, from the shadow of a 0.5 m boulder. (b) The boulder was then tipped over and a sample was taken from the regolith underneath it (AS16-107-17561 and AS16-107-17577).

The measurements of the ^{26}Al and ^{53}Mn depth profiles from the 60007/6 core were first published by Imamura et al. [1974] and Nishiizumi et al. [1976]. The ^{26}Al profile can be seen in Fig. 4.12. As the profile is undersaturated towards the surface, it indicates a mixing on the order of few centimeter over a period of 10^6 years. Nevertheless, Evans et al. calculated an ^{26}Al excess of 17% when integrated over the range of 0-16 g/cm^2. The ^{53}Mn depth profile, displayed in Fig. 4.13, shows an excess of 35 % [Evans et al., 1980] compared to the calculated profile, integrated over the same depth range. This is best explained with a continuous deposition of highly irradiated material at a rate of 2 cm/Myr coming from impacts ocurring in the vicinity and/or down slope movement of regolith. Both estimations were compared with the model by Reedy and Arnold [1972].

One important variable in the analysis of the set of skim, scoop and under-boulder

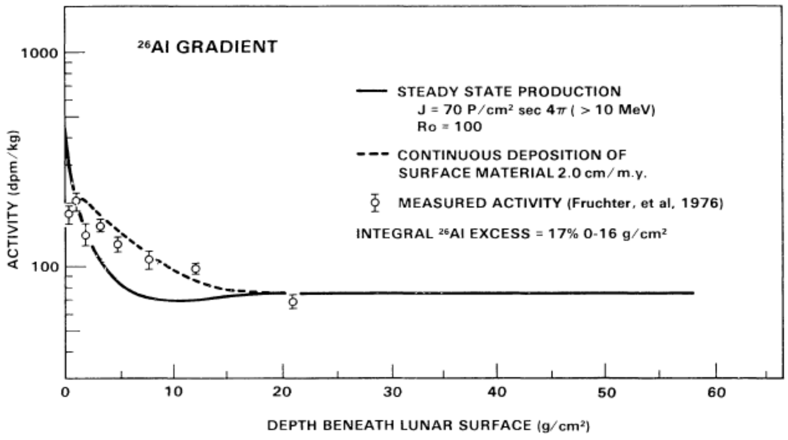

Figure 4.12. ^{26}Al depth profile measured in the Apollo 16 deep drill core 60007, compared with the calculated profile. As shown in Evans et al. [1980].

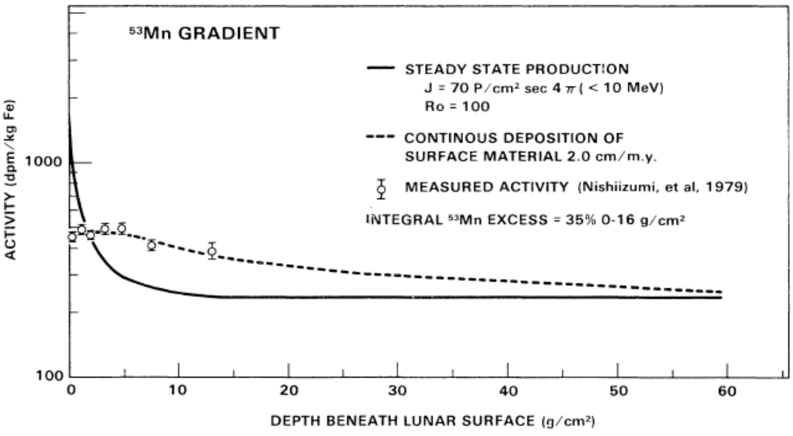

Figure 4.13. ^{53}Mn depth profile measured in the Apollo 16 deep drill core 60007, compared with the calculated profile. As shown in Evans et al. [1980]

samples is the exposure age of the boulder. Several studies have been made on samples 69935 and 69955, two fragments chipped off of the 0.5 m rock from the top and the bottom, respectively. Behrmann et al. [1973] and Drozd et al. [1974] measured the isotopic ratios of ^{81}Kr/Kr and other krypton isotopic abundances in both samples. Noble gases found inside this samples are of solar origin and are partially produced in-situ in spallation reactions. Since ^{81}Kr has a half life of 2.3×10^5 yr, the interpretation of long exposure ages is uncertain [Drozd et al., 1974]. Thus, this boulder was first wrongly associated with the South Ray crater, which is a fresh crater, probably 2 Myr old. They also inferred different, incompatible ages, which could only be explained with a complicated and improbable exposure history. Besides, the possibility of erosion was not taken into account in both publications.

Fruchter et al. [1981] measured the ^{26}Al and ^{53}Mn concentrations of both fragments, as well as the adjacent skim and under-boulder samples (69921 and 69961). Their results showed a low concentration in the 69935 sample (top of the boulder) and a high concentration (one of the highest measured on lunar samples) in the adjacent 69921 soil sample. Their proposed explanation is that this was caused by the milling of the rock by micrometeorites (as schematically shown in Fig. 4.14), that caused the deposition of highly irradiated material from the top of the rock to the adjacent soil. Concerning the age, they compared the results obtained in samples 69955 and 69961, namely the bottom fragment of the rock and the regolith underneath it. Both measurements gave similar results and the inferred exposure age of (5.0±0.8) Myr.

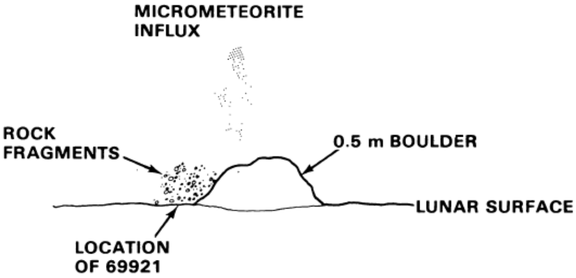

Figure 4.14. Proposed micrometeorite erosion model for high ^{26}Al and ^{53}Mn contents in shadowed soil 69921. As shown in Fruchter et al. [1981].

4.2 Elemental composition of the lunar samples

The elemental composition of the lunar samples was determined by ICP-MS. The results are presented in Table 4.1. In general, the agreement with previous measurements [Meyer et al., 1971; Warren et al., 1983; Korotev, 1981] is good, except for samples 69941 and 69961, for which our results are lower by about 40% for unknown reasons.

Sample	Mg wt%	Al wt%	Ca wt%	Ti wt%	Fe wt%	Ni ppm
12025,14,365	5.4 ± 0.1	6.42 ± 0.08	7.0 ± 0.2	1.55 ± 0.01	12.6 ± 0.2	128 ± 2
12025,23,366	5.7 ± 0.1	6.45 ± 0.09	7.2 ± 0.2	1.57 ± 0.02	12.5 ± 0.2	145 ± 3
15008,1050	5.9 ± 0.1	9.7 ± 0.2	8.8 ± 0.3	0.77 ± 0.01	9.4 ± 0.2	154 ± 3
15008,1051	5.6 ± 0.1	8.9 ± 0.1	8.7 ± 0.4	0.75 ± 0.01	8.6 ± 0.1	145 ± 3
15008,1052	5.5 ± 0.1	8.9 ± 0.1	8.0 ± 0.3	0.71 ± 0.01	8.3 ± 0.1	159 ± 2
15008,1053	6.2 ± 0.1	9.5 ± 0.1	8.6 ± 0.3	0.77 ± 0.01	9.2 ± 0.1	213 ± 3
69921,31,0	3.50 ± 0.08	13.2 ± 0.2	11.5 ± 0.4	0.37 ± 0.01	4.82 ± 0.08	1211 ± 17
69941,138,42	2.28 ± 0.05	8.2 ± 0.1	8.1 ± 0.2	0.23 ± 0.01	2.84 ± 0.05	299 ± 5
69961,143,38	2.37 ± 0.05	8.8 ± 0.1	8.4 ± 0.3	0.23 ± 0.01	2.91 ± 0.05	266 ± 3

Table 4.1. Elemental composition of the Moon samples, measured via ICP-MS. The nickel values are blank-corrected. The uncertainties correspond to 1σ.

4.3 ^{10}Be and ^{26}Al in lunar samples

The measurements of the ^{26}Al/Al and ^{10}Be/Be ratios were available from PRIMELab, an AMS facility at Purdue University, United States of America, better suited for lighter AMS isotopes. The results are shown in Table 4.2. The ^{26}Al profiles of cores 12025 and 15008, compared with previous measurements are shown in Fig. 4.15.

As was already explained in Sec. 4.1, core samples having the same specific identificatory number are essentially the same sample, as they correspond to the same depth. This is valid for samples 12025,14,365 and 358, and for 12025,23,366 and 359. The ^{10}Be results are, for these 2 samples, about 40% lower than the ones reported by Cook et al. [2009]. No other values for the other studied samples were found. Good agreement was found between the new measurements of ^{26}Al and the previous publications [Rancitelli et al., 1971; Fruchter et al., 1982; Cook et al., 2009].

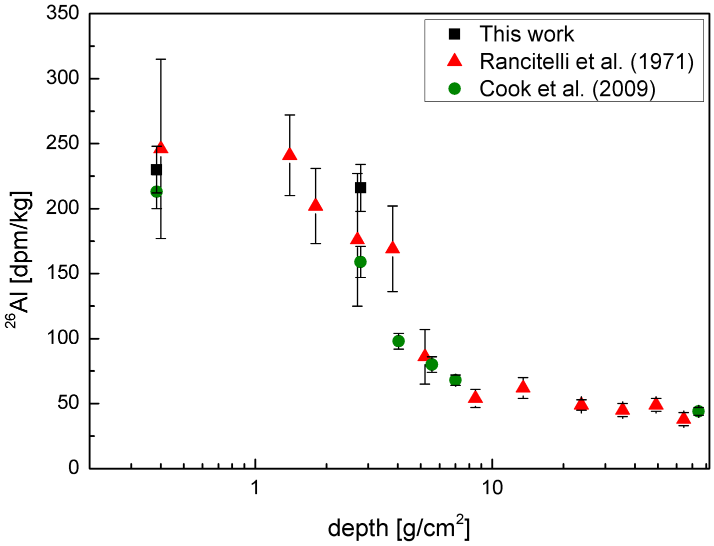

(a)

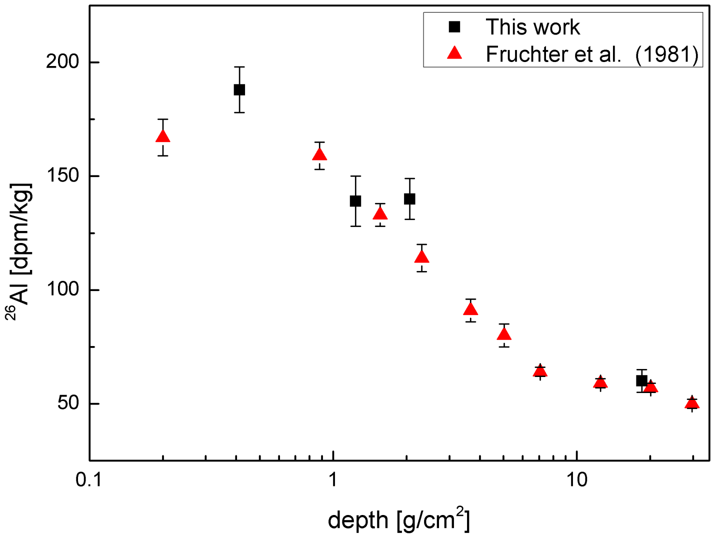

(b)

Figure 4.15. ^{26}Al measurements of cores (a) 12025/8 and (b) 15008, compared with previous measurements [Rancitelli et al., 1971; Cook et al., 2009; Fruchter et al., 1981].

Sample	Depth [cm]	^{26}Al [dpm/kg]	^{10}Be [dpm/kg]
12025,14,365	0.2 ± 0.2	230 ± 18	9.32 ± 0.37
12025,23,366	0.8 ± 0.4	216 ± 18	9.78 ± 0.31
12025,14,358(*)	0.2 ± 0.2	213 ± 13	13.4 ± 0.7
12025,23,359(*)	0.8 ± 0.4		12.9 ± 0.7
12025,30,360(*)	1.45 ± 0.25	159 ± 12	13.9 ± 0.8
12025,11,357(*)	2.1 ± 0.4	98 ± 6	12.8 ± 0.6
12025,10,356(*)	2.9 ± 0.4	80 ± 6	14.1 ± 0.8
12025,9,355(*)	3.65 ± 0.35	68 ± 4	13.1 ± 0.7
12028,493,837(*)	38.7 ± 0.5	44 ± 3	11.7 ± 0.7
15008,1004,1050	0.25 ± 0.25	188 ± 10	8.79 ± 0.26
15008,1005,1051	0.75 ± 0.25	139 ± 11	8.56 ± 0.23
15008,1006,1052	1.25 ± 0.25	140 ± 9	9.29 ± 0.24
15008,1026,1053	11.25 ± 0.25	60 ± 5	9.75 ± 0.27
60007,99,517(*)	3.25 ± 0.25	133 ± 7	13.3 ± 0.4
60007,15,516(*)	7.25 ± 0.25	112 ± 7	13.7 ± 0.7
60007,36,515(*)	13.25 ± 0.25	68 ± 5	16.0 ± 1.0
60007,62,514(*)	18.25 ± 0.25	72 ± 5	13.0 ± 1.1
60006,78,418(*)	31.75 ± 0.25	66 ± 4	13.9 ± 0.8
69921,31,0	0.25 ± 0.25	244 ± 21	9.32 ± 0.32
69941,138,42	1.75 ± 1.25	123 ± 8	8.79 ± 0.71
69961,143,38	under boulder	67 ± 6	10.79 ± 0.21

Table 4.2. ^{10}Be and ^{26}Al activities of the samples, measured meanings AMS at PRIME-Lab. The samples marked with a (*) are from Cook et al. [2009]. The uncertainties correspond to 1σ.

4.4 Meteorite samples

Iron meteorites are very rich in nickel and iron, the principal target elements for spallogenic production of ^{60}Fe and ^{53}Mn, respectively. The concentration of these radioisotopes (and respective activity) can be used to establish reference levels for the production of ^{60}Fe and ^{53}Mn in the lunar surface due to galactic cosmic rays.

A total of 7 different samples, from a set of 4 iron meteorites, were analyzed during the course of this work. Additionally, a thorough search through publications was performed, in order to find other results for nickel rich meteorites. A total of 13 was found [Knie et al., 1999b; Berger et al., 2007; Nishiizumi and Honda, 2007]. Four of them, the ones published by Nishiizumi and Honda [2007], were measured via low-level counting of ^{60}Co ($T_{1/2}$=5.27 yr)[*] by dissolving masses between 0.5 and 2.5 kg of meteorite per sample. The other measurements were performed via AMS at the facility in Garching, needing sample weights of only a few milligrams. This example shows a very important advantage of AMS over decay counting techniques.

Table 4.3 shows the results of both sample groups, along with the references of the previous publications and the concentration of the major elements in the samples.

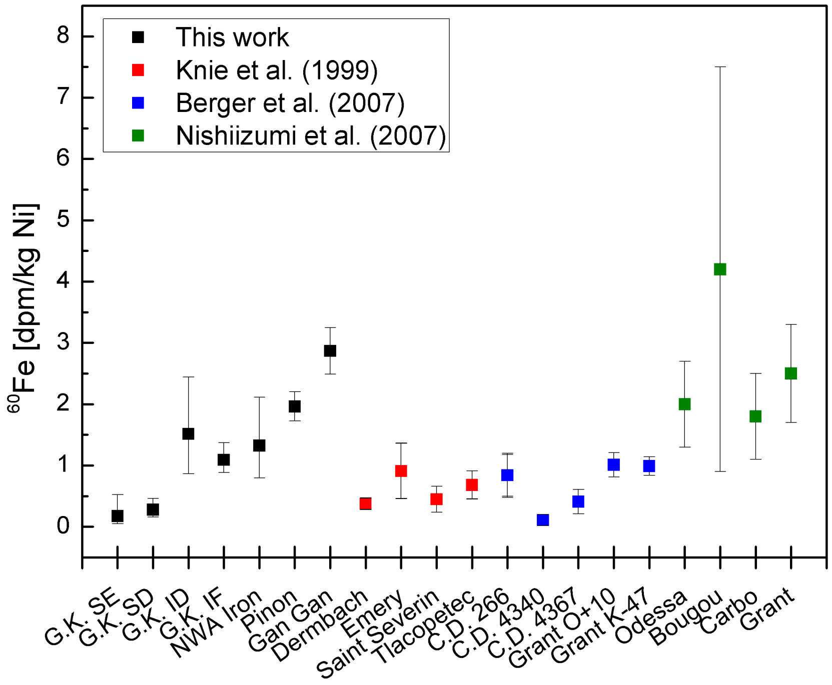

Figure 4.16. Summary of ^{60}Fe activities in iron meteorites found in the literature [Nishiizumi and Honda, 2007; Knie et al., 1999b; Berger et al., 2007] and the ones determined during the course of this work. C.D. stands for Canyon Diablo and G.K. for Gebel Kamil.

---

[*] The radioisotope ^{60}Fe decays to ^{60}Co and then finally to the stable ^{60}Ni.

Sample	Fe	Ni	^{60}Fe	^{53}Mn	Reference
	wt%	wt%	dpm/kg Ni	dpm/kg Fe	
Dermbach	51.8	47.0	$0.38^{+0.10}_{-0.09}$	165±18	Knie et al. [1999b]
Tlacopetec	81.5	18.0	$0.68^{+0.23}_{-0.17}$		
Emery (m.f.)	89.3	7.8	$0.91^{+0.45}_{-0.34}$	371^*	
Saint Séverin (m.f.)	47.6	13.2	$0.44^{+0.21}_{-0.16}$		
Odessa	n.r.	7.25	2.0±0.7		Nishiizumi and Honda [2007]
Bougou		7.15	4.2±3.3		
Carbo		10.02	1.8±0.7		
Grant		9.24	2.5±0.8		
Canyon Diablo 266	n.r.	6.91	0.48±0.20		Berger et al. [2007]
Canyon Diablo 4340		6.98	0.06±0.05		
Canyon Diablo 4367		6.98	0.23±0.11		
Grant O+10		9.29	0.57±0.11		
Grant K-47		9.29	0.69±0.14		
Dorofeevka		11.3	0.56±0.09		
NWA Iron	86.0	6.0	$1.3^{+0.4}_{-0.3}$	596±33	This work
Gebel Kamil Se	78.4	20.0	0.18±0.09	117±6	
Gebel Kamil Sd	77.4	19.3	0.28±0.11	116±7	
Gebel Kamil Id	77.7	19.0	1.52±0.21	399±18	
Gebel Kamil If	79.3	18.0	1.09±0.22	348±15	
Piñon	86.8	16.6	0.97±0.20		
Gan-Gan	94.1	9.5	2.1±0.3		

Table 4.3. Previous measurements of ^{60}Fe in iron meteorites. Emery and Saint Séverin are stony irons, m.f. stands for magnetic fraction. Neither Nishiizumi and Honda [2007] or Berger et al. [2007] reported the Fe concentration of their samples (n.r. stands for not reported). The value of the Mn activity for Emery (marked with a *) was obtained from Merchel [2012]. The values from Berger et al. [2007] and Knie et al. [1999b] shown in this table are corrected using the newly measured half life of ^{60}Fe [Rugel et al., 2009]. The uncertainties correspond to 1σ (confidence interval of 68%). No better information for the iron and nickel contents for the Piñon and Gan-Gan meteorites is available.

Chapter 5

Results

Contents

A total of 24 different samples from 3 different Apollo missions were measured in this work. The results for ^{10}Be and ^{26}Al have been already discussed in chapter 4, ^{53}Mn and ^{60}Fe are shown in this chapter. Of the total samples, 11 from the Apollo 12 12025 core and 5 from the Apollo 16 60007/6 core were partially analyzed and published by Cook et al. [2009]. These will also be considered here. A more complete interpretation will be attempted after the presentation of the whole set of results. For a summary of all relevant results, the reader is referred to the Appendix C.

Some results were already shown in previous chapters in order to emphasize arguments or compare with preceding measurements. At this point it is important to clarify the difference of the units used in this work. As a result of an AMS measurements, one obtains an isotopic ratio, for example, ^{60}Fe/Fe. By using the half live of the radioisotope and knowing the elemental composition of the sample, one can calculate the activity in disintegrations per minute and kg of some interesting element: for example dpm/kg Ni in the case of ^{60}Fe, since nickel is the principal target material for the spallation production of this isotope. This unit is used widely in the publications relevant to this work. For this reason both units will be used during this chapter. For the transformation between isotopic ratios and activities the half lives of ^{53}Mn and ^{60}Fe used are 3.7 Myr [Honda and Imamura, 1971] and 2.62 Myr [Rugel et al., 2009], respectively. The errors given include the 1 σ uncertainties of the AMS measurement, while the systematic error of the half lives of ^{53}Mn and ^{60}Fe are omitted.

5.1 ^{53}Mn

^{53}Mn can be measured via neutron activation analysis (NAA), but this technique requires a lot of effort and expenditure [see for example Imamura et al., 1979, where the measuring procedure is explained], besides being less sensitive than AMS. All other results presented here, besides our own, were measured with this technique.

For our measurements, the blank level for ^{53}Mn was 1×10^{-13}. This sensitivity can be improved by 2 orders of magnitude [Poutivtsev et al., 2010], but this was not necessary in this work, because the concentrations in our samples were on average 2 orders of magnitude higher.

5.1.1 Apollo 12 core 12025

The results of the AMS measurement of the ^{53}Mn/Mn depth profile of the Apollo 12 12025 core are shown in Fig. 5.1(a). Fig. 5.1(b) shows the same profile, but with the calculated activity normalized to the iron content of the samples and compared with the results published by Nishiizumi et al. [1979]. The depth is noted in g/cm^2, calculated by dividing the mean depth of the sample by the bulk density of the core, in this case 1.92 g/cm^3 [Heiken et al., 1991].

Except for two data points (1.5 and 12.5 g/cm^2), both profiles agree with each other. These can be described as smoothly decreasing as the depth in the core increases to more than 1 g/cm^2. The ^{53}Mn activity in the uppermost section of the core seems more constant. The small discrepancies between the two graphs of Fig. 5.1(b) can be explained by the differences in the composition measured during this work and by Nishiizumi et al., but do not significantly influence the interpretation of the results. This profile corresponds to a slightly disturbed core, with a rapid decrease in the activity from a depth from approximately 2 g/cm^2 to 16 g/cm^2. Nishiizumi et al. [1979] notice a slight increase in the activity, followed by a small decrease. In other words, they found a maximum activity at this depth. They assumed this fact could be explained with the addition of 2 g/cm^2 of material to an undisturbed core. Comparing their results with the model of Reedy and Arnold [1972], they found an excess in the depth integrated activity, up to a depth of 10 g/cm^2, that is 1.2 ± 0.1 larger than the theoretical prediction.

5.1.2 Apollo 15 core 15008

The AMS measurements of the Apollo 15 15008 core are shown in Fig. 5.2(a). The same results are shown in Fig. 5.2(b), but in dpm/kg Fe units, compared with earlier

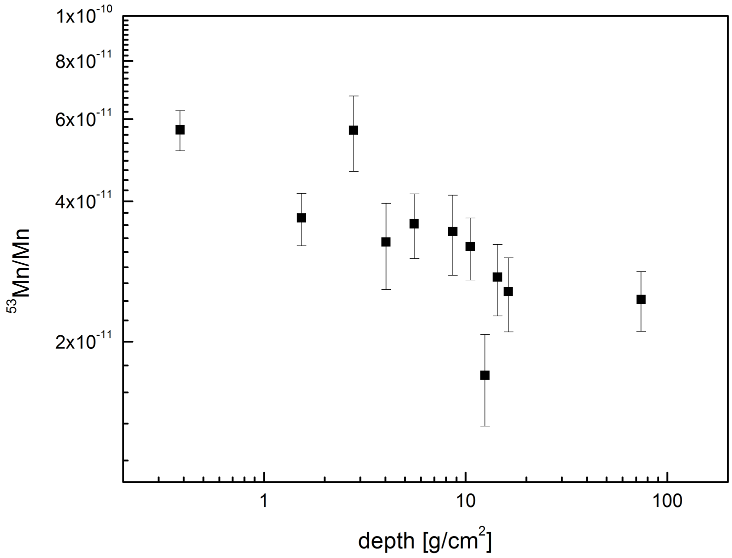

(a)

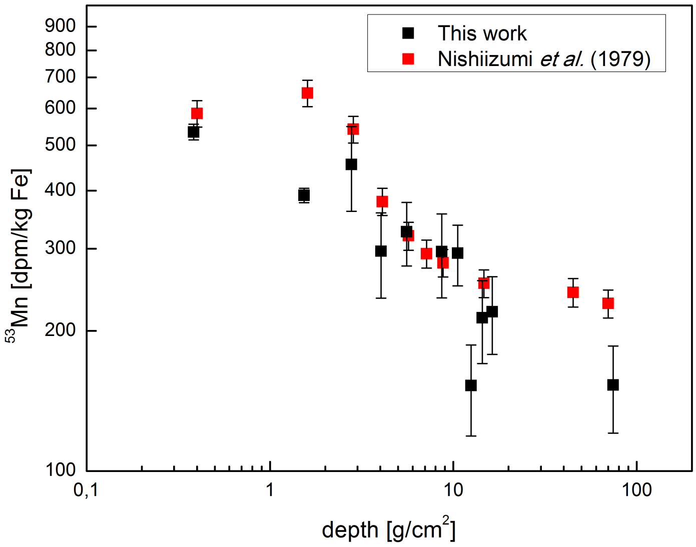

(b)

Figure 5.1. Results of the measurements of the ^{53}Mn depth profile of the Apollo 12 core 12025. (a) AMS results. (b) Same as in (a) but with the calculated activity, as a direct comparison with the published results of Nishiizumi et al. [1979]. Error bars correspond to a 1σ uncertainty.

measurements via NAA by Nishiizumi et al. [1990]. Our data points match with the existing measurements within 1 σ uncertainty, completing the profile with new values in previously missing depths, except for the sample of 1.1 g/cm^2 depth, which is lower and does not fit with the expected curve. This difference may lie in a slightly different iron concentration of the specific sample. This is supported by the fact that the ^{53}Mn/Mn profile from Fig. 5.2(a) does not show any disruptions. The depths are expressed in g/cm^2, calculated with the bulk density of the core, 1.65 g/cm^3 [Heiken et al., 1991].

As it was already discussed in chapter 4, this core seems to have a rather complicated history. Its depth profile is undersaturated and shows no significant gradient near the surface, as it is expected for an undisturbed core. This core was taken from the rim of a crater. Nishiizumi et al. [1990] proposed a simple model that could explain this result, evaluating the possibility that material from the surface down to a depth of approximately 5 g/cm^2 was removed 5×10^6 years ago, and that infilling from material with about GCR saturated activity continued until $1.5 - 2 \times 10^6$ years ago. This is supported by the petrography study by Nagle [1980], who noticed that the upper 17.5 cm (28.9 g/cm^2) of the core was of a lighter color, coarse grained, than the soil directly below, which is darker and contains finer grains. He assumed this to be deposited from rim crest ejecta.

5.1.3 Apollo 16 60007/6 core

Fig. 5.3(a) show the results for the Apollo 16 60007/6 drill core. The bulk density of this core is 1.5 g/cm^3 [Heiken et al., 1991] and this was used to express the depth units of g/cm^2. The comparison with previous measurements [Imamura et al., 1974; Nishiizumi et al., 1976] in dpm/kg Fe is shown in Fig. 5.3(b). We complemented with data points at depths that have not been measured yet.

The depth profile shown in Fig. 5.3(b) is not as smooth as the previous one. It is flat down to a depth of 4 g/cm^2 (2.7 cm) and then decreases rapidly. When compared with the expected activity calculated with the Reedy and Arnold [1972] model, the measured profile shows an excess of 35% , integrated over the 0-16 g/cm^2 depth range [Nishiizumi et al., 1976].

5.1.4 Apollo 16 shaded samples

This set of samples cannot be described in the same way as the core samples mentioned before. Their depths are only approximately known, as the objective of their

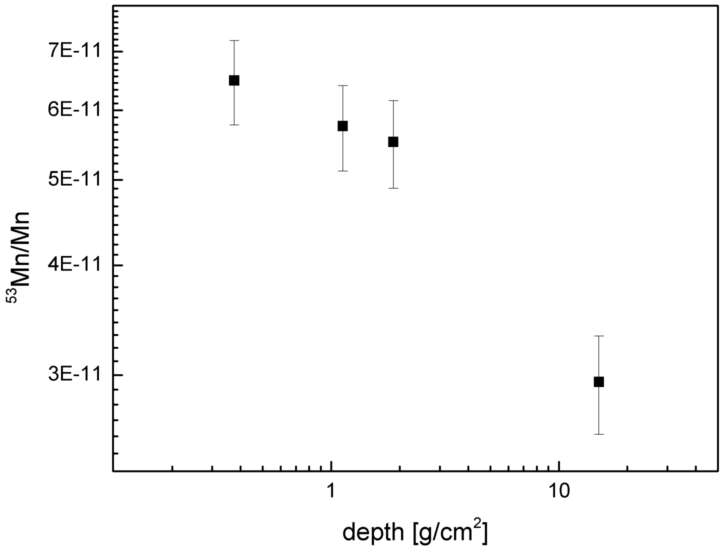

(a)

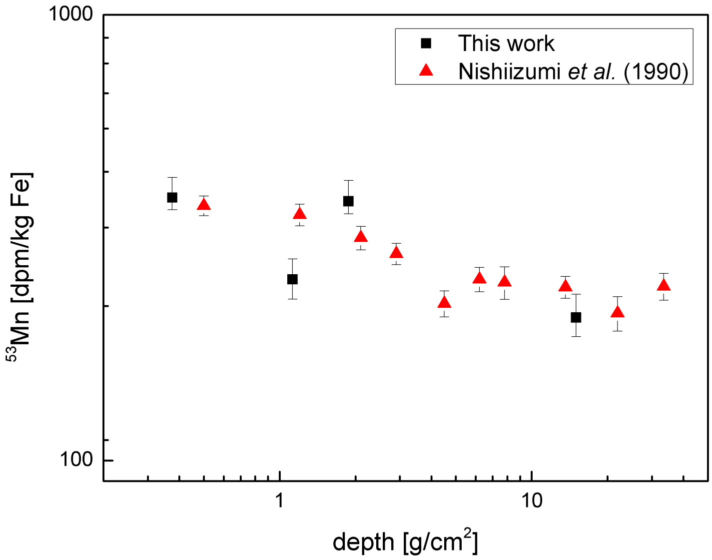

(b)

Figure 5.2. Results of the measurements of the ^{53}Mn depth profile of the Apollo 15 core 15008. (a) AMS results. (b) Same as in (a) but with the calculated activity, as a direct comparison with the published results of Nishiizumi et al. [1990]. Error bars correspond to a 1σ uncertainty.

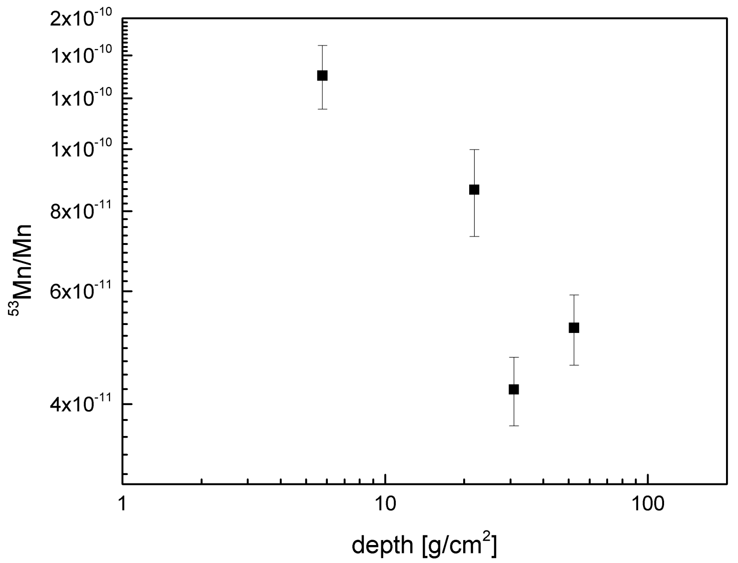

(a)

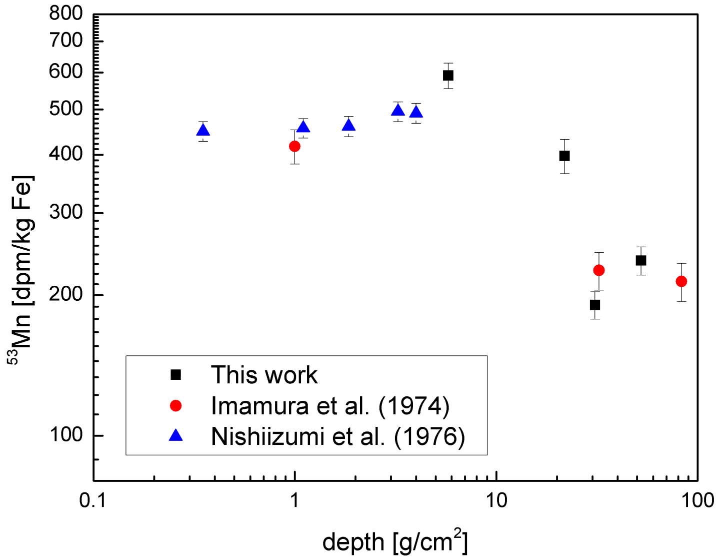

(b)

Figure 5.3. Results of the measurements of the ^{53}Mn depth profile of the Apollo 16 core 60007/6. (a) AMS results. (b) Same as in (a) but with the calculated activity, as a direct comparison with the published results of Imamura et al. [1974] and Nishiizumi et al. [1976]. Error bars correspond to a 1σ uncertainty.

sampling was to obtain pristine samples, not contaminated by the exhaust of the lunar module or disturbed by the steps of the astronauts as they approached the sampling location. Samples 69921 and 69941 were collected from the shade cast by a small boulder, first skimming the surface with a scoop, taking approximately 0.5 cm of regolith, then a regular scoop was taken from the same location, up to a depth of approximately 3 cm. The boulder was then tipped over and the sample 69961 was taken from underneath it (see Fig. 4.11).

Sample	Depth [cm]	^{53}Mn/Mn [10^{-11}]	^{53}Mn [dpm/kg Fe] This work	^{53}Mn [dpm/kg Fe] Fruchter et al. [1981]
69921,31,0	~ 0.5	8 ± 1	653 ± 88	630 ± 65
69941,138,42	~ 3	5.0 ± 0.6	313 ± 38	
69961,143,38	under boulder	4.5 ± 0.5	223 ± 51	245 ± 27
69935	top of boulder			135 ± 15
69955	bottom of boulder			148 ± 20

Table 5.1. Results of the measurements of the ^{53}Mn of the set of shaded samples. Results are expressed as isotopic ratio, as measured by means of AMS, and in dpm/kg Fe, for the comparison with previous measurements via NAA [Fruchter et al., 1981]. Error bars correspond to a 1σ uncertainty.

The results for this set of samples are shown in Table 5.1, along with selected results from Fruchter et al. [1981], including two shaded samples. Our results compare well with the previous ones, taking into account the uncertainties. Fruchter et al. measured samples 69921 and 69961, as well as samples taken from the top and from the bottom of the boulder, 69935 and 69955, respectively, in order to determine the exposure age of the rock. Results of both samples yielded different exposure ages, but comparison with 69961 yielded an age of (5.0 ± 0.8) Myr. In contrast, if they would have taken the activity of sample 69935 into account, the exposure age would be approximately 2 Myr. As the authors emphasize, the ^{53}Mn activity of sample 69921 is one of the highest activities measured on the lunar surface. They proposed that eroded, saturated material from the top of the boulder, fell onto the surface of the regolith, explaining the high activity of sample 69921 and the undersaturated activity of the sample taken from the top of the boulder.

5.2 ^{60}Fe

There is one previous publication that reported ^{60}Fe/Fe concentrations in Moon samples, namely Cook et al. [2009]. These measurements were also performed in the AMS facility of the Maier-Leibnitz-Laboratorium during the year 2005. They measured a ^{60}Fe/Fe depth profile with 12 samples from the Apollo 12 12025 core and 5 samples from the Apollo 16 60007 drill core. A detailed description of the ^{60}Fe results of this work follows, considering the previous results by Cook et al. as well.

5.2.1 Previous measurements

Cook et al. [2009] measured a depth profile with 12 samples of the Apollo 12 12025 drive tube, with depths ranging from 0.2 cm through 38.7 cm. These measurements yielded only upper limits (no ^{60}Fe events) for every sample except for the surface sample, where 4 events were detected, corresponding to a ratio of ^{60}Fe/Fe of $3.6^{+2.5}_{-1.5} \times 10^{-15}$. Results were also obtained for 5 samples of the Apollo 16 drill core, with depths ranging from 3 to 32 cm. All samples showed between 3 and 7 counts, corresponding to concentrations of ^{60}Fe/Fe between 4×10^{-16} and 4×10^{-15}. These results are summarized in Table 5.2.

Cook et al. argued that the activity in the samples of the 60007/6 core were compatible with GCR origin within a 95% confidence level and that the activity measured in the surface sample of the 12025 core exceeded the predicted by SCR and GCR production on the lunar surface by more than 2 σ, hinting to the deposition of interstellar material.

5.2.2 New measurements

We requested two samples from the same Apollo 12 core, in order to confirm these findings. For this work, we measured samples 12025,14,365 and 12025,23,366, with depths of (0.2 ± 0.2) cm and (0.8 ± 0.4) cm, respectively. These are from the same depth as the 2 first samples from Cook et al. [2009]. The new result obtained for the surface sample agrees with the previous one and for the other sample, the measured concentration is within the upper limit reported in the mentioned publication. Since these are samples coming from the same core and from the same depths intervals (they have the same parent number, but different specific numbers), we regard them as the same samples. Fig. 5.4 show the depth profile from core 12025, where we included also the previous results.

Sample	Depth [cm]	Events	^{60}Fe/Fe [10^{-15}]	^{60}Fe [dpm/kg Ni]
12025,14,358	0.2 ± 0.2	4	$3.6^{+2.5}_{-1.5}$	14^{+10}_{-6}
12025,23,359	0.8 ± 0.4	0	< 10	< 22
12025,30,360	1.45 ± 0.25	0	< 8	< 17
12025,11,357	2.1 ± 0.4	0	< 2	< 4
12025,10,356	2.9 ± 0.4	0	< 6	< 13
12025,9,355	3.65 ± 0.35	0	< 3	< 7
12025,8,354	4.5 ± 0.5	0	< 2	< 4
12025,41,361	5.5 ± 0.5	0	< 20	< 43
12025,50,362	6.5 ± 0.6	0	< 4	< 7
12025,53,363	7.5 ± 0.5	0	< 11	< 24
12025,55,364	8.5 ± 0.5	0	< 6	< 13
12028,493,837	38.7 ± 0.5	0	< 3	< 7
60007,517,78	3.25 ± 0.25	7	$1.4^{+0.7}_{-0.5}$	$0.9^{+0.5}_{-0.3}$
60007,516,62	7.25 ± 0.25	3	$1.5^{+1.1}_{-0.9}$	$0.9^{+0.7}_{-0.6}$
60007,515,36	13.25 ± 0.25	4	$2.3^{+1.6}_{-1.0}$	$1.5^{+1.1}_{-0.6}$
60007,514,15	18.75 ± 0.25	5	$1.2^{+0.7}_{-0.6}$	$0.8^{+0.5}_{-0.3}$
60006,418,99	0.25 ± 0.25	5	$0.7^{+0.4}_{-0.3}$	$0.5^{+0.3}_{-0.2}$

Table 5.2. Summary of the ^{60}Fe results by Cook et al. [2009]. The table shows the results of the ^{60}Fe measurements. Confidence intervals correspond to 1 σ uncertainties.

As there was very little material from each position (from some samples as little as 1 mg of Fe_2O_3) each sample could be measured for only a limited period of time until the material was exhausted, thus no better sensitivity was achievable. Therefore, the concentrations measured in the first two samples are compatible with the upper limits from the deeper samples. By reducing the depth resolution and combining the results from the deeper samples in groups of 3 or 4, the upper limits can be improved, as can be seen in Fig. 5.4.

Table 5.3 shows all ^{60}Fe results from this work. The results for the samples of the Apollo 12 core include the first measurements performed on the same samples. The activities were calculated using the elemental compositions of the samples obtained from the ICP-MS measurements, shown in Table 4.1 in Chapter 4. Additionally, the expected

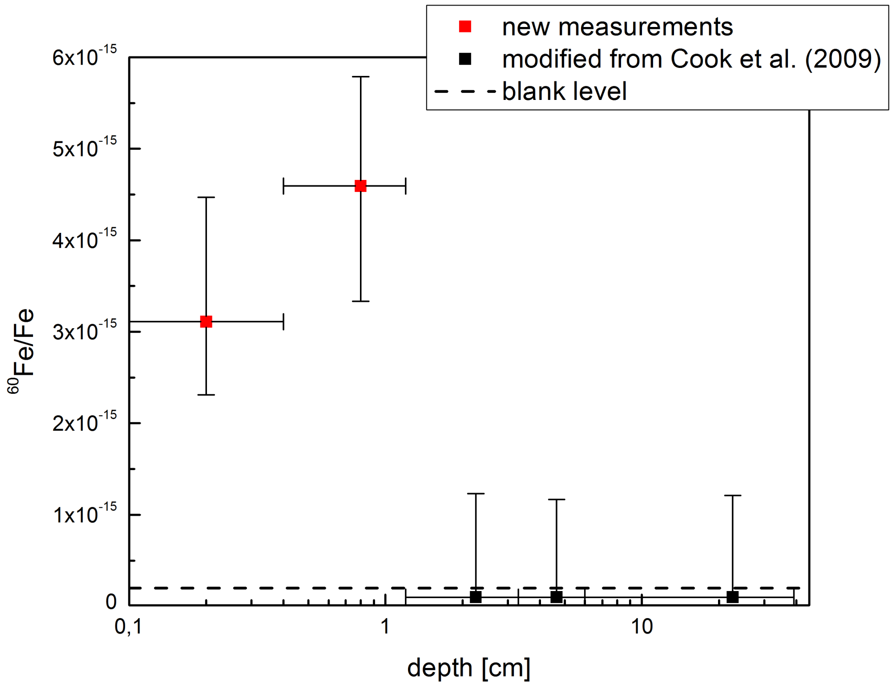

Figure 5.4. Results of the measurements of the ^{60}Fe/Fe depth profile of the Apollo 12 core 12025. The two upper samples (red in the graph) were analyzed by Cook et al. [2009] and during this work. The last three data points (black in the graph) are the deeper samples from the Apollo 12 12025 core, grouped 3 or 4 together (depth intervals are shown) in order to improve the upper limits of the previous measurement. Error bars in the x-direction correspond to depth intervals, in the y-direction to 1σ uncertainty.

background, assuming a blank concentration of ^{60}Fe/Fe $= 2\times10^{-16}$ during these experiments and the duration of each measurement, is shown in the same table, along with the number of events observed in each sample. The same results are also depicted in Figs. 5.5 and 5.6, isotopic ratios and activities, respectively. The depth of every sample is expressed in areal depth units, calculated with the respective bulk density of each core. For the shaded samples, approximate depths are given for the first two samples. Sample 69961 (under boulder) is included in the graphs with a depth of 70 g/cm^2. However, this value does not consider the shielding or depth from the lunar surface.

The new measurements yielded ^{60}Fe counts in every sample besides two of them: sample 15008,1052 (depth: (1.25 ± 0.25) cm) from the Apollo 15 15008 core and sample 69961 (under boulder). Some samples had only 2 or 3 counts, and some as many as 26.

Sample	Depth [cm]	Events	Expected background	^{60}Fe/Fe [10^{-15}]	^{60}Fe [dpm/kg Ni]
12025,14	0.2 ± 0.2	6	0.34	$3.1^{+1.9}_{-1.1}$	$16.6^{+7.2}_{-4.3}$
12025,23	0.8 ± 0.4	25	0.98	$4.6^{+1.2}_{-1.3}$	$21.4^{+5.6}_{-5.9}$
15008,1050,1004	0.25 ± 0.25	2	0.17	$2.3^{+2.6}_{-1.5}$	$7.6^{+8.7}_{-5.1}$
15008,1051,1005	0.75 ± 0.25	2	0.05	$7.8^{+8.8}_{-5.0}$	$25.3^{+20.7}_{-11.7}$
15008,1052,1006	1.25 ± 0.25	0	0.17	< 1.3	< 3.8
15008,1053,1026	11.25 ± 0.25	3	0.34	$1.6^{+1.3}_{-1.1}$	$3.7^{+2.9}_{-2.5}$
69921,31,0	0.25 ± 0.25	26	0.79	5.9 ± 1.8	1.3 ± 0.4
69941,138,42	1.75 ± 1.25	19	0.41	$4.2^{+1.6}_{-1.4}$	$4.2^{+2.6}_{-2.5}$
69961,38,146	under boulder	0	0.22	< 1.3	< 0.8

Table 5.3. Summary of the ^{60}Fe results. The table shows the results of the ^{60}Fe measurements. For the conversion between isotopic ratios and activities, the half life of ^{60}Fe of 2.62 Myr was used. Sample 12025,14 includes the 4 counts reported by Cook et al. [2009]. The expected background was estimated given the sensitivity of the set up and the duration of each measurement.

The possible origin of ^{60}Fe in the lunar samples will be discussed in the following.

In the work by Cook et al. [2009], the production due to SCR spallation was estimated with the help of the TALYS code [Koening et al., 2007]. It uses the cross sections for the $^{\mathrm{nat}}$Fe(α,X)^{60}Fe, $^{\mathrm{nat}}$Ni(p,X)^{60}Fe and $^{\mathrm{nat}}$Ni(α,X)^{60}Fe reactions, to calculate the production rate for ^{60}Fe on the lunar surface. The results for the *in-situ* production of ^{60}Fe show a maximum at the surface and decrease rapidly with depth. For the Apollo 12 12025 core, the expected SCR contribution in the lunar surface is 0.45 dpm/kg Ni, and for the Apollo 16 60007/6 core 0.07 dpm/kg Ni. Consequently, the contribution at depths greater than 1 g/cm^2 can be neglected. This production mechanism alone cannot account for the activity observed in the lunar samples.

The contribution to the local production of ^{60}Fe by GCR was estimated by taking into account the activities in iron meteorites. This type of meteorite is composed mainly of iron and nickel, which are the principal spallogenic targets for the production of both ^{53}Mn and ^{60}Fe. As mentioned in Chapter 4, a set of 7 different samples coming from 4 iron meteorites were analyzed with AMS. Additionally, all measurements of the ^{60}Fe activity of 11 iron meteorites have been included [Berger et al., 2007; Nishiizumi and Honda, 2007; Knie et al., 1999b]. These results are summarized in Table 4.3 in chapter 4

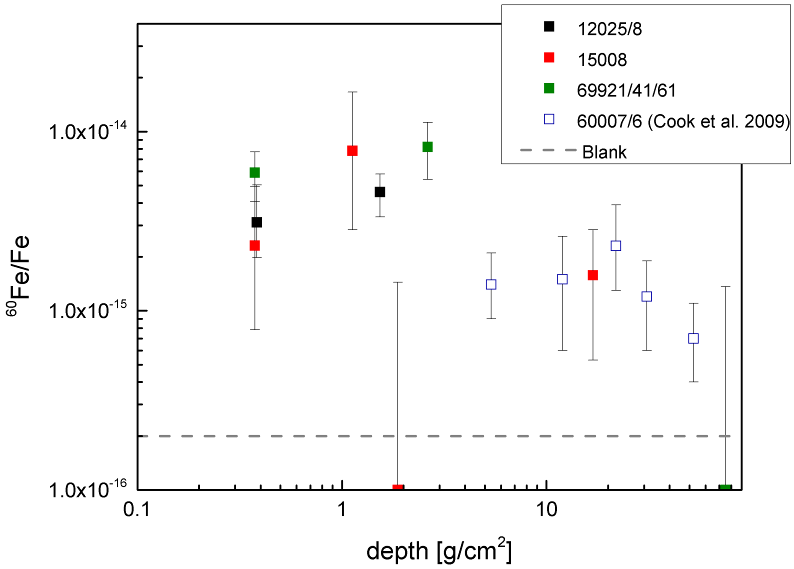

Figure 5.5. ^{60}Fe measurements up to this date in lunar samples. Data points for samples from cores 12025 (black full squares) and 15008 (red full squares), shaded samples 69921/41/61 (green full squares) were measured in this work. The results for the 60007/6 core (blue empty squares), published by Cook et al. [2009] are also included.

and shown in Fig. 4.16. The weighted mean of these results is (0.58 ± 0.05) dpm/kg Ni. This value is included in Fig. 5.6.

All samples (except the ones were no ^{60}Fe was observed) measured during this work have activities greater than the weighted mean in iron meteorites. This is a strong hint against meteoritic contamination of the samples or *in-situ* production of ^{60}Fe due to GCR. Compared with this new estimation of the cosmogenic contribution, samples 60007,517, 60007,515 and 60007,514 also have activities that are higher than the average.

Even adding both SCR and GCR contributions, this cannot account for the high ^{60}Fe activities observed in almost every sample measured during this work, which points to the deposition of interstellar material on the lunar surface.

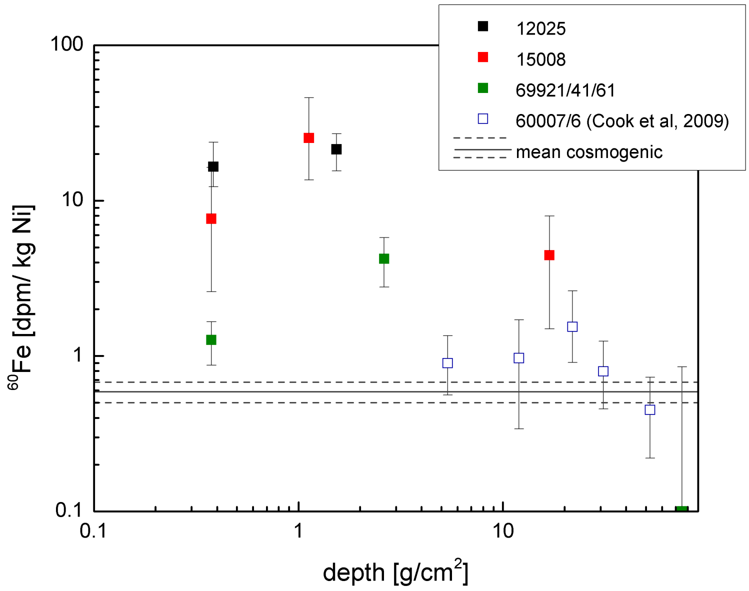

Figure 5.6. ^{60}Fe results, expressed in dpm/kg Ni. Data points for samples from cores 12025 (black full squares) and 15008 (red full squares), shaded samples 69921/41/61 (green full squares) were measured in this work. The results for the 60007/6 core (blue empty squares), published by Cook et al. [2009] are also included. The dark grey line is the weighted mean of the activity measured in 15 iron meteorites [Nishiizumi and Honda, 2007; Knie et al., 1999b; Berger et al., 2007, and this work], the dashed line corresponding to a 1 SD.

5.3 Interpretation of the results

It is interesting to relate the activities of ^{53}Mn and ^{60}Fe, as it is shown in Fig. 5.7. Samples labeled 1 through 11 are lunar samples, samples 12 through 18 are iron meteorites. Moon samples 69961 and 15008,1052 were excluded since they both showed no ^{60}Fe events. All colored numbers in the graph from Fig. 5.7 correspond to the new samples measured during this work. Black numbers are the results from the iron meteorites.

An almost linear trend is distinct among the black numbers in Fig. 5.7. This corresponds to the cosmogenic production of ^{53}Mn and ^{60}Fe in iron meteorites and their not much different half lives. The grey dashed line is a linear fit (dotted lines corresponds to 1 σ error) of the meteorite data that illustrates this trend. Throughout the iron meteorites, a constant ratio of A(^{53}Mn)/A(^{60}Fe) $\sim$ 300 is maintained. Samples 1, 2 (12025,14 and 23, respectively), 4 (69941), 5, 6 and 7 (15008,1050, 1051 and 1053 respectively) lie

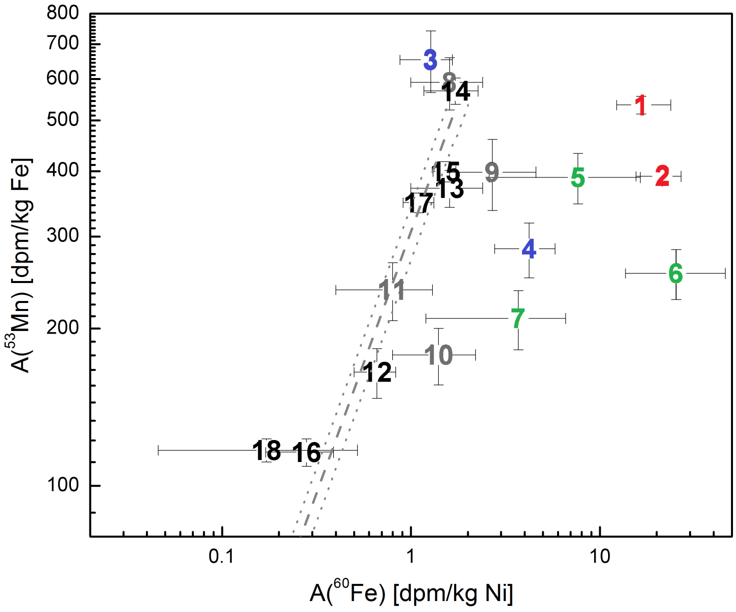

Figure 5.7. ^{53}Mn versus ^{60}Fe. 1:12025,14, 2:12025,23 (red); 3: 69921, 4: 69941 (blue); 5: 15008,1050, 6: 15008,1051, 7:15008,1053 (green); 8: 60007,517, 9: 60007,515, 10: 60007,514, 11: 60006,418 (grey), 12 - 18: iron meteorites (Dermbach, Emery, NWA Iron, Gebel Kamil Id, Gebel Kamil Sd, Gebel Kamil If, Gebel Kamil Se, respectively) (black). Samples 69961 and 15008,1052 were excluded, since they both showed 0 events for ^{60}Fe. The grey dashed line is a linear fit of the meteorite data only, the dotted lines correspond to the error of the fit.

outside this linear trend. Samples 9 and 10 (60007,515 and 60007,514 respectively) are located only slightly away from the trend.

Sample 69921 shows the highest ^{53}Mn activity ever measured in a lunar sample [Fruchter et al., 1981]. This sample was collected from the shadow cast by a small boulder during the Apollo 16 mission. As it was already explained earlier, after the comparison with the activity measured from the top of the boulder, which was considerably low taking into account the time this rock was at this place, it was assumed that eroded material from the top of the boulder fell into the position from where sample 69921 was taken. The fact that the activity of ^{60}Fe in the same sample is not considerably high suggests that the scenario described by Fruchter et al. [1981] may be feasible and the eroded material that fell in that position diluted the sought SN signature. This is supported by the fact that sample 69941, which originates from underneath sample 69921, has a higher ^{60}Fe activity.

This is the first time a systematic measurement of both ^{53}Mn and ^{60}Fe in identical lunar samples was performed. The origin of the high ^{60}Fe activities observed in samples 1, 2, 4, 5, 6, 7, 9 and 10 cannot be explained with *in-situ* production due to SCR and/or GCR only. For this reason, the origin of these values is definitely not cosmogenic.

Regarding the excess of ^{60}Fe observed, it is possible to obtain an estimation of the local interstellar fluence:

$$\Phi = 4 \int_0^{D_{\max}} \mathrm{c}(^{60}\mathrm{Fe})\ \mathrm{d}D \tag{5.1}$$

where c(^{60}Fe) is the observed quantity of ^{60}Fe atoms per kilogram of lunar soil and D is the depth expressed in kg/cm^2, calculated using the bulk density from each set of samples.

In order to estimate the local interstellar fluence Φ the expected contribution due to GCR was subtracted from each result. The black squares in Fig. 5.8 show the resulting profile, ^{60}Fe atoms per kg of soil as a function of depth, where samples having activities compatible with the expected GCR contribution were ignored. The concentration of ^{60}Fe seems to increase up to the first centimeter and then decreases. Given the uncertainties of the results it is difficult to estimate how deep in the lunar surface the expected deposition of freshly synthesized material is likely to be found. The red dashed curves in Fig. 5.8 are two proposed estimated profiles. The curve that goes deeper takes into account the samples that are separated by 1 σ from the linear trend in Fig. 5.7 (samples 1, 2, 4, 5, 6, 7, 9, and 10 in Fig. 5.7). The more shallow curve took into account only samples that are separated by 2 σ from the expected cosmogenic trend (samples 1, 2, 4, 5, and 6 in Fig. 5.7).

It is expected that the deposited material remains in the surface of the lunar regolith, and due to gardening, this material is further mixed into the first centimeters of the lunar surface. For example, according to Gault et al. [1974], it is very improbable that more than one centimeter of the lunar regolith has been mixed during a time period comparable with the half life of ^{60}Fe. Nevertheless, high activities were observed in several deeper samples. A few remarks about the results obtained for the three deepest samples in Fig. 5.8 need to be made at this point.

The elevated concentration of the deepest sample we obtained from the Apollo 15

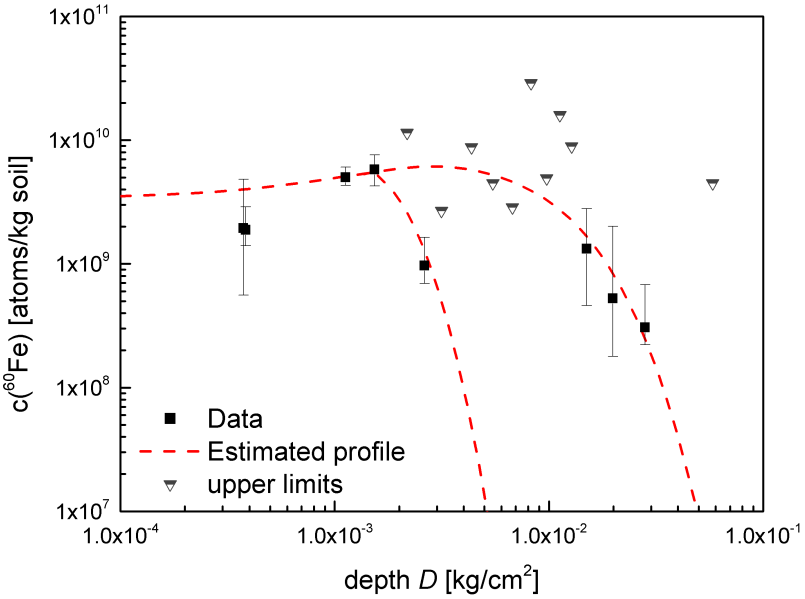

Figure 5.8. ^{60}Fe depth profile, constructed with the samples lying above the expected GCR contribution. The red dashed lines are estimations of the depth profile used to integrate it and obtain a local interstellar fluence of ^{60}Fe. The first sample has a depth of 0.2 cm and the last one 18.75 cm. The half full triangles are the upper limits obtained by Cook et al. [2009].

core (15008,1053, depth (11.25$\pm$0.25) cm, number 7 in Fig. 5.7) could be explained with the observations of Nagle [1980] and Fruchter et al. [1981]. This core was taken from the rim of a small crater and their studies suggested that the top part of the core is composed by infilled material from the crater's rim. This infilling seems to have taken place until 1.5 - 2 Myr ago and could have buried some of the freshly deposited material.

The two deepest samples in Fig. 5.8 are 2 samples from the Apollo 16 60007/6 core (numbers 9 and 10 in Fig. 5.7, depths) are less than 2 σ apart from the expected A(^{53}Mn)/A(^{60}Fe) ratio. Cook et al. [2009] already discarded them in their work, but with the new estimation of the rate of production of ^{60}Fe in iron meteorites it seems that an excess, although not significant, is also observed here.

From the integrated deposition of about $1\times10^7-5\times10^7$ atoms/cm^2 a local interstellar fluence of ^{60}Fe of $4\times10^7-2\times10^8$ at/cm^2 is inferred. The value originally estimated by Knie et al. [2004] was 2×10^9 at/cm^2 and it is known that it should be corrected and should be 2 orders of magnitude lower, due to a higher uptake factor in the crust. This correction is suggested after Auer et al. found out that the ^{53}Mn flux in ice was $\sim$ 160 times smaller than the previously determined value by Bibron et al. [1974] and used by Knie et al. to estimate the uptake factor of ^{60}Fe in the ferromanganese crust.

The yield of ^{53}Mn atoms produced in a SN is similar or up to an order of magnitude higher than ^{60}Fe for stars with masses between 10 and 25 $M_\odot$ [see Figs. 2.2 and 2.3 in chapter 2, or Woosley and Weaver, 1995; Rauscher et al., 2002]. Since ^{53}Mn is copiously produced in the lunar surface by spallation reactions on iron, it is difficult to accurately discern if the observed ^{53}Mn activities are partly of SN origin. ^{53}Mn production on the surface of the Moon is dominated by SCR over GCR down to a depth of $\sim$ 10 cm [Reedy and Arnold, 1972] and it corresponds with the values observed in the lunar samples. The samples that showed significantly high ^{60}Fe activities also have a higher than average ^{53}Mn activity. Deviations with respect to the expected theoretical profile were interpreted as mixing of the regolith.

Given the ^{53}Mn production yields in massive stars compared to ^{60}Fe, the results obtained for the latter radioisotope, the average concentration of iron in the lunar regolith of approximately 10%, and the fact that ^{53}Mn is abundantly produced in the lunar surface by SCR and GCR, the expected contribution from a possible SN source to the ^{53}Mn activity on the Moon is neglegible. The estimated interstellar contribution is at least three orders of magnitude lower than the observed activities, despite optimistic calculation.

Chapter 6

Conclusion

The subject of this work was the study of lunar samples in order to find a signature of a recent deposition of supernova (SN) debris. The finding of an ^{60}Fe/Fe spike in a ferromanganese crust [Knie et al., 2004; Fitoussi et al., 2008] was the first indication of such an event in the vicinity of our solar system. From the concentration found in the layer with the ^{60}Fe excess, which was measured with the ultra-sensitive accelerator mass spectrometry technique (AMS) Knie et al. [1997], a local interstellar fluence of ^{60}Fe related to this event of $\Phi \approx 2 \times 10^9$ at/cm^2 was estimated. With the measurement of a ^{10}Be depth profile, to determine the growth rate of the crust [Fitoussi et al., 2008], it was found that this layer was $1.7 - 2.6$ Myr old.

The estimation of the distance of the alleged SN explosion is not straightforward. It is known that the Local Bubble, a hot sparse cavity in the interstellar medium (ISM) in the same region where our Solar System is, was excavated by $14 - 20$ supernovae (SNe), the last of them occurring 0.5 Myr ago [Fuchs et al., 2006]. It is suggested, that the SNe that created this cavity contributed to the excess of ^{60}Fe found by Knie et al. [Berghöfer and Breitschwerdt, 2002]. Therefore, it is not possible to associate the observed ^{60}Fe excess with a single SN event unequivocally. Assuming however a single SN of a star with solar metallicity, this assumed SN was estimated to be at a distance of approximately 40 pc [Knie et al., 2004]. It seems that there are some problems with this model. The local interstellar fluence of ^{60}Fe has to be corrected, since its estimation was based on the cosmogenic ^{53}Mn flux in ice [Bibron et al., 1974] and this value need to be improved [Auer et al.]. This ^{53}Mn flux was used to infer an uptake factor of ^{60}Fe in the crust, that is, the percentage of iron that was actually incorporated in the crust.

The local interstellar fluence of ^{60}Fe can be estimated with the measurement of an ^{60}Fe depth profile in the lunar surface. Due to its lack of atmosphere and water, the deposited material is believed to remain on the first centimeters of the lunar surface. This is only diluted due to gardening, *i.e.* a constant stirring of the lunar regolith due to stochastic impacts of micrometeorites. This deposition must be differentiated from the locally produced ^{53}Mn and ^{60}Fe via spallation reactions by solar and galactic cosmic rays (SCR and GCR, respectively).

Over the course of this work, an ^{60}Fe depth profile in lunar samples, collected during three Apollo missions (Apollo 12, 15 and 16) was measured via AMS. Additionally, the same samples were analyzed for their ^{53}Mn concentrations. To estimate the cosmogenic contribution, a series of iron meteorites were analyzed for both radionuclides and these results were then compared with the results on the lunar samples. In the next sections the principal observations and conclusions of this work are going to be summarized.

On the correlation of ^{53}Mn and ^{60}Fe activities and the possibility of interstellar origin of the signals

To experimentally determine the local production due to GCR of ^{53}Mn and ^{60}Fe on the lunar surface, a set of samples coming from 4 different iron meteorites were analyzed in order to determine the activity of these two isotopes. Since these meteorites are composed mainly of the principal target material (iron and nickel) for the spallogenic production of ^{53}Mn and ^{60}Fe, they should provide a close picture to which the activities observed in lunar samples can be compared. A clear correlation was found between the activity of ^{53}Mn and of ^{60}Fe in this set of samples. The ratio between the activities of ^{53}Mn and ^{60}Fe, each normalized to the content of its principal spallogenic target material, is constant: A(^{53}Mn)/A(^{60}Fe) $\sim$ 300. The contribution to spallative synthesis of ^{60}Fe from SCR was already discarded by Cook et al. [2009].

This was then compared to the activities observed in the lunar soils. Samples showing a significantly higher ^{60}Fe activity than expected due to GCR also showed a higher than average ^{53}Mn activity. Five samples (1, 2, 4, 5, and 6 in Fig. 5.7 in chapter 5) were found to have an activity significantly higher than the mean expected value determined with iron meteorites. Since the high activity of ^{60}Fe observed in these samples cannot be explained only with the spallogenic production via GCR or SCR, it is assumed that the excess found in the lunar surface is of interstellar origin. Considering SNe produce appreciable quantities of both ^{60}Fe and ^{53}Mn whereas AGB stars produce ^{60}Fe but little ^{53}Mn, it is inferred that interstellar material from either SNe only or both sources may be present on the lunar surface. This was the first time that ^{53}Mn and ^{60}Fe were systematically measured in identical lunar samples.

On the local interstellar fluence of ^{60}Fe

As mentioned in the previous chapter, the determination of the local interstellar fluence Φ is not straightforward. The choice for the margin of errors is rather conservative and takes into account that estimations of GCR production of both ^{60}Fe and ^{53}Mn are not completely understood. Additionally, the effects of gardening by micrometeorites introduces large uncertainties to any considerations about depth. The value obtained in this work is 4×10^7 at/cm^2 $< \Phi < 2 \times 10^8$ at/cm^2. As mentioned earlier, the upper and lower limits were obtained by taking only samples with more ^{60}Fe than expected from GCR production on a 1 and 2 σ level into account, respectively. This value would fit very well with the one determined by Knie et al. [2004], after the proposed correction from Auer et al..

The upper limit seems, however, optimistic, considering the turnover depth for e.g. three ^{60}Fe half lives $3T_{1/2} \sim 7.8$ Myr , which is only $\sim$ 1cm [Gault et al., 1974], while the profile reaches down to almost 20 cm. Since the deeper samples all come from cores with rather complicated gardening and exposure histories, it could be possible that these were isolated mixing events and do not represent typical scenarios in the lunar surface. The lower limit, although conservative in the light of the results, seems to originate from a more average scenario.

Given the results obtained for ^{60}Fe, the expected interstellar contribution to the total ^{53}Mn activity is some orders of magnitude lower than the observed values. This makes the detection of interstellar ^{53}Mn on the lunar surface impossible.

Appendix A

Data acquisition and analysis

In Fig. A.1 a schematically view of the data adquisition electronics is shown. A set of 9 *raw* signals for each event is saved:

eiL-eiR: i=1,2 the signal of each part of the first two segments of the anode

e3 - e5: the signal of the three last segments of the detector

Et: the signal of the Frisch grid

dt: time difference between e1 and e3: angle of entrance in the y-direction.

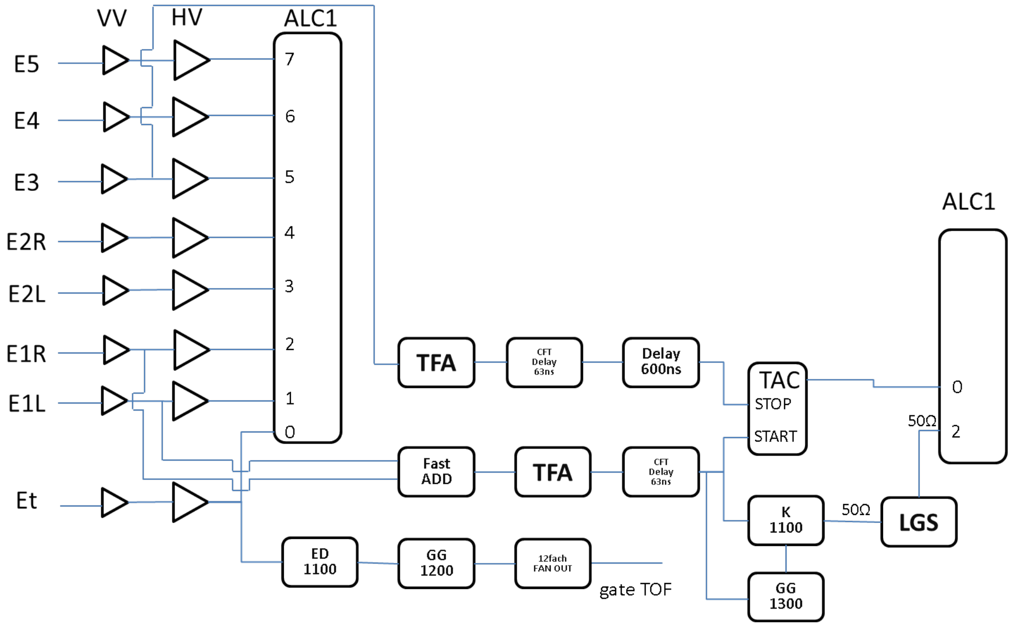

Figure A.1. Schematic view of the adquisition electronics.

With these raw signals, additional signals are calculated:

ei: i=1,2 energy loss in the first two segments of the anode

p_i: i=1,2 position of entrance in the detector

dp: angle in the x-direction

The position is calculated using the following formula:

$$p_i = \frac{l}{2}\left(\frac{E_{iL} - E_{iR}}{E_{iL} + E_{iR}}\right) \tag{A.1}$$

with $i = 1, 2$ and l =145 mm, the width of the anode.

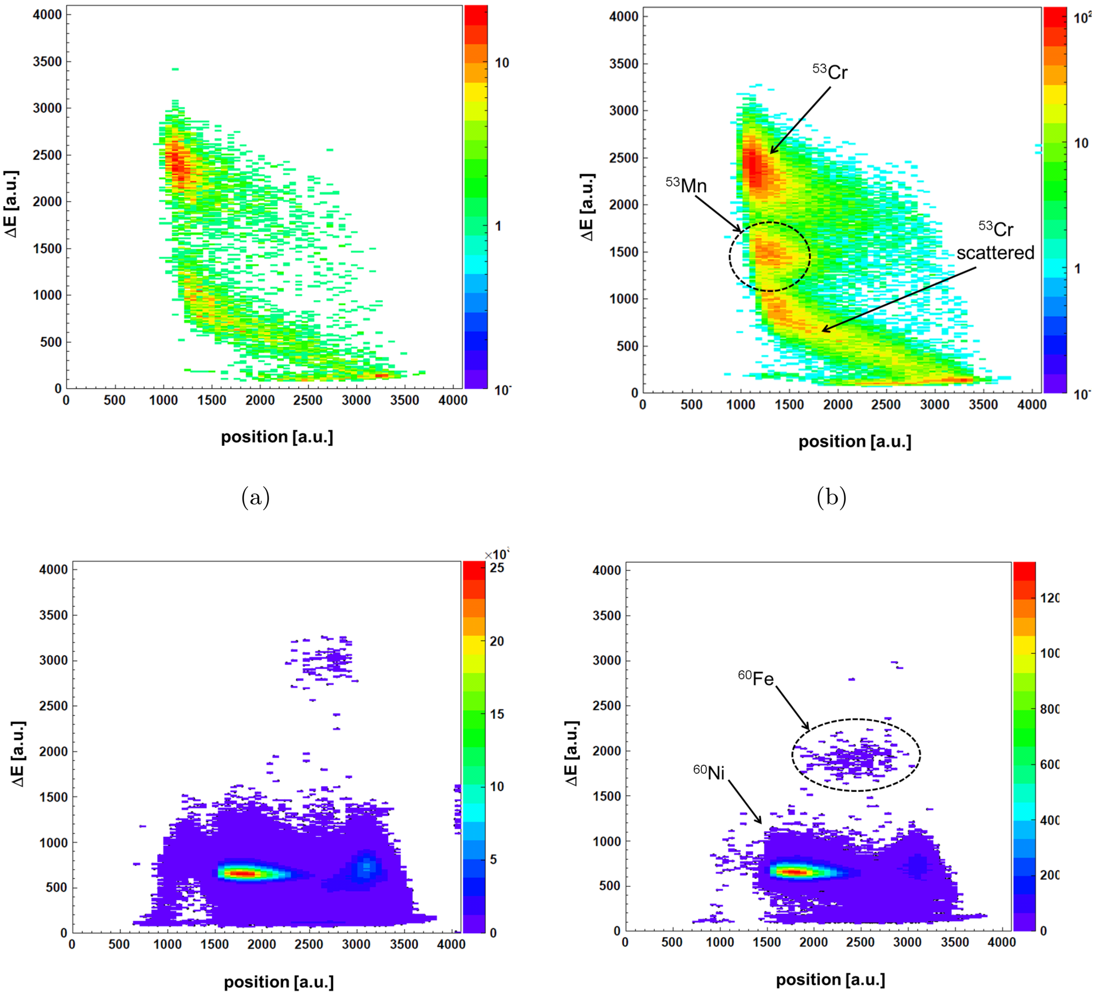

(a) (b)

(c) (d)

Figure A.2. Spectra of (a) ^{53}Mn blank sample, (b) ^{53}Mn standard sample, (c) ^{60}Fe blank sample, and (d) ^{60}Fe standard sample.

Comparing the spectra of the blank and the standard sample, one can easily identify the radioisotope and the interfering isobar (see, for example, Fig. A.2). Comparing the one dimentional energy loss spectra one can set the so called software cuts or windows, namely the range in each spectrum where the events related to the interesting radioisotope lie. This is possible not only in the differential energy loss spectra, but in the spectra corresponding to the angle in x and y-direction. One can as well determine the mean $\langle x_i \rangle$ and the standard deviation σ_i for each distribution of radioisotope related events, used them to calculate a χ^2 parameter for each event

$$\chi^2 = \sum_{i=1}^{6} \left(\frac{x_i - \langle x_i \rangle}{\sigma_i} \right)^2 \tag{A.2}$$

and define a window for this as well. Here i = E1, ..., E5 and Et. A χ^2 probability distribution with 6 degrees of freedom has its maximum at $\chi^2_{\mathrm{max}} = 4$ and events with $\chi^2 \leq 12$ were accepted as real.

In this process one have to compromise between the sensitivity of the measurement and the transmission through the GAMS. If the presence of impurities in the samples is to high, one can set the windows in a more restrictive way, with the risk of obtaining a low transmission or even losing a few of counts of the radioisotope.

The window-sets are defined in all one-dimentional spectra but a couple of them, usually one of the differential E_i, where the radioisotope and its stable isobar are well separated, and position signals. The final step is to define a two-dimentional region of interest in this E_i *versus* position graph, as, for example, in Fig. A.3.

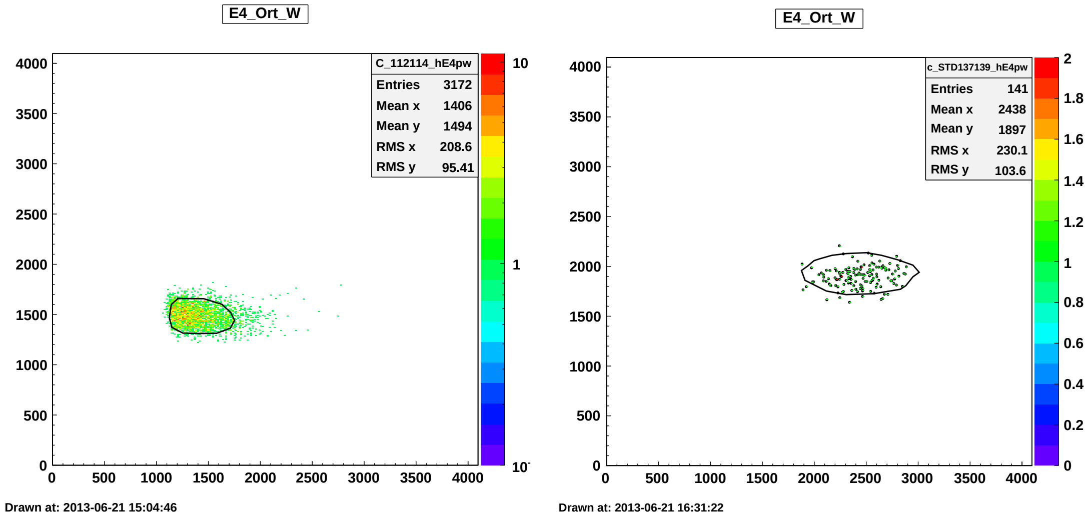

(a) (b)

Figure A.3. ^{53}Mn and ^{60}Fe spectra of a standard sample with windows and two-dimentional cuts.

The uncertainity is mostly dominated by the statistics in the measurements. When the number of counts detected was N $\leq$ 20, the calculation of the statistical uncertainity was done as in Feldmann and Cousins [1998]. For N $>$ 20 the statistical uncertainity was computed as the Gaussian interval $\pm\sqrt{N}$. Additionally, a 10% systematical uncertainity was taken into account, coming from beam fluctuations and the measurement of the current before and after a run. These two values are interpolated and it is assumed, that the current is stable during the run. This was quadratically added to the statistical uncertainities to obtain the final results reported in the work.

Appendix B

Chemical preparation of the samples

B.1 Meteorite samples

The chemical preparation of the metorite samples was done as described in Merchel and Herpers [1999]. Samples were diluted in HNO_3, after Al, Be, and Mn (1 mg, 10 mg, and 4 mg, respectively) carriers was added. Iron was extracted from HCl (7.1 mol/l) into diisopropyl ether and then back extracted from the organic phase into water and FeO(OH) was precipitated with NH_3aq. Further purification was achieved by anion exchange to reduce nickel. The rest of the sample was evaporated and redissolved in HCl (10 mol/l). This solution was charged into an anion exchange column and an eluate containing Be, Al, and Ni was collected. Finally, Mn was eluated with 7.1 mol/l HCl, after disgarding a portion of eluate containing relatively high amounts of chromium. $KCLO_3$ was added to the Mn fraction to oxidate Mn(II) to Mn(IV). After the sample was dried, it was ignited to MnO_2 at 500°C.

For further details, the reader is referred to Merchel and Herpers [1999].

B.2 Lunar samples

To all samples (60 to 190 mg) 8 mg Be carrier and 10 mg Mn carrier was added. Only to samples 12025,14 and 23, 8 mg Al carrier was incorporated. After digestion in 5 ml 7M HNO_3, 5 ml concentrated HF, and 1 ml concentrated $HClO_4$, an aliquot (5 wt%) of the resulting solution was taken for elemental analysis by ICP-MS. The rest (main sample) was evaporated and re-dissolved in 8M HCl from which iron was extracted with di-isopropyl ether and then back extracted into 1M HCl. The main sample (minus iron) was evaporated once again and dissolved in 9M HCl for separation of Mn from Be and Al by anion exchange. Mn was precipitated from the Mn eluate with $KClO_3$ as MnO_2. Be and Al were separated by cation exchange, precipitated with NH_3, and ignited to make the oxides. ICP-MS was used to determine the elemental compositions of the sample aliquots.

Appendix C

Summary of results

C.1 Meteorite samples

Sample	^{53}Mn/Mn [10^{-9}]	^{53}Mn [dpm/kg Fe]	^{60}Fe/Fe [10^{-14}]	^{60}Fe [dpm/kg Ni]
NWA Iron	3.09 ± 0.18	569 ± 33	1.72 ± 0.55	$1.3^{+0.4}_{-0.3}$
Gebel Kamil Se	0.71 ± 0.04	117 ± 6	0.83 ± 0.40	0.18±0.09
Gebel Kamil Sd	0.74 ± 0.05	116 ± 7	1.29 ± 0.50	0.28±0.11
Gebel Kamil Id	2.05 ± 0.12	399 ± 18	6.82 ± 0.95	1.52±0.21
Gebel Kamil If	1.12 ± 0.06	348 ± 15	4.58 ± 0.91	1.09±0.22
Piñon			3.43 ± 0.70	0.97±0.20
Gan-Gan			3.89 ± 0.59	2.1±0.3

Table C.1. Results of the measurements of iron meteorites performed during this work.

C.2 Lunar samples

Sample	Depth [cm]	^{10}Be/Be [10^{-12}]	^{10}Be [dpm/kg]	^{26}Al/Al [10^{-11}]	^{26}Al [dpm/kg]
12025,14	0.2 ± 0.2	1.11 ± 0.04	9.32 ± 0.37	2.66 ± 0.21	230 ± 18
12025,23	0.8 ± 0.4	1.23 ± 0.04	9.78 ± 0.31	2.62 ± 0.21	216 ± 18
15008,1050,1004	0.25 ± 0.25	1.37 ± 0.04	8.79 ± 0.26	4.68 ± 0.26	188 ± 10
15008,1051,1005	0.75 ± 0.25	1.49 ± 0.04	8.71 ± 0.23	3.73 ± 0.29	138 ± 11
15008,1052,1006	1.25 ± 0.25	1.58 ± 0.04	9.83 ± 0.28	3.77 ± 0.25	140 ± 9
15008,1053,1026	11.25 ± 0.25	1.47 ± 0.04	9.05 ± 0.24	1.52 ± 0.13	60 ± 5
69921,31,0	~ 0.5	3.42 ± 0.12	9.32 ± 0.32	4.44 ± 0.39	243 ± 21
69941,138,42	~ 3	2.95 ± 0.24	8.79 ± 0.71	2.25 ± 0.14	123 ± 8
69961,143,38	under boulder	3.58 ± 0.07	10.79 ± 0.21	1.23 ± 0.10	67 ± 6

Table C.2. Results of the ^{10}Be and ^{26}Al measurements in the lunar samples.

Sample	Depth [cm]	^{53}Mn/Mn [10^{-11}]	^{53}Mn [dpm/kg Fe]	^{60}Fe/Fe [10^{-15}]	^{60}Fe [dpm/kg Ni]
12025,14	0.2 ± 0.2	4.05 ± 0.68	535 ± 21	$3.1^{+1.9}_{-1.1}$	$16.6^{+7.2}_{-4.3}$
12025,23	0.8 ± 0.4	2.54 ± 0.50	391 ± 14	$4.6^{+1.2}_{-1.3}$	$21.4^{+5.6}_{-5.9}$
12025,30,360	1.45 ± 0.25	4.11 ± 0.76	455 ± 84	$< 8^*$	$< 30^*$
12025,11,357	2.1 ± 0.4	2.25 ± 0.47	297 ± 62	$< 2^*$	$< 7^*$
12025,10,356	2.9 ± 0.4	$2,45 \pm 0.39$	327 ± 52	$< 6^*$	$< 23^*$
12025,9,355	3.65 ± 0.35			$< 3^*$	$< 11^*$
12025,8,354	4.5 ± 0.5			$< 2^*$	$< 11^*$
12025,41,361	5.5 ± 0.5	2.19 ± 0.47	294 ± 64	$< 20^*$	$< 76^*$
12025,50,362	6.5 ± 0.5	1.17 ± 0.33	153 ± 43	$< 4^*$	$< 12^*$
12025,53,363	7.5 ± 0.5	2.01 ± 0.26	213 ± 27	$< 11^*$	$< 42^*$
12025,55,364	8.5 ± 0.5	1.80 ± 0.35	220 ± 43	$< 6^*$	$< 23^*$
12028,493,837	38.7 ± 0.5	1.33 ± 0.33	153 ± 38	$< 3^*$	$< 11^*$
15008,1050,1004	0.25 ± 0.25	6.49 ± 0.71	389 ± 43	$2.3^{+2.6}_{-1.5}$	$7.6^{+8.7}_{-5.1}$
15008,1051,1005	0.75 ± 0.25	5.76 ± 0.64	255 ± 28	$7.8^{+1.3}_{-2.2}$	$25.3^{+4.1}_{-4.0}$
15008,1052,1006	1.25 ± 0.25	5.52 ± 0.63	382 ± 44	< 1.3	< 3.8
15008,1053,1026	11.25 ± 0.25	2.95 ± 0.38	209 ± 27	$1.6^{+1.3}_{-1.1}$	$3.7^{+2.9}_{-2.5}$
60007,517,78	3.25 ± 0.25	12.4 ± 1.2	591 ± 68	$1.4^{+0.7*}_{-0.5}$	$1.6^{+0.8*}_{-0.6}$
60007,516,62	7.25 ± 0.25			$1.5^{+1.1*}_{-0.9}$	$1.7^{+1.3*}_{-1.1}$
60007,515,36	13.25 ± 0.25	8.25 ± 1.28	398 ± 62	$2.3^{+1.6*}_{-1.0}$	$2.7^{+1.9*}_{-1.1}$
60007,514,15	18.75 ± 0.25	4.01 ± 0.49	178 ± 22	$1.2^{+0.7*}_{-0.6}$	$1.4^{+0.8*}_{-0.6}$
60006,418,99	0.25 ± 0.25	5.01 ± 0.63	237 ± 30	$0.7^{+0.4*}_{-0.3}$	$0.8^{+0.5*}_{-0.4}$
69921,31,0	~ 0.5	8.87 ± 1.19	653 ± 88	5.9 ± 1.8	1.3 ± 0.4
69941,138,42	~ 3	5.00 ± 0.60	284 ± 34	$4.2^{+1.6}_{-1.4}$	$4.2^{+2.6}_{-2.5}$
69961,143,38	under boulder	4.52 ± 0.51	452 ± 51	< 1.3	< 0.8

Table C.3. Results of the ^{53}Mn and ^{60}Fe measurements in the lunar samples studied during this work. Values marked with * are from Cook et al. [2009] and are only included to give a complete picture of the measurements of ^{60}Fe done so far in lunar samples.

List of Figures

List of Tables

Bibliography

Alpher, R., Bethe, H., Gamov, G., 1948. The origin of chemical elements. Physical Review 73.

ALSJ, 2013. Apollo Lunar Surface Journal. www.hq.nasa.gov/alsj/frame.html .

Alvarez, L., Cornog, R., 1939a. He^3 in Helium. Physical Review 56, 379.

Alvarez, L., Cornog, R., 1939b. Helium and Hydrogen of Mass 3. Physical Review 56, 613.

Ammon, K., Masarik, J., Leya, I., 2009. New Model calculations for the production rates of cosmogenic nuclides in iron meteorites. Meteoritics & Planetary Science 44, 485.

Arnold, J., 1975. Monte Carlo simulation of turnover processes in the lunar regolith, pp. 2375–2395.

Auer, M., Korschinek, G., Faestermann, T., . Unpublished.

Behrmann, C., Crozaz, G., R.J., D., Hohenberg, C., Ralston, C., Walker, R., Yuhas, D., 1973. Cosmic-ray exposure history of the North Ray and South Ray material. Geochimica et Cosmochimica Acta 2, 1957.

Benitez, N., Maiz-Apellaniz, J., Canelles, M., 2002. Evidence for Nearby Supernova Explosions. Physical Review Letters 88, 081101.

Berger, E., Faestermann, T., Herzog, G., Knie, K., Korschinek, G., Leya, I., Serefiddin, F., 2007. Iron-60 activities of Canyon Diablo, Grant and Dorofeevka. Proceedings of the 70th Annual Meteoritical Society Meeting , 5241.

Berghöfer, T., Breitschwerdt, D., 2002. The origin of the young stellar population in the solar neighborhood - A link to the formation of the Local Bubble? Astronomy and Astrophysics 390, 299.

Bibron, R., Chesselet, R., Crozaz, G., Leger, G., Mennessier, J., Picciotto, E., 1974. Extra-terrestrial ^{53}Mn in Antarctic ice. Earth and Planetary Science Letters 21, 109–116.

Burbidge, E., Burbidge, G., Fowler, W., Hoyle, F., 1957. Synthesis of the elements in stars. Reviews of Modern Physics 29.

Choppin, G., Liljenzin, J., Rydberg, J., 2002. Radiochemistry and nuclear chemistry. Butterworth-Heinemann.

Cook, D., Berger, E., Faestermann, T., Herzog, G., Knie, K., Korschinek, G., Poutisev, M., Rugel, G., Serefiddin, F., 2009. ^{60}Fe, ^{10}Be, and ^{26}Al in lunar cores 12025/8 and 60006/7: search for a nearby supernova, in: Proceedings of the 40th Lunar and Planetary Science Conference, p. 1129.

Drechsler, G., Boesl, U., Bassmann, C., Schlag, E., 1997. Mass selected anion-zero kinetic energy photoelectron spectroscopy (anion-ZEKE): Ground and low excited states of FeO. Journal of Chemical Physics 107, 2284.

Drozd, R., Hohenberg, C., Morgan, C., Ralston, C., 1974. Cosmic-ray exposure history at the Apollo 16 and other lunar sites: lunar surface dynamics. Geochimica et Cosmochimica Acta 38, 1625.

Ellis, J., Schramm, D., 1995. Could a nearby supernova explosion have caused a mass extiction? Proceedings of the National Academy of Sciences 92, 235.

Evans, J., Fruchter, J., Reeves, J., Rancitelli, L., Perkins, R., 1980. Recent depositional history of Apollo 16 and 17 cores. Proceedings of the 11th Lunar and Planetary Science Conference , 1497.

Feige, J., Wallner, A., Winkler, S., Merchel, S., Fifield, L., Korschinek, G., Rugel, G., Breitschwerdt, D., 2012. The search for supernova-produced radionuclides in terrestrial deep-sea archives. Publications of the Astronomical Society of Australia 29, 109–116.

Feldmann, G., Cousins, R., 1998. Unified approach to the classical statistical analysis of small signals. Physical Review D 57, 3873.

Fink, D., 2010. AMS-11 in Rome, 2008: Past achievements, current and future trends. Nuclear Instruments and Methods in Physics Research B 268, 1334.

Fitoussi, C., Raisbeck, G., Knie, K., Korschinek, G., Faestermann, T., Goriely, S., Lunney, D., Poutivtsev, M., Rugel, G., Waelbroeck, C., Wallner, A., 2008. Search for Supernova-produced Fe-60 in a Marine Sediment. Physical Review Letters 101, 121101.

Fruchter, J., Evans, J., Reeves, J., Perkins, R., 1982. Measurements of ^{26}Al in Apollo 15 core 15008 and ^{22}Na in Apollo 17 rock 74275, in: Proceedings of the Lunar and Planetary Institute Science Conference, p. 243.

Fruchter, J., Rancitelli, L., Laul, J., Perkins, R., 1977. Lunar regolith dynamics based on analysis of the cosmogenic radionuclides ^{22}Na, ^{26}Al, and ^{53}Mn, pp. 3595–3605.

Fruchter, J., Rancitelli, L., Perkins, R., 1976. Recent and long-term mixing of the lunar regolith based on ^{22}Na and ^{26}Al measurements in Apollo 15, 16, and 17 deep drill stems and drive tubes. Proceedings of the 7th Lunar Science Conference , 27–39.

Fruchter, J., Reeves, J., Evans, J., Perkins, R., 1981. Studies of lunar regolith dynamics using measurements of cosmogenic radionuclides in lunar rocks, soils and cores. Proceedings of the 12th Lunar and Planetary Science Conference , 567.

Fuchs, B., Breitschwerdt, D., a. de Avillez, M., Dettbarn, C., Flynn, C., 2006. The search for the origin of the Local Bubble redivivus. Monthly Notices of the Royal Astronomical Society 373, 993–1003.

Fuse, K., Anders, E., 1969. Aluminium-26 in meteorites - VI. Achondrites. Geochimica et Cosmochimica Acta 33, 653–670.

Gamov, G., 1946. Expanding universe and the origin of elements. Physical Review 70, 572.

Gault, D., Hörz, F., Brownlee, D., Hartung, J., 1974. Mixing of the lunar regolith. Geochimica et Cosmochimica Acta 373, 2365–2386.

Heiken, G., Vaniman, D., French, B. (Eds.), 1991. Lunar sourcebook, a user's guide to the moon. 1 ed., Cambridge University Press.

Honda, M., Imamura, M., 1971. Half-life of ^{53}Mn. Physical Review C 4, 1182.

Imamura, M., Inoue, T., Nishiizumi, K., Tanaka, S., 1979. ^{53}Mn in Deep-Sea Sediment Cores - An Indicator of Past Solar Activity, in: 16th International Cosmic Ray Conference Proceedings, pp. 304–307.

Imamura, M., Nishiizumi, K., Honda, M., 1974. Depth profiles of ^{53}Mn in lunar rocks and soils, pp. 2093–1203.

Jahresbericht, 1970. Beschleunigerlaboratorium der Universität und der Technische Universität München. Technical Report.

Janka, H., 2012. Explosion Mechanisms of Core-Collapse Supernovae. The Annual Review of Nuclear and Particle Science 62, 407.

Karakas, A., Lattanzio, J., 2007. Stellar models and yields of asymptotic giant branch stars. Publications of the Astronomical Society of Australia 24, 103.

Knie, K., 1997. Beschleunigermassenspektrometrie mit Isobarenseparation in einem dedizierten gasgefüllten Magneten. Ph.D. thesis. Technical University of Munich.

Knie, K., Faestermann, T., Korschinek, G., 1997. AMS at the Munich gas-filled analyzing magnet system GAMS. Nuclear Instruments and Methods in Physics Research B 123, 128.

Knie, K., Korschinek, G., Faesterman, T., Wallner, C., Scholten, J., Hillebrandt, W., 1999a. Indication for supernova ^{60}Fe on earth. Physical Review Letters 83, 18.

Knie, K., Korschinek, G., Faestermann, T., Dorfi, E., Rugel, G., Wallner, A., 2004. Fe Anomaly in a deep-sea Manganese Crust and implications for a nearby supernova source^{60}. Physical Review Letters 93.

Knie, K., Merchel, S., Korschinek, G., Faestermann, T., Herpers, U., Gloris, M., Michel, R., 1999b. Accelerator Mass Spectrometry measurements and model calculations on iron-60 production rates in meteorites. Meteoritics & Planetary Science 34, 729.

Koening, K., Hilaire, S., Duijvestijn, M., 2007. Proceedings of the International Conference on Nuclear Data for Science and Technologie , 211.

Korotev, R., 1981. Compositional trends in Apollo 16 soils. Proceedings of the 12th Lunar and Planetary Science Conference 12B, 577.

Korschinek, G., Urban, A., Nolte, E., 1986. Ion source study of AMS with ^{41}Ca at the Munich tandem accelerator laboratory, Research Laboratory for Archaeology. p. 108.

Krohn, V., 1962. Emission of negative ions from metal surfaces bombarded by positive cesium ions. Journal of applied physics 33, 3523.

Landgraf, M., Baggaley, W., Grün, E., Krüger, H., Linkert, G., 2000. Aspects of the mass distribution of interstellar dust grains in the solar system from in-situ measurements. Journal of Geophysical Research 105, 10343.

Leya, I., Masarik, J., 2009. Cosmogenic nuclides in stony meteorites revisited. Meteoritics & Planetary Science 44, 1061.

Leya, I., S., N., Wieler, R., Michel, R., 2001. The production of cosmogenic nuclides by galactic-cosmic ray particles for 2π exposure geometries. Meteoritics & Planetary Science 36, 1547.

Limongi, M., Chieffi, A., 2006. The nucleosynthesis of ^{26}Al and ^{60}Fe in solar metalicity stars extending in mass fromm 11 to 120 $M_{\odot}$: the hydrostatic and explosive contributions. The Astrophysical Journal 647, 483.

Llorca, J., Roszjar, J., Cartwright, J., Bischoff, A., Ott, U., Merchel, S., Rugel, G., Fimiani, L., Ludwig, P., Casado, J., ALlepuz, D., 2013. The Ksar Ghilane 002 shergolite - The 100th registered martian meteorite fragment. Meteoritics & Planetary Science 48, 493.

LROC, 2011. Lunar Reconnainssance Orbital Camera : High resolution global topographic map of the Moon. URL: `http://www.lroc.asu.edu`.

Ludwig, P., Egli, R., Bishop, S., Chernenko, V., Frederichs, T., Rugel, G., Merchel, S., Orgeira, M., 2013. Characgerization of primary and secondary magnetite in marine sediment by combinig chemical and magnetic unmixing techniques. Global and Planetary Change 110, 321.

Meier, A., 2006. Messung von in-situ produziertem Mn mit Beschleunigermassenspektrometrie. Diploma Thesis .

Merchel, S., 2012. personal comunication.

Merchel, S., Faestermann, T., Herpers, U., Knie, K., Korschinek, G., Leya, I., Michel, R., Rugel, G., Wallner, C., 2000. Thin- and thick-target cross sections for the production of ^{53}Mn and ^{60}Fe. Nuclear Instruments and Methods in Physics Research B 172, 806.

Merchel, S., Herpers, U., 1999. An update on radiochemical separation techniques for determination of long-lived radionuclides via accelerator mass spectrometry. Radiochimica Acta 84, 215.

Meyer, C.J., Brett, R., Hubbard, N., Morrison, D., McKay, D., Aitken, F., Takeda, H., Schonfeld, E., 1971. Mineralogy, chemistry, and origin of the KREEP component in soil samples from the Ocean of Storms. Proceedings of the 2nd Lunar Science Conference 101, 393.

Middleton, R., 1983. A versatile high intensity negative ion source. Nuclear Instruments and Methods 214, 139–150.

Moskalenko, I., Strong, A., Mashnick, S., Ormes, J., 2003. Challenging cosmic-ray propagation with antiprotons: evidence for a "fresh" nuclei component? The Astrophysical Journal 586, 1050–1066.

Muller, R., 1977. Radioisotope Dating with a Cyclotron. Science 196, 489.

Nagle, J., 1980. Possible rim crest deposits in cores 12027 and 15008: Some interpretations and problems for future research, pp. 1479–1496.

NASA, 1972. Preliminary Examination Team. The Apollo 15 Lunar Samples: A preliminary Description.

Nishiizumi, K., Arnold, J., Kubik, P., Sharma, P., 1990. New results on history of gardening in lunar cores 15008 and 76001 using cosmogenic radionuclides, p. 895.

Nishiizumi, K., Honda, M., 2007. Cosmogenic iron-60 in iron meteorites: measurements by low-level counting. Proceedings of the 70th Annual Meteoritical Society Meeting , 5281.

Nishiizumi, K., Imamura, M., Honda, M., Russ, G., Kohl, C., Arnold, J., 1976. ^{53}Mn in the Apollo 15 and 16 drill stems: Evidence for surface mixing, pp. 41–54.

Nishiizumi, K., Imamura, M., Kohl, C., Murrell, J., Arnold, J., Russ, G., 1979. The extent of lunar regolith mixing. Earth and Planetary Science Letters 44, 409–419.

Poutivtsev, M., 2007. Extraterrestrisches ^{53}Mn in hydrogenetischen Mangankrusten. Ph.D. thesis. Technical University of Munich.

Poutivtsev, M., Dillmann, I., Faestermann, T., Knie, K., Korschinek, G., Lachner, J., 2010. Highly sensitive AMS measurements of ^{53}Mn. Nuclear Instruments and Methods in Physics Research B 268, 756.

Ramond, T., Davico, G., Hellberg, F., Svedberg, F., Salen, P., Soderqvist, P., Libeberger, W., 2002. Photoelectron spectroscopy of nickel, palladium, and platinum oxide anions. Journal of Molecular Spectroscopy 216, 1.

Rancitelli, L., Perkins, R., Felix, W., 1971. Erosion and mixing of the lunar surface from cosmogenic and primordial radio-nuclide measurements in Apollo 12 lunar samples. Lunar and Planetary 2, 1757.

Rauscher, T., Heger, A., Hoffman, R., Woosley, S., 2002. Nucleosynthesis in massive stars with improved nuclear and stellar physics. The Astrophysical Journal 576, 323.

Reedy, R., Arnold, J., 1972. Interaction of Solar and Galactic Cosmic-Ray Particles with the Moon. Journal of Geophysical Research 77.

Reedy, R., Arnold, J., Lal, D., 1983. Cosmic-ray record in solar system matter. Annual Review of Nuclear and Particle Science 33, 505.

Rolfs, C., Rodney, W., 1988. Cauldrons in the Cosmos. The University of Chicago Press.

Rugel, G., Faestermann, T., Knie, K., Korschinek, G., Poutivtsev, M., Schumann, D., Kivel, N., Günther-Leopold, I., Weinreich, R., Wohlmuther, M., 2009. New Measurement of the ^{60}Fe Half-Life. Physical Review Letters 103, 14–17.

Sayer, R., 1977. Semi-empirical formulas for heavy ion stripping data. Revue de Physique Appliquée 12, 1543.

Schumann, D., Neuhausen, J., Eikenberg, J., Rüthi, M., Wohlmutter, M., Kubik, P., Synal, H., Alfimov, V., Korschinek, G., Rugel, G., Faestermann, T., 2009. Radiochemical analysis of a copper beam dump irradiated with high-energetic protons. Radiochimica Acta 97, 123.

Segl, M., Mangini, A., Bonani, G., Hofmann, H., 1984. 10Be-dating of a manganese crust from Central North Pacific and implications for ocean palaeocirculation. Nature 7, 540.

Shima, K., Kuno, N., Yamanouchi, M., 1992. Equilibrium charge fractions of ions of Z=4-92 emerging from a carbon foil. Atomic Data and Nuclear Data Tables 51, 173.

Voyager-1, 2013. NASA Spacecraft Embarks on Historic Journey Into Interstellar Space. `http://www.nasa.gov/mission_pages/voyager/voyager20130912.html` [Online; accessed December 2013].

Warren, P., Taylor, G., Keil, K., Kallemeyn, G., Shirley, D., Wasson, J., 1983. Seventh Foray: Whitlockite-rich lithologies, a diopside-bearing troctolitic anorthosie, ferroan anorthosites and KREEP. Journal of Geophysical Research 88, B151.

Wieler, R., Beer, J., Leya, I., 2013. The galactic cosmic ray intensity over the past 10^6-10^9 years as recorded by cosmogenic nuclides in meteorites and terrestrial samples. Space Science Reviews 176.

Woosley, S., Heger, A., 2007. Nucleosynthesis and remnants in massive stars of solar metallicity. Physics Reports 442, 269.

Woosley, S., Weaver, T., 1995. The evolution and explosion of massive stars. II. Explosive hydrodynamics and nuclesynthesis. The Astrophysical Journal Supplement Series 101, 101.

Acknowledgments

After dedicating so much time to this thesis, I want to thank all people who helped me along the way and contributed in a way or another to this work.

First of all, I want to thank Prof. Dr. Reiner Krücken for giving me the opportunity of work at his chair and Prof. Dr. Walter Henning for continuing with his support.

Thanks to Dr. Gunther Korschinek, for giving me the chance to work on such an exciting subject, with the perk of having a piece of the Moon in my hands. Thank you for the patience and time you dedicated to me. Thank you for the discussions and for spreading me enthusiasm for AMS. Thank you for your help when I moved to Germany, for the espressos and Krapfen. And thank you for correcting my German (and sorry for still making the same grammar mistakes!).

I also want to thank Dr. Thomas Faestermann. I will always admire his creativity and wisdom. Thank you for always explaining to me things several times until I understand them.

I want to especially thank Dr. Gregory Herzog for the chemical preparation of the lunar samples and for always being so kind to me, and Dr. Silke Merchel for supplying the meteorite samples.

Thanks to all members of the GAMS group for the help during the experiments. Thank you Karin Hain, Peter Ludwig, José Manuel Gómez Guzmán and Nicolai Famulok for making the time spent during shifts fun. I also want to thank Dr. Georg Rugel for teaching me everything related to the measurements, from cleaning and building the ion source to analyzing the spectra, and everything in between. I also want to thank Ursula Heim for sharing time in the office. And thanks to the honorary group member, Clemens Herlitzius, for his very enjoyable company during lunch and coffee breaks.

I am grateful to the MLL staff, operators, technicians and everyone who makes this lab viable, being always willing to help. I enjoyed very much working with everyone of you and I will always be thankful for your help making this work possible. I want to acknowledge the E12 staff, specially Sigrid Weichs and Petra Zweckinger for all their help.

Although they have not directly contributed to this work, I am very grateful to Dr. Guillermo Martí and Dr. Andrés Arazi, former advisors and present friends. I also want to thank Darío Rodrigues for his help throughout beamtimes during his visits.

Finally, I want to thank my family and friends, who never stop supporting me and believing in me. I miss you all very much. Last, but not least, I will be always grateful to Peter, for having read this work several times, for having not given up on me, for being my loving partner, and for everything.